

AD-A144 439

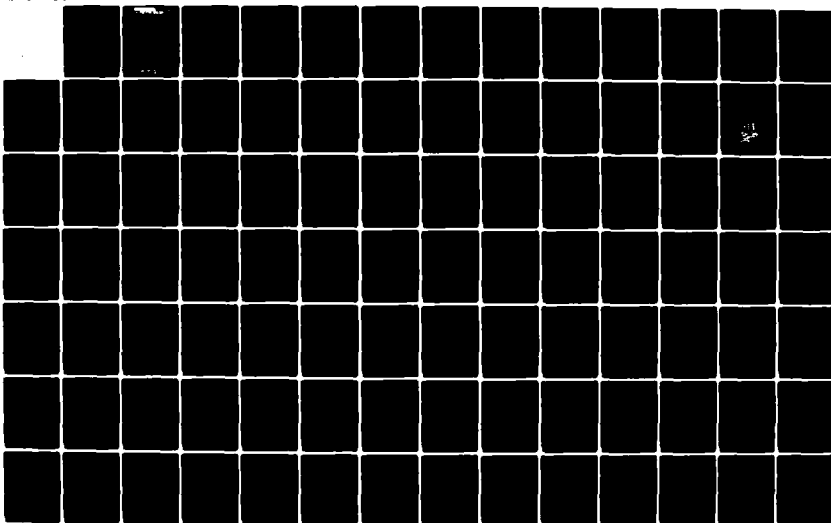
SINTERABLE CERAMIC POWDERS FROM LASER HEATED GAS PHASE  
REACTIONS AND RAPID (U) MASSACHUSETTS INST OF TECH  
CAMBRIDGE ENERGY LAB J S HAGGERTY JUL 84 MIT-EL-84-009  
N00014-82-K-0350

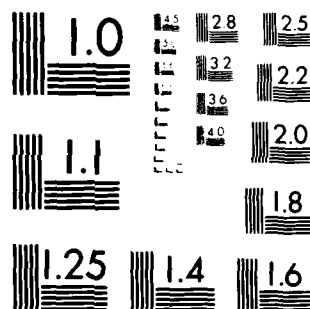
1/2

UNCLASSIFIED

F/G 11/2

NL





MICROCOPY RESOLUTION TEST CHART  
NATIONAL BUREAU OF STANDARDS-1963-A

(12)

ENERGY LABORATORY  
AND  
MATERIALS PROCESSING CENTER

DTIC FILE CY ADA144 439

SINTERABLE CERAMIC POWDERS FROM LASER  
HEATED GAS PHASE REACTIONS AND RAPIDLY SOLIDIFIED  
CERAMIC MATERIALS

BY

John S. Haggerty

July 1984

Energy Laboratory Report  
MIT-EL 84-009

DTIC

AUG 15 1984



This document is a copy  
for public release and is  
distributed as such.

BUILDING NO. 12  
MASSACHUSETTS INSTITUTE OF TECHNOLOGY

CAMBRIDGE, MASSACHUSETTS 02139

84 08 14 162

**ANNUAL REPORT**

**SINTERABLE CERAMIC POWDERS FROM LASER  
HEATED GAS PHASE REACTIONS AND RAPIDLY SOLIDIFIED  
CERAMIC MATERIALS**

Principal Investigator

Dr. John S. Haggerty

Energy Laboratory  
and  
Department of Materials Science and Engineering

Massachusetts Institute of Technology

Cambridge, Massachusetts 02139


Prepared for:

The Office of Naval Research  
(ONR)

and

The Army Research Office  
(ARO)

Contract No: N00014-82-K-0350  
Contract Expiration Date: 5/31/84  
Status Report Period: 4/01/82 - 5/31/84



REPORT DOCUMENTATION PAGE		READ INSTRUCTIONS BEFORE COMPLETING FORM										
1. REPORT NUMBER MIT-EL 84-009	2. GOVT ACCESSION NO. <b>A144439</b>	3. RECIPIENT'S CATALOG NUMBER										
4. TITLE (and Subtitle) Sinterable Ceramic Powders from Laser Heated Gas Phase Reactions and Rapidly Solidified Ceramic Materials	5. TYPE OF REPORT & PERIOD COVERED 4/01/82-5/31/84 Technical Report	6. PERFORMING ORG. REPORT NUMBER MIT-EL 84-009										
7. AUTHOR(s) John S. Haggerty	8. CONTRACT OR GRANT NUMBER(s) N00014-82-K-0350											
9. PERFORMING ORGANIZATION NAME AND ADDRESS Massachusetts Institute of Technology Cambridge, MA 02139	10. PROGRAM ELEMENT, PROJECT, TASK AREA & WORK UNIT NUMBERS											
11. CONTROLLING OFFICE NAME AND ADDRESS O.N.R. Department of the Navy 800 North Quincy Street, Arlington, VA 22217	12. REPORT DATE July 1984	13. NUMBER OF PAGES 120										
14. MONITORING AGENCY NAME & ADDRESS (if different from Controlling Office)	15. SECURITY CLASS. (of this report) Unclassified	15a. DECLASSIFICATION DOWNGRADING SCHEDULE										
16. DISTRIBUTION STATEMENT (of this Report) Unrestricted												
17. DISTRIBUTION STATEMENT (of the abstract entered in Block 20, if different from Report) Unrestricted												
18. SUPPLEMENTARY NOTES												
19. KEY WORDS (Continue on reverse side if necessary and identify by block number) <table border="0"> <tr> <td>Al<sub>2</sub>O<sub>3</sub>-Cr<sub>2</sub>O<sub>3</sub> Melt Surface Tensions</td> <td>Gas Phase Synthesis of Powders</td> </tr> <tr> <td>Al<sub>2</sub>O<sub>3</sub>-MgO Melt Surface Tensions</td> <td>Laser Driven Reactions</td> </tr> <tr> <td>Al<sub>2</sub>O<sub>3</sub>-TiO<sub>2</sub> Melt Surface Tensions</td> <td>Laser Heated Gases</td> </tr> <tr> <td>Al<sub>2</sub>O<sub>3</sub>-ZrO<sub>2</sub> Melt Surface Tensions</td> <td>Laser Synthesis of Powders</td> </tr> <tr> <td>Ceramic Powders</td> <td>Molten Oxide Surface Tensions</td> </tr> </table>			Al <sub>2</sub> O <sub>3</sub> -Cr <sub>2</sub> O <sub>3</sub> Melt Surface Tensions	Gas Phase Synthesis of Powders	Al <sub>2</sub> O <sub>3</sub> -MgO Melt Surface Tensions	Laser Driven Reactions	Al <sub>2</sub> O <sub>3</sub> -TiO <sub>2</sub> Melt Surface Tensions	Laser Heated Gases	Al <sub>2</sub> O <sub>3</sub> -ZrO <sub>2</sub> Melt Surface Tensions	Laser Synthesis of Powders	Ceramic Powders	Molten Oxide Surface Tensions
Al <sub>2</sub> O <sub>3</sub> -Cr <sub>2</sub> O <sub>3</sub> Melt Surface Tensions	Gas Phase Synthesis of Powders											
Al <sub>2</sub> O <sub>3</sub> -MgO Melt Surface Tensions	Laser Driven Reactions											
Al <sub>2</sub> O <sub>3</sub> -TiO <sub>2</sub> Melt Surface Tensions	Laser Heated Gases											
Al <sub>2</sub> O <sub>3</sub> -ZrO <sub>2</sub> Melt Surface Tensions	Laser Synthesis of Powders											
Ceramic Powders	Molten Oxide Surface Tensions											
20. ABSTRACT (Continue on reverse side if necessary and identify by block number) <p>CO<sub>2</sub> lasers have been employed to heat reactant gases to synthesize Si, Si<sub>3</sub>N<sub>4</sub> and SiC powders. The powders are small, uniform in size, nonagglomerated, highly pure and of controlled crystallinity, all parameters considered ideal for fabrication of defect-free ceramic parts. The unique and uniform time-temperature histories achievable with laser heating permit these important characteristics to be realized.</p>												

Dispersions of Si powders have been made and characterized extensively. These results have defined an appropriate strategy for making concentrated dispersions and have confirmed earlier preliminary results. Zeta-potential and photon correlation spectrometry have been used to study the effects of water contamination in the alcohol dispersants. Based on current results, we believe that concentrated dispersions will be achieved with steric rather than coulombic stabilization. Coulombic repulsive forces are effective only with dilute dispersions.

Manufacturing cost analysis shows that submicron powders can be made at lower cost with gas phase processes than with comminution processes. The laser heat source does not contribute significantly to the total costs. Total manufacturing costs are dominated by even lower than present actual feed stock ( $\text{SiH}_4$ ) costs. Recent cost reductions indicate that acceptable  $\text{SiH}_4$  costs may be realized soon.

Surface tensions of  $\text{Al}_2\text{O}_3$  based melts with  $\text{MgO}$ ,  $\text{Cr}_2\text{O}_3$ ,  $\text{TiO}_2$  and  $\text{ZrO}_2$  additives have been measured in neutral, oxidizing and reducing atmospheres. A new procedure was developed to analyze pendant drops which permits high precisions with the short maximum drop lengths that are characteristic of these materials. A  $\text{CO}_2$  laser heat source was used to melt the polycrystalline feed rods.

Molten oxide drops were splat quenched using a copper piston and anvil quenching apparatus. Approximately 500 samples of 10 oxide materials have been made. These samples are being characterized with respect to crystallinity, grain size, hardness,  $K_{IC}$  and surface composition. These results will be reported in the future.

#### 19. KEY WORDS

Nucleation and Growth of Particles	Pendant Drop Analysis
Particle Diameter Measurement	Silicon Carbide Powder
Particle Number Density Measurement	Silicon Nitride Powder
Particle Temperature Measurement	Silicon Powder

## TABLE OF CONTENTS

TITLE	PAGE
<b>CHAPTER I</b>	1
Introduction and Summary	1
References	6
<b>CHAPTER II: Growth of Precisely Controlled Powders from Laser Heated Gases</b>	9
II.1. Introduction	9
II.2. Laser Heated Powder Synthesis Process	11
II.2.A. Process Description	11
II.2.B. Powder Characteristics	15
II.2.C. Process Attributes	16
II.3. Conclusions	23
II.4. Acknowledgements	23
II.5. References	24
<b>CHAPTER III: Powder Temperature, Size, and Number Density in Laser Driven Reactions</b>	27
III.1. Introduction	27
III.2. Experimental Apparatus and Methodology	28
III.3. Experimental Procedure	33
III.4. Results and Discussion	35
III.5. Conclusion	43
III.6. Acknowledgements	44
III.7. References	45
Appendix III.A.	46
<b>CHAPTER IV: Homogeneous Nucleation and Growth of Silicon Powder from Laser Heated <math>\text{SiH}_4</math></b>	49
IV.1. Introduction	49
IV.2. Experimental and Analytical Procedures	51
IV.3. Results and Observations	53
IV.3.A. Temperature Measurements	53
IV.3.B. In Situ Nucleation and Growth Measurements	55
IV.4. Particle Nucleation and Growth Mechanisms	56
IV.4.A. Nucleation	56
IV.4.B. Growth	63
IV.4.C. Control of Particle Size, Shape and Distribution	69
IV.5. Conclusions	71
IV.6. Acknowledgements	71
IV.7. References	72

## TABLE OF CONTENTS

TITLE	PAGE
<b>CHAPTER V: Dispersion of Silicon in N-Propanol</b>	<b>75</b>
V.1. Introduction	75
V.2. Theoretical Considerations	77
V.3. Procedures	85
V.3.A. IR Spectroscopy	85
V.3.B. Specific Surface Area, TEM and Photon Correlation Determinations of Particle and Agglomerate Sizes	85
V.3.C. Electrophoretic Mobility Determinations	87
V.4. Results and Discussion	87
V.4.A. IR Study	87
V.4.B. Particle and Agglomerate Size Distribution	91
V.4.C. Zeta Potential Measurements	97
V.4.D. Dispersion Stability	99
V.5. Conclusions	102
V.6. Acknowledgements	103
V.7. References	104
<b>CHAPTER VI: Surface Tensions of Alumina-Containing Liquids</b>	<b>107</b>
VI.1. Introduction	107
VI.2. Analytical	107
VI.3. Experimental	111
VI.4. Results and Discussion	113
VI.5. Summary and Conclusions	117
VI.6. Acknowledgements	118
VI.7. References	119



Accession For	
NTIS GR-61	<input checked="" type="checkbox"/>
DTIC TAB	
Unannounced	
Justification	
P.	
Distribution	
Avail. and/or Sales	
Remarks	
<i>Al</i>	



# LIST OF FIGURES

FIGURE		PAGE
II.1.	Powder synthesis cell. <sup>3</sup>	12
II.2.	TEM photomicrograph of laser synthesized SiC powder. <sup>3</sup> Mean diameter ~ 250 $\mu$ .	14
II.3.	Temperature versus distance from nozzle for several Si synthesis runs. <sup>7,8</sup>	18
II.4.	Particle size versus distance from nozzle for several synthesis runs. <sup>7,8</sup>	18
II.5.	Particle number density versus distance from nozzle for a typical Si synthesis run. <sup>7,8</sup>	19
II.6.	Sales price in 5000 kg lots for Acheson SiC powder <sup>22</sup> , specific comminution energy <sup>23</sup> and manufacturing cost for SiC powders made from laser heated gases as functions of particle size.	22
III.1.	Schematic of the reaction zone.	28
III.2.	Scatter-extinction ratio versus $C_{sca} / C_{ext}$ .	32
III.3.	Scatter-extinction ratio versus particle radius.	32
III.4.	Scatter-extinction optical layout.	34
III.5.	$I_{\perp}$ , $E(20^{\circ})$ , and scatter-extinction ratio for run 631S.	36
III.6.	Temperature and emissivity for run 631S.	36
III.7.	Temperature and emissivity for run 654S.	37
III.8.	Temperature versus distance from nozzle.	37
III.9.	Particle size versus distance from nozzle.	38
III.10.	Particle number density versus distance from nozzle.	38
III.11.	Temperature and emissivity for Run # 910SiC.	42
III.12.	Particle size and number density for Run # 910SiC.	42
III.A-1.	Scattering diagram with cylindrical symmetry.	47

FIGURE		PAGE
IV.1.	Schematic of powder synthesis cell.	52
IV.2.	True temperature, brightness temperature, and emissivity as a function of distance above the inlet nozzle for Run 631S.	54
IV.3.	Particle size calculated from the scatter-extinction results as a function of distance above the inlet nozzle for various synthesis runs.	54
IV.4.	Product of the particle number density and optical pathlength as a function of distance above the inlet nozzle.	58
IV.5.	The effect of temperature and percent reaction on the supersaturation ratio for silane pyrolysis.	58
IV.6.	Calculated silicon concentration in the reaction zone as a function of distance above the inlet nozzle for Run 654S.	66
IV.7.	The logarithm of the growth rate calculated from the scattering-extinction results versus the logarithm of the silicon concentration in the reaction zone. (a. Run 630S, b. Run 654S.	66
V.1.	Double layer thickness as a function of ionic concentration, $\epsilon = 20.4$ ; $T = 300^\circ\text{K}$ .	80
V.2.	Schematic of interparticle energies for a typical stable aqueous dispersion.	81
V.3.	Interparticle energies for charged silicon particles in n-propanol as a function of interparticle distance; particle radius = $400\text{\AA}$ ; surface charge = $80\text{ mV}$ ; $[\text{ion}] = 1 \times 10^{-9}\text{ m}$ at $300^\circ\text{K}$ .	81
V.4.	Interparticle energies for silicon in n-propanol as functions of interparticle distance and surface charge. Radius = $400\text{\AA}$ ; $[\text{ion}] = 1 \times 10^{-9}\text{ m}$ ; $T = 300^\circ\text{K}$ .	82
V.5.	Interparticle energies for silicon in n-propanol as functions of interparticle distance $\Delta$ and particle radius. $\psi_0 = 80\text{ mV}$ ; $[\text{ion}] = 1 \times 10^{-9}\text{ m}$ ; $T = 300^\circ\text{K}$ .	82
V.6.	Interparticle attraction of silicon in n-propanol with and without adsorbed water. Radius = $100\text{\AA}$ ; water layer thickness = $20\text{\AA}$ ; $T = 300^\circ\text{K}$ .	84
V.7.	FTIR absorbance plot of sample 226S; KBr pellet.	86

FIGURE		PAGE
V.8.	FTIR absorbance plot of sample 227SB; KBr pellet.	86
V.9.	TEM particle size distribution of sample 226S.	88
V.10.	TEM particle size distribution of sample 227SB.	88
V.11.	TEM particle size distribution of sample 806SB.	90
V.12.	BET equivalent spherical diameters versus TEM arithmetic means for eight silicon powders.	90
V.13.	BET equivalent spherical diameters versus TEM weighted mean diameters for eight silicon powders.	92
V.14.	TEM agglomerate size distribution for sample 226S.	92
V.15.	TEM agglomerate size distribution for sample 231S.	93
V.16.	TEM agglomerate size distribution for sample 806SB; 10 ppm silicon in n-propanol.	93
V.17.	TEM agglomerate size distribution for sample 226S; 10 ppm silicon in n-propanol.	94
V.18.	TEM agglomerate size distribution for sample 227SB; 10 ppm silicon in n-propanol.	94
V.19.	Log-normal agglomerate size plot of data in Figure V.16 sample 806SB.	95
V.20.	Log-normal agglomerate size plot of data in Figure V.17 sample 226S.	95
V.21.	Log-normal agglomerate size plot of data in Figure V.18 sample 227SB.	96
V.22.	TEM particle size distribution for sample B004S showing three types of particles. Bar length = 10,000Å.	96
V.23.	TEM micrograph of centrifuged sediment of sample B004S. Bar length = 10,000Å.	98
V.24.	The effect of water on the rate of agglomeration as measured by photon correlation. Sample 227-SB, 4ppm in n-propanol.	100
VI.1.	Shows some pendant-drop shapes computed for a constant $r_e$ value. Curves D through H in this order correspond to $\beta$ values (Equation 3) of -0.25, -0.31, -0.37, -0.475, and -0.55. Curves A, B and C, though defined by very close	

## FIGURE

## PAGE

values of  $S = r_s/r_e$  (Equation 6) and almost undistinguishable at the altitude  $z = 2r_e$ , correspond to  $\gamma/\rho$  values as different as 214.73, 201.79 and 187.24, respectively.

110

VI.2. Illustrates the non-linear aspect of Equation 3. Parallel curves like A, B, and C correspond to very different  $\gamma/\rho$  values: 190.4 (A), 253.7 (b) and 352.5 (C), whereas non-parallel contours D, E and F define similar values of  $\gamma/\rho$ : 249.5 (D), 253.7 (E), 258.2 (F).

110

VI.3. Density of the various melts as calculated with the approximations detailed in Section VI.2.

111

VI.4. Experimental surface tension of the liquids in air.

115

VI.5. Experimental surface tension of the liquids in helium.

115

VI.6. Experimental surface tension of the liquids in a 90% helium - 10% hydrogen mixture.

116

VI.7. Experimental surface tension of various  $Al_2O_3$ - $ZrO_2$  liquid:1 in air.

116

## LIST OF TABLES

TABLE	PAGE
II.1. Process Conditions Used for Si, Si N and SiC	12
II.2. Summary of Powder Characteristics	14
II.3. Manufacturing Rates and Costs	20
III.1. Powder Synthesis Reactions Studied	34
IV.1. Synthesis Conditions from Appendix 1 Runs 6305, 6315, 6545, 6505, 6345.	52
IV.2. Nucleation Calculations for a Reaction Zone Initially Comprised of 0.2 atm. of Pure Silane.	60
IV.3. Comparison of Experimental Growth Rate and Calculated Growth Rate (Transport Limited).	68
V.1. Hamaker Constants	80
V.2. A Comparison of Two Methods of Agglomerate Size Distribution Characterization	98
V.3. Zeta Potentials of Silicon Powders in N-Propanol with Varied Water Concentration	100
VI.1. Cited Surface Tension Values of Liquid Alumina	114

## FORWARD

This research program involved several groups within M.I.T. which represented different technical disciplines. The principal investigator, Dr. J. S. Haggerty is a materials scientist associated with both the Energy Laboratory and the Department of Materials Science and Engineering. R. A. Marra and J. H. Flint were graduate students in the Department of Materials Science and Engineering; their research contributed to every aspect of this program. Mr. J. Flint has continued as a member of the research staff and Mr. G. Garvey and Dr. Lihrmann are both members of the research staff. Everyone's contributions are gratefully acknowledged.

PRECEDING PAGE BLANK-NOT FILMED

## CHAPTER I

### INTRODUCTION AND SUMMARY

The research undertaken in this program addresses two new approaches for processing ceramic materials. One is based on particulate processes using powders with an unusual and highly specific set of characteristics. The other attempts to modify material properties by means of rapid solidification techniques.

It was hypothesized<sup>1</sup> and now has been demonstrated<sup>2</sup> that the microstructural characteristics of polycrystalline ceramic bodies could be dramatically improved by using powders having uniform particle sizes. Also, the time-temperature cycles needed for complete densification are lower in temperature and shorter in time than needed for conventional powders.<sup>3</sup> The superior microstructural and processing characteristics result directly from the defect-free, high coordination number green bodies that can be produced with uniform diameter, agglomerate free powders. Additionally, the powders must have a small diameter, be equiaxed, have high purity and have specific stoichiometry and crystallinity.

Because existing powder synthesis techniques could not produce  $\text{Si}_3\text{N}_4$  and  $\text{SiC}$  powders with these requisite characteristics, we developed a laser heated gas phase synthesis process.<sup>4,5,6</sup> In the laser process uniform nucleation and growth rates produce uniform powders. The program has emphasized the synthesis of  $\text{Si}$ ,  $\text{Si}_3\text{N}_4$  and  $\text{SiC}$  powders. The  $\text{Si}$  powders are used for the reaction bonding process in which densification and conversion to  $\text{Si}_3\text{N}_4$  occur simultaneously. We have had two specific objectives. Our initial and primary objective has been to develop a process for producing ceramic powders having the desired characteristics. To this end, we have concentrated on developing an analytical description of the laser driven synthesis process.<sup>7,8</sup> Secondly, we have begun to process the powders into bodies.<sup>9,10,11</sup> This phase has concentrated on finding means to disperse  $\text{Si}$  powders in nonaqueous liquids. Particle size distributions, agglomerate sizes, zeta potentials, and coagulation rates have been measured. Coulombic and van der Waals interparticle forces have been calculated.

Based on results with metals and other considerations, we anticipate that unusual and superior materials properties can be realized by rapidly

solidifying ceramic materials. Unusual, attractive densification characteristics have already been observed<sup>11</sup> with the amorphous powders that can be produced by the laser heated gas phase synthesis process. We have developed the means to produce rapidly solidified ceramics and have begun preliminary characterization of these materials.<sup>12</sup> Initially, these experiments are focusing on materials that exhibit interesting electrical properties. Also, prior to being dropped into the quenching apparatus, the melts can be characterized to yield surface tensions, densities and viscosities. Our initial research has concentrated on an improved analytical procedure for pendant-drops needed for melts having surface tension and densities characteristic of oxides.<sup>13</sup>

This report consists of five technical chapters. Four are preprints of papers that have been submitted for publication and the fifth is a statement of the present status of our ability to disperse nonionic powders in nonaqueous media. The principal contributors are reflected by the authorship.

Studies of the synthesis process have addressed many technical and economic issues. The second chapter,<sup>14</sup> entitled "Growth of Precisely Controlled Powders from Laser Heated Gases", summarizes the general features of the synthesis process as it is presently configured, the characteristics of resulting powders and projected manufacturing costs. The results are extremely encouraging. The third chapter, entitled "Powder Temperature, Size and Number Density Evolution in Laser Driven Reactions", reports the procedures developed to monitor nucleation and growth of particles in laser heated reactants. This unique experimental technique provides a basis for analysing reaction kinetics as a function of reactant partial pressures and temperatures with a 0.5 mm spacial resolution. The fourth chapter, entitled "Homogeneous Nucleation and Growth of Silicon Powder from Laser Heated  $\text{SiH}_4$ ", applies this diagnostic technique to the nucleation and growth kinetics of Si particles from  $\text{SiH}_4$  gas. Rate controlling steps for nucleation and growth steps were identified. The fifth chapter, entitled "Dispersion of Silicon in n-Propanol", summarizes the dispersion results for Si powders. Based on these results and analyses, the feasibility of successfully employing coulombic and steric stabilization are discussed. On the second subject, the sixth chapter, entitled "Surface Tensions of Alumina-Containing Liquids", presents the first results of characterizing high temperature liquids.



Surface tensions of alumina-containing melts are reported as a function of composition and ambient atmosphere.

The results of characterizations continue to demonstrate that the laser heated gas phase powder synthesis process is capable of producing Si,  $\text{Si}_3\text{N}_4$  and SiC powders having the desired characteristics. The particles can be small, uniform in diameter, weakly agglomerated, spherical, of high purity and controlled stoichiometry and crystallinity. While the maximum diameter achieved with Si ( $\sim 2500\text{\AA}$ ) exceeds our target of  $1500\text{\AA}$ , to date we have not reached this large a diameter with  $\text{Si}_3\text{N}_4$  and SiC. By manipulating process variables we have suppressed nucleation to permit maximum diameters to be increased to  $\sim 700\text{\AA}$ ; further processing research is required to achieve larger  $\text{Si}_3\text{N}_4$  and SiC powders. Recent results with Si have shown that hard agglomerates can form both by sintering and melting mechanisms when heated excessively. Thorough characterization of these types of particles has resolved some anomalies between measured and BET equivalent diameters of the larger diameter powders. Overall, the process still appears capable of satisfying the technical requirements and is scalable to higher rates of production.

A simplified manufacturing cost analysis was undertaken to provide a first estimate of anticipated production costs and to reveal critical cost factors. These results show that the process can produce submicron diameter powders at a cost of \$2.60 to \$3.70 per kg exclusive of reactant materials. The future cost of  $\text{SiH}_4$  dominates anticipated manufacturing costs. Even with higher than anticipated costs for  $\text{SiH}_4$  ( $\sim 20\text{\$/kg}$ ), this process appears capable of producing submicron SiC powders at substantially lower costs than those produced by grinding Acheson material. This very important result is the basis for scaling the process to pilot scale production levels.

The direct measurement of nucleation and growth kinetics formed an important link between our previously developed empirical relationships between process variables and powder characteristics and the existing kinetic models for low growth rate CVD processes. The new diagnostic technique is based on simultaneous HeNe laser light scattering and transmission measurements. The results permit calculation of the local emissivity, number density and particle diameter in the reaction zone.

Combined with measurements of brightness temperatures and calculated gas velocities, nucleation and growth rates are derived as a function of

temperature and reactant partial pressures. The calculated results are extremely sensitive to the assumed complex index of refraction. While this introduces a potential for error, the sensitivity can be used to interpret reaction mechanisms when calculated results are compared with the results of other independent characterizations.

The diagnostic technique gives heating rates ( $10^6$ - $10^8$ °C/s), maximum temperature, dwell time at maximum temperature ( $\sim 10^{-4}$ s), and cooling rates ( $\sim 10^{-5}$ °C/s). For Si powder, it also provided direct evidence that the nucleation process stops early in the reaction ( $\sim 2\%$  conversion), that agglomerates do not form in the heated zone and that the Si particles are amorphous when formed and then may crystallize if heated sufficiently. The growth processes could be monitored from a minimum particle diameter of  $\sim 80\text{\AA}$ .

The nucleation and growth kinetics of Si particles from  $\text{SiH}_4$  gas were studied. Particles nucleate homogeneously at rates in excess  $10^{14}$  per  $\text{cm}^3/\text{s}$ . The high level of initial supersaturation presents no barrier to nucleation, rather the nucleation rate appears controlled by the concentration of Si atoms in the vapor phase. Growth rate is controlled by vapor phase transport of reactants to the particle surfaces. The condensation coefficient is estimated to be 0.002-0.02. Particle growth terminates when reactants are depleted; the final particle size depends on the initial nuclei density and the reactant concentration. The separation of the nucleation and growth processes intrinsically tends to yield uniform powders.

Building on earlier research,<sup>9,15,16</sup> the dispersibility of Si powders in n-propanol has been studied. This work incorporated a more complete characterization of the constituent powders. Particle size distribution, agglomeration, agglomerate size, bulk and surface purities and  $\zeta$ -potential were characterized for pure and boron doped powders. Dispersion stability and agglomeration rates were evaluated as functions of solids and water contents. The results were interpreted in terms of DLVO theory. Stable dispersions can be produced with low solids content and dry n-propanol. The low, dispersed coulombic potential barrier resulting from a large double layer does not provide adequate repulsion for close interparticle spacing. Stabilization by means of ionic additives which compress the double layer may be possible. Alternatively, steric barriers can be used to counteract van

der Waals attractive forces at close interparticle spacings. Because the theory for nonaqueous dispersions is not well developed, the dispersion research will of necessity proceed as a largely empirical study guided by theory.

The laser heated floating zone crystal growth apparatus was modified to permit melt surface tension and rapid solidification experiments. Both static and dynamic techniques are to be used to provide independent measurements of surface tension to density ratios. The dynamic technique will also permit measurement of melt viscosity. A piston and anvil quenching apparatus has been installed to splat quench high temperature liquids. Melts from  $Y_2O_3-ZrO_2$ ,  $Al_2O_3-ZrO_2$ ,  $Al_2O_3-TiO_2$ ,  $Al_2O_3-Cr_2O_3$ ,  $Al_2O_3-MgO$ ,  $Sc_2O_3-Ta_2O_5$  and  $Li_2O-B_2O_3$  systems have been quenched and characterized.

The results of the static, pendant-drop surface tension measurements are reported in detail. An improved analytical procedure based on comparing calculated and observed melt contours was developed. This new technique permits acceptable experimental accuracy with the short maximum pendant-drop lengths achievable with the oxide melts. Surface tensions of  $Al_2O_3$  containing melts with  $Cr_2O_3$ ,  $MgO$ ,  $TiO_2$  and  $ZrO_2$  additives were measured in air, helium and helium-hydrogen atmospheres. The surface tensions tended to increase with oxygen partial pressure. In air, the effect of additives on surface tension paralleled their effect on the melting point. In most cases, the compositional effects were approximately linear;  $TiO_2$ , an exception, caused a sharp decrease in  $\gamma$  for small additions that were followed by essentially constant  $\gamma$ 's for further additions. The effect of additives in neutral and reducing atmospheres was more complex and did not follow specific trends.

During the first year, the research has addressed all topics in the contractual scope of work. Technically and economically, the laser heated gas phase synthesis process appears to be a viable means of producing  $Si$ ,  $Si_3N_4$  and  $SiC$  powders. Many issues remain to be resolved before the highly perfect microstructures achieved with  $TiO_2$  powders are realized with these nonionic materials; but, they appear tractable. The rapidly solidified ceramics continue to be interesting based on results of microstructural characteristics.

## I. REFERENCES

1. H. K. Bowen et al., "Basic Research need on High Temperature Ceramics for Energy Applications," Mat. Sci. Eng., 4, 41-56.
2. E. A. Barringer and H. K. Bowen, "Formation, Packing and Sintering of Monodisperse  $\text{TiO}_2$  Powders" J. Am. Ceram. Soc., 65, 12, C-199-201 (1982).
3. E. A. Barringer, "The Synthesis, Intefacial Electrochemistry, Ordering, and Sintering of Monodisperse  $\text{TiO}_2$  Powders", Ph.D. Thesis, MIT, Cambridge, MA, September 1983.
4. W. R. Cannon, S. C. Danforth, J. S. Haggerty and R. A. Marra, "Sinterable Ceramic Powders from Laser Driven Reactions, Part I: Process Description and Modelling", J. Am. Ceram. Soc., 65, 324-30 (1982).
5. W. R. Cannon, S. C. Danforth, J. S. Haggerty and R. A. Marra, Sinterable Ceramic Powders from Laser Driven Reactions, Part II: Powder Characteristics and Process Variables", J. Am. Ceram. Soc., 65, 7 330-5 (1982).
6. J. S. Haggerty, "Sinterable Powders from Laser Driven Reactions, September 1981, Contract N00014-77-C0581, MIT, Cambridge MA.
7. J. H. Flint, "Powder Temperatures in Laser Driven Reactions", M.S. Thesis, MIT, Cambridge, MA, February 1982.
8. R. A. Marra, "Homogeneous Nucleation and Growth of Silicon Powder from Laser Heated Gas Phase Reactants", PhD Thesis, Department of Materials Science and Engineering, MIT, Cambridge, MA, January 1983.
9. S. Mizuta, W. R. Cannon, A. Bleifer, and J. S. Haggerty, "Wetting and Dispersion of Silicon Powder Without Deflocculants", Am. Ceram. Soc. Bull., 61, 872-875 (1982).
10. S. C. Danforth and J. S. Haggerty, "Mechanical Properties of Sintered and Nitrided Laser-Synthesized Silicon Powder", J. Am. Ceram. Soc., 66, 4, C-58-9 (1983)
11. H. T. Sawhill and J. S. Haggerty, "Crystallization of Ultrafine Amorphous  $\text{Si}_3\text{N}_4$  During Sintering", J. Am. Ceram. Soc., 65, 8, C-131-2, (1982).
12. J. S. Haggerty, H. Tuller, K. Russell, "Ionic Conductivity of Splat-Cooled Ceramics", Ceram. Bull., 61, 8, 805 (1982).
13. J. Lihrmann and J. S. Haggerty, "Surface Tensions of Oxide Melts", Ceram. Bull., 62, 3, 381 (1983).

14. J. S. Haggerty, "Growth of Precisely Controlled Powders from Laser Heated Gases", Proceedings of the International Conference on Ultrastructure Processing of Ceramics, Glasses, and Composites, February 13-17, 1983, Gainesville, Florida, Science of Ceramics, J. Wiley & Sons, 1983.
15. S. C. Danforth, Rutgers University, New Jersey, private communication.
16. M. Dahlén, Volvo Corporation, Sweden, private communication.

## CHAPTER II

### GROWTH OF PRECISELY CONTROLLED POWDERS FROM LASER HEATED GASES

by

J. S. Haggerty

#### ABSTRACT

Powders having superior characteristics have been synthesized from laser heated gases. These superior properties result from the unusually well controlled process conditions that are achievable with laser heating. Manufacturing costs appear lower than conventional submicron powders.

#### II.1. INTRODUCTION

This paper will summarize the principal features of a powder synthesis process developed at M.I.T. Many of the technical details have already been described<sup>1-6</sup> and others are being published. The latter include papers based on the theses of Flint<sup>7</sup> and Marra<sup>8</sup>, as well as contributions by Suyama<sup>9</sup>, Golino<sup>10</sup> and Gattuso<sup>11</sup>. This synthesis process was developed specifically to enable the making of powders having characteristics considered ideal for processing into ceramic parts has been discussed by Bowen.<sup>12</sup> These ideal powder characteristics include: uniform particle size, small particle size, equiaxed shapes, freedom from agglomerates, and absence of impurities or deviations from desired stoichiometry.

Our processing research has concentrated on the nonoxide particulate materials Si,  $\text{Si}_3\text{N}_4$  and SiC; to a lesser extent oxides have also been made by this process. Based on our results, it is apparent that laser heated gas phase processes can be employed with many different materials to make either powders or monolithic coatings.

A gas phase process was selected for making powders having ideal characteristics. Experience with  $\text{TiO}_2$  powder synthesis shows that gas phase processes can produce inexpensively powders having the desired characteristics. Heating techniques that were considered included rf and microwave plasmas, arcs, heated tubes, reactive sputtering techniques and optical heating means. The latter were elected because they appeared to combine

many desirable features. Although broadband optical sources can be used to heat gases, they are typically inefficient because the gases have few, narrow absorption lines. Heating with a laser can be very efficient with some lasers when emission and absorption lines coincide. The general process characteristics achievable with laser heating that were considered important include: a small, well defined heating zone can be created, all gas molecules can be subjected to similar time-temperature histories, process variables can be manipulated in reproducible and defined manners, controlled atmosphere, cold-wall reaction vessels are straight forward.

Specifically, we have used CO<sub>2</sub> lasers as heat sources for the gas phase reactions. This type of laser emits on approximately 100 different wavelengths between nominally 9.2 and 11.0  $\mu\text{m}$ . Several of these lines have been investigated in our research; fortunately, many of the useful reactant gases exhibit strong absorptivities for the P(20) line at 10.591  $\mu\text{m}$ . This is the highest gain line exhibited by a CO<sub>2</sub> laser and is both the most efficient choice and is the line usually emitted by the simple untuned lasers. These lasers convert electricity to light with approximately 15% efficiency; better than many alternative heating means. This laser equipment is extremely reliable, controllable and has a reasonable cost.

Reactant gases are heated by absorbing IR photons in these laser processes. They differ from photochemical reactions induced by ultraviolet or visible wavelength photons because absorption of single or multiple IR photons generally leaves the molecules in vibrationally or rotationally excited electronic ground states where they ultimately dissociate only when sufficient energy has been absorbed. With the high gas pressures used, these reactions basically proceed as thermal reactions with a Boltzmann distribution of energies. Even if collisions and other relaxation processes occur, these reactions may differ from conventional reactions because the short times and rapid heating rates may result in different intermediate states. Our investigation has not presumed unusual reaction paths and has proceeded on the premise that these laser induced reactions will differ from conventional reactions in the level of process control and the process conditions that can be achieved uniquely with them and that they will have value because of the superior properties of the resulting powders.

## II.2. LASER HEATED POWDER SYNTHESIS PROCESS

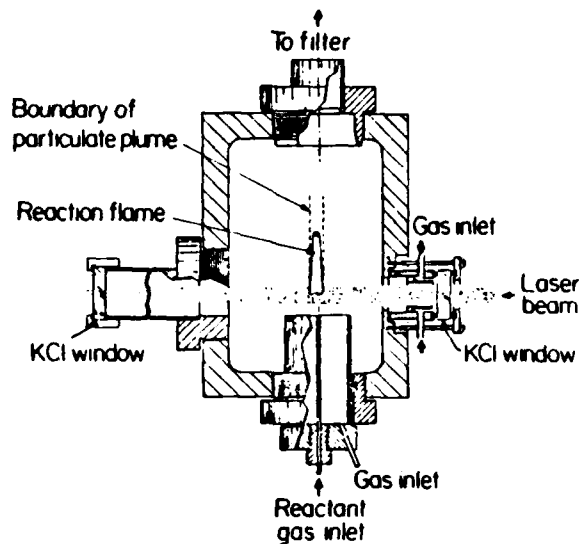
### II.2.A. Process Description

Powders have been synthesized with crossflow and counterflow gas stream - laser beam configurations and with both static and flowing gases. Most of the process research has been conducted with the reaction cell shown schematically in Figure II.1.

In a crossflow configuration, the laser beam having a Gaussian shaped intensity profile orthogonally intersects the reactant gas stream possessing a parabolic velocity profile. The laser beam enters the cell through a KCl window. The premixed reactant gases, under some conditions diluted with an inert gas, enter through a 1.5 mm ID stainless steel nozzle located 2-3 mm below the laser beam. A coaxial stream of argon is used to entrain the particles in the gas stream. Argon is also passed across the inlet KCl window to prevent powder build-up and possible window breakage. Cell pressures are maintained between 0.08 to 0.90 atm with a mechanical pump and throttling valve. At present, the powder is captured in a microfiber filter located between the reaction cell and vacuum pump. In the future, the particles will be collected by electrostatic precipitation or by separation with a fluid used for dispersion.

To insure uniform laser intensities throughout the reactants, the gas stream has been made optically thin. Typically only 2-15% of the incident light is absorbed by the reactants with this experimental apparatus configuration. Obviously more efficient use of the expensive laser energy is essential for a production process. The counterflow configuration permits the simultaneous, complete capturing of the light energy and uniform time - temperature histories. Although it is one alternative that probably satisfies production requirements, the counterflow apparatus is not well suited to an experimental program in which process variables are manipulated over orders of magnitude. There are several other equipment configurations that capture all of the light while achieving uniform heating. These include multiple radially opposed beams, reflecting the beam repeatedly through an optically thin gas stream as we are doing in the laser heated chemical vapor deposition process<sup>13</sup>, and intersecting an elongated, strip shaped gas stream at an oblique angle of incidence with one or more laser





### II.1. Powder synthesis cell.<sup>3</sup>

TABLE II.1

PROCESS CONDITIONS USED FOR Si, Si<sub>3</sub>N<sub>4</sub> AND SiC

Process Variable	Si	Si <sub>3</sub> N <sub>4</sub>	SiC
Cell Pressure (atm)	0.2-0.9	0.2-0.9	0.2-0.8
SiH <sub>4</sub> Flow Rate (cc/min)	5.4-110	5.4-40	11-45
NH <sub>3</sub> Flow Rate (cc/min)	0	44-110	0
C <sub>2</sub> H <sub>4</sub> Flow Rate (cc/min)	0	0	9.0-45
Ar Flow Rate (Annulus plus window) (cc/min)	560-1450	1000-1100	1000
Laser Intensity (W/cm <sup>2</sup> )	176-5.4x10 <sup>3</sup>	530-1x10 <sup>5</sup>	530-5.2x10 <sup>3</sup>
Reaction Zone Temp. (°C)	750-1390	675-1390	865-1930

beams. The virtually complete conversion of laser light to process heat appears quite feasible.

Principally, Si,  $\text{Si}_3\text{N}_4$  and SiC powders have been made from appropriate combinations of  $\text{SiH}_4$ ,  $\text{NH}_3$ , and  $\text{C}_2\text{H}_4$  gases.  $\text{CH}_4$  was investigated but we found that it did not react to form SiC with the laser heated process conditions. Alternative reactant gases such as  $\text{CH}_3\cdot\text{SiH}_3$  and  $\text{Cl}_2\text{SiH}_2$  have been investigated for SiC; others have also been used in preliminary experiments to make  $\text{Al}_2\text{O}_3$ ,  $\text{TiO}_2$  and  $\text{B}_4\text{C}$ . Diborane ( $\text{B}_2\text{H}_6$ ) was used to boron dope Si and SiC powders acting as a sintering aid.<sup>14</sup> Thus, while most of this process research has focused on a limited set of compounds and reactants, it is apparent that laser induced reactions are applicable to a broad range of materials.

The specific process conditions employed to make the powders have been manipulated over an extensive range. The investigated conditions are summarized in Table II.1. More recent synthesis runs have employed higher pressures, higher mass flow rates and near zero argon flow rates for the window stream. Fortunately, these latter conditions combine more desirable powder characteristics with economically more attractive process parameters.

Heating rates, nucleation rates, growth rates and temperatures can be estimated surprisingly accurately based on measured zone and particle dimensions, calculated gas velocities and uncorrected pyrometrically determined temperatures. For typical reaction conditions employing a total reactant gas flow rate of approximately 100  $\text{cm}^3/\text{min}$  and a pressure of 0.2 atm, the velocity of the gas decreases from approximately 500 cm/s at the nozzle to 350 cm/s at the center of the laser beam. With a  $\text{NH}_3/\text{SiH}_4$  flame, the reaction commences approximately 3 to 5 mm into the laser beam. Thus, the exposure time needed to initiate the reaction is nominally  $10^{-3}$  s. For a reaction temperature of approximately 1000°C, this indicates a gas heating rate of approximately  $10^6^\circ\text{C/s}$ . Time-temperature profiles have been computed<sup>3</sup> as a function of varied process parameters using calculated velocities, actual laser intensities and absorptivities that we have measured. Qualitatively, the calculations agree with observed effects.

For most process conditions, the reactants are essentially completely consumed; this is particularly important with expensive reactants. Also, particle growth is limited by depletion of the reactants rather than elapsed

TABLE II.2

## SUMMARY OF POWDER CHARACTERISTICS

Powder Type	Si	Si <sub>3</sub> N <sub>4</sub>	SiC
Mean Diameters (Å)	190-1700	75-500	200-500
Standard Deviation of Diameters (% of Mean)	46	23	~25
Impurities O <sub>2</sub> (wt. %)	0.06- 0.7	~0.3	0.3 - 1.3
Total Others (ppm)	<200	<100	NA
Major Elements	Ca, Cu, Fe	Al, Ca	NA
Stoichiometry	---	0-60% (excess Si)	0-10% (excess C or Si)
Crystallinity	crystalline -amorphous	amorphous -crystalline	crystalline Si and SiC
Grain Size: Mean Diameter	1/5-1/3	~1/2	1/2-1



II.2. TEM photomicrograph of laser synthesized SiC powder.<sup>3</sup> Mean diameter ~ 250Å.

growth time which permits particle size to be manipulated through control of the nucleation process.

#### II.2.B. Powder Characteristics

The Si,  $\text{Si}_3\text{N}_4$  and SiC powders all exhibit the same general features and appear to match the idealized characteristics we sought. Table II.2 summarizes the range of properties that have been achieved with these particulate materials.<sup>3,9</sup>

A bright field TEM photomicrograph of a typical SiC powder is shown in Figure II.2. The particles are spherical and uniform in size. The  $\text{Si}_3\text{N}_4$  and SiC powders are usually smaller and have a narrower size distribution than the Si powders. This micrograph also indicates the powders were observed in chainlike agglomerates after being captured in a filter. Neck formation has been observed by TEM between Si particles, but not with the  $\text{Si}_3\text{N}_4$  and SiC powders. Dispersion results<sup>15</sup> have shown primary bonding does not exist in necks between Si particles because light scattering and photon correlation spectrometer characterizations of the sols showed that the dispersed particle sizes are equal to those of the individual particles.<sup>3,15,16</sup> It is presumed that the same will be true of  $\text{Si}_3\text{N}_4$  and SiC powders that do not exhibit interparticle necks.

The BET equivalent spherical diameter and the diameter measured from TEM micrographs have always been nearly equal. This indicates that the particles have smooth surfaces, no porosity accessible to the surface, relatively narrow size distributions, and nearly spherical shapes. Powder densities, measured by He pycnometry, indicated the particles had no internal porosity.

Chemical analyses indicate that the oxygen content is generally less than 1.0% by weight and some powders are as low as 0.05 wt.%. The total cation impurities are typically less than 200 ppm. For  $\text{Si}_3\text{N}_4$  and SiC powders, the stoichiometry varied substantially depending on the process conditions. For  $\text{Si}_3\text{N}_4$  powder, the stoichiometry ranged from nearly pure  $\text{Si}_3\text{N}_4$  (< 1.0 wt.% excess Si) to  $\text{Si}_3\text{N}_4$  + 60 wt.% excess Si. Near stoichiometric values are caused by increased laser intensity, increased pressure, and lower gas stream velocities.  $\text{C}_2\text{H}_4/\text{SiH}_4$  runs produced SiC powders with up to 10 wt.% excess C or Si. The more stoichiometric powders were produced with increased laser intensity and close to stoichiometric

reactant gas ratios. In both the  $\text{Si}_3\text{N}_4$  and  $\text{SiC}$  powders, it appears the excess Si and C are distributed uniformly throughout the individual particles.

Except when synthesized under very low laser intensities, the Si powders are crystalline. In all cases, the crystallite size was a fraction ( $1/5 - 1/3$ ) of the BET equivalent diameter, indicating the individual particles are polycrystalline. Marra found<sup>8</sup> that the particle size to grain size ratio reflected the nucleation and growth of crystals in the amorphous particles. Virtually all process conditions produced  $\text{Si}_3\text{N}_4$  powder which was amorphous. High laser intensities and high reactant pressure resulted in stoichiometric, crystalline  $\text{Si}_3\text{N}_4$  powders. All  $\text{SiC}$  powders were crystalline. Most process parameters produced polycrystalline  $\text{SiC}$  particles with the BET equivalent spherical diameter approximately twice as large as the crystallite size measured by X-ray line broadening.

Powders of other materials have not been characterized as extensively as these three nor have the interrelationships between process variables and powder characteristics been studied yet. They all have poorly developed crystalline structures or extremely small grain sizes based on X-ray diffraction analyses and have small diameters based on TEM and BET characteristics.

### II.2.C. Process Attributes

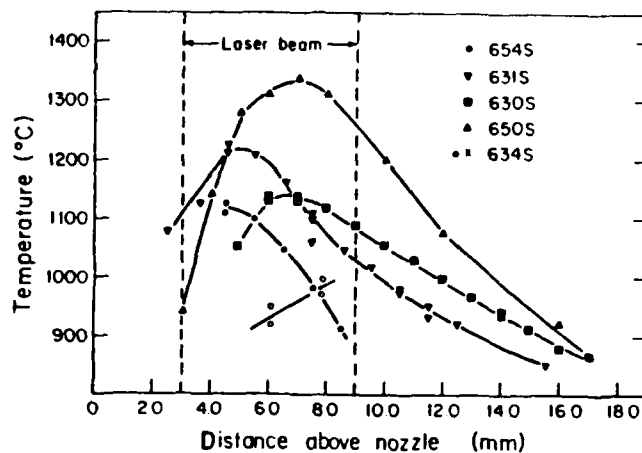
Qualitatively, it is now clear that the laser heated powder synthesis process works; in fact, it works very well. It is stable, simple, diagnosable, efficient and the resulting powder characteristics satisfy a stringent set of requirements. It is the inherent stability and the ability to make real time diagnostics that permit high quality powders to be produced, insuring they have a high value. The simplicity and both material and energy efficiencies should permit costs to reach viable levels.

Newly developed diagnostics based on light scattering and transmittance measurements permit nucleation and growth processes to be analyzed in terms of temperature and reactant partial pressures with  $< 1$  mm spacial resolution throughout the reaction zone and particulate plume. They also permit important observations about the crystalline state of the reaction product and the agglomeration process. Using an experimental technique developed by Flint<sup>7</sup> and Marra<sup>8</sup> and modifications<sup>7</sup> of computational techniques reported by

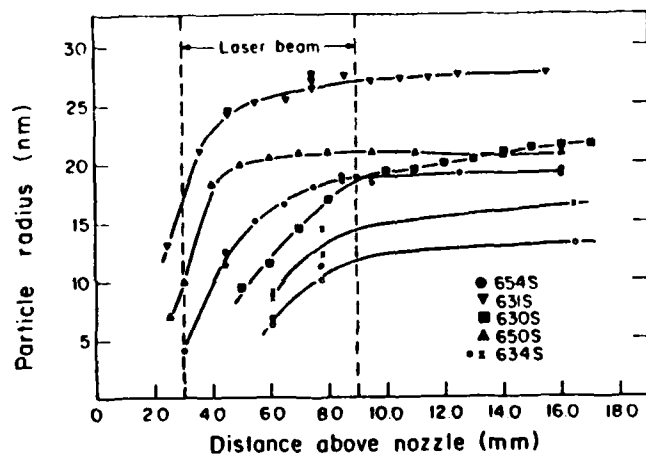
Sarofim<sup>17</sup>, it is possible to calculate the local emissivity, particle diameter and number density from the extinction and scatter-extinction ratio results. Mass balance calculations, based on local number density and particle diameter, permit the local reactant concentrations to be calculated. These, combined with local temperatures, permit reaction kinetics to be interpreted in terms of rate controlling models. They also provide a basis for real time process control. Typical results<sup>7,8</sup> are given in Figures II.3, II.4 and II.5 for Si powders made from  $\text{SiH}_4$ . The temperatures shown in Figure II.3 are calculated from the pyrometrically determined brightness temperatures and the calculated emissivities.

These calculations employ the complex index of the particulate materials which are strongly dependent on crystallinity, temperature, stoichiometry and wavelength. This variance can be used to gain insights about the reaction process. For either amorphous or polycrystalline indices, Figure II.5, the calculated number densities decrease rapidly over a distance of approximately 1 mm ( $\sim 3 \times 10^{-4}\text{s}$ ) and then remain constant. Supported by direct STEM observations and annealing studies<sup>8</sup>, these results show that the Si particles form with an amorphous structure then crystallize when the gases become hotter as they penetrate into the laser beam.<sup>7</sup> The actual number density follows the dotted line from the amorphous curve ( $\sim 3$  mm) to the polycrystalline curve ( $\sim 4.5$  mm) and remains essentially constant ( $N \approx 4 \times 10^{12}\text{cm}^{-3}$ ) throughout the growth process. The cessation of nucleation is an essential requirement for achieving the desired uniform particle size. Equally important, this result shows that agglomeration does not occur within the hot region where hard agglomerates could form in agreement with the constant particle diameter regions shown in Figure II.4. This result shows that the chainlike agglomerates probably result from being captured in the filter, extraction or preparation of TEM samples.

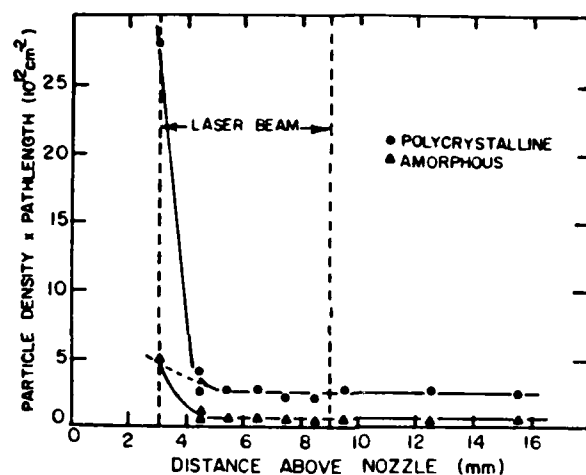
In close agreement with the simplified analyses, these direct observations show that the process is characterized by rapid heating rates ( $\sim 10^6\text{C/s}$ ), short reaction times ( $\sim 5 \times 10^{-4}\text{s}$ ) and rapid cooling rates ( $\sim 10^5\text{C/s}$ ). The high heating rates cause high nucleation rates and consequently small particle sizes. The short time at high temperatures minimizes problems with forming hard agglomerates when particles collide through Brownian motion. The cooling rates are fast enough to quench non-equilibrium structures. The maximum exposure temperature can also be



II.3. Temperature versus distance from nozzle for several Si synthesis runs.<sup>7,8</sup>



II.4. Particle size versus distance from nozzle for several synthesis runs.<sup>7,8</sup>



II.5. Particle number density versus distance from nozzle for a typical Si synthesis run.<sup>7,8</sup>

precisely controlled largely independent of heating and cooling rates. This unusual feature permits the powder's crystalline state to be manipulated. In combination, the attributes of this process constitute a very precise means of producing ceramic powders.

The costs of manufacturing powders by the laser heated processes have been estimated and compared to conventional powders. The results are very encouraging.

Our manufacturing cost estimates are based on the simplified technique described by Aries and Newton.<sup>18</sup> Material, utility, energy and labor costs are treated conventionally. The major simplification is that the plant cost is assumed to be a multiple of the equipment cost and that annualized plant cost is  $0.202 \times$  total plant cost. Chemical engineering experience shows that the "plant cost" multiple should be 4.74 for a fluid process; lower multiples are used for simpler, non hermetic processes. Labor costs are treated as  $1.79 \times$  direct salaries and annual building costs as  $0.052 \times$  total building costs.

This analysis was based on a single gas tip since this would be the scaling unit for a plant. It presumed most of the same operating conditions we employ with the laboratory scale process; they are summarized in Table II.3. The assumed 2.0 cm diameter gas tip is the only significant



**TABLE II.3**  
**MANUFACTURING RATES AND COSTS**

● Assumptions

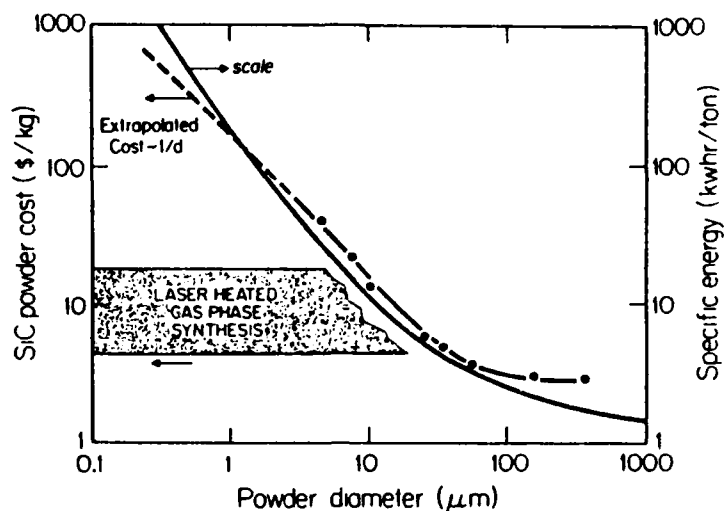
Gas tip diameter        = 2.0 cm  
 Gas velocity            = 500 cm/sec  
 Gas pressure            = 1 atm  
 Reaction efficiency     = 100 %  
 Capture efficiency      = 100%  
 Operational efficiency = 91% (8000 hr/yr)  
 Heating -  
     0 - 700°C by resistance  
     700 - 1000°C by laser  
     no heat recovery

● Results	<u>Si</u>	<u>Si<sub>3</sub>N<sub>4</sub></u>	<u>SiC</u>
Production rate: kg/hr	7.2	5.1	6.8
ton/yr	57.6	40.8	54.4
Laser power requirement (kW)	1.5	1.3	1.5
Total process energy (kWhr/kg)	1.8	2.1	1.9
Costs (\$/kg)			
Labor	0.77	1.09	0.82
Plant	1.66	2.34	1.76
Building	<0.01	<0.01	<0.01
Utilities	0.19	0.25	0.21
Raw materials	2.28-22.80	1.62-13.95	1.77-16.17
Total	4.29-25.44	5.32-17.65	4.57-18.97

departure from current practice. This value is approximately the maximum laser beam penetration depth that can produce uniform local intensities with multiple, radially apposed laser beams. The assumed reaction and powder capture efficiencies reflect our current values. We presumed that preheated gases would be injected into the laser beam to minimize unnecessary laser heating; but, no heat recovery was assumed. The plant was scheduled for full time operation (8760 hrs/yr maximum) and assumed to actually produce 91% of available time (8000 hrs/yr). Four full shifts having one person for three tips was assumed. Current bulk costs for  $\text{NH}_3$  (0.52 \$/kg) and  $\text{C}_2\text{H}_4$  (0.5 \$/kg) were used for these materials. Silane costs were estimated informally from several sources.<sup>19,20,21</sup> The cost analysis was done based on a silane cost of 2.0 and 20.0 \$/kg. A figure of 10-15 \$/kg appears reasonable for silane with somewhat higher impurity levels than semi-conductor grades.

The results of the manufacturing cost analysis are given in Table II.3. They show that the assumed process configuration is well matched to available  $\text{CO}_2$  laser equipment. The presumed gas tip diameter and gas flow rate require lasers in the 1.5 kW range. Also, the output per tip is 40-57 tons per year; a level that is well into a viable manufacturing scale. Finally, calculated manufacturing costs range from 4.30 to 25.00 \$/kg depending mostly on the silane cost. The dominance by raw material costs will be true of other gas phase processes using these materials. Their distinctions will be the quality of the resulting powders. These costs pose questions regarding the accuracy of the analysis, the opportunities for cost reduction and the relative costs of conventional materials.

Generally we feel that the cost projection is conservative. The only factor not considered is maintenance. The "plant cost" estimating factor appears too high because the required equipment cost is made up largely of a single, easily installed laser. For instance, equipment having the optics and laser power assumed in this analysis was just designed and constructed at M.I.T. on a first time basis for much less than half of the ~ \$470,000 figure used in the calculation. We believe this cost will be less than indicated. More importantly, there are many opportunities for reducing the raw material costs made possible by changing chemistries. Our initial choice of silane as a silicon source made no consideration of cost. A major task in our new "scale up" research program will be the consideration of alternative reactants.



II.6 Sales price in 5000 kg lots for Acheson SiC powder<sup>22</sup>, specific comminution energy<sup>23</sup> and manufacturing cost for SiC powders made from laser heated gases as functions of particle size.

Figure II.6 summarizes present sales prices of Acheson SiC in 5000 kg lots as a function of particle size.<sup>22</sup> The price is essentially constant for powder sizes greater than 100  $\mu\text{m}$ . Below 100  $\mu\text{m}$ , the cost increases rapidly with decreasing particle size. A  $1/d$  extrapolation was used to project prices into the submicron range needed for sintering. Also shown in Figure II.6, is a generalized curve of comminution energy per unit mass as a function of particle size.<sup>23</sup> For coarse powders, it is independent of particle size; for fine and ultrafine powders it usually increases with decreasing particle size at a rate between  $1/d$  and  $1/d^2$ . The similarity between the two curves is striking; although, it should be noted that the values of these specific comminution energies constitute a small fraction of the sales prices. The manufacturing costs for powders made by a comminution process must follow curves having shapes similar to those shown in Figure II.6 and also they cannot be displaced very much for profit factors. The "coarse", constant cost is largely set by energy and handling costs, the diameter dependence usually begins between 5 and 100  $\mu\text{m}$ , below that, costs increase at rates between  $1/d$  and  $1/d^2$ . These powders will have the typical broad particle size distribution and contaminations resulting from comminution processes.

Our SiC manufacturing cost estimate range is shown in Figure II.6 for comparison with commercial powders. These costs are independent of particle diameter because controlling the nucleation process has no obvious consequence to equipment costs or mass flow rates. Even with probably higher than actual cost figures, the laser heated gas phase synthesis process has a much lower manufacturing cost than the sales price of present submicron SiC powders. Also, these powders have a narrow size distribution and are free of unwanted contaminants.

### II.3. CONCLUSIONS

The conclusions are straight forward and are very optimistic. A new powder process has been developed. It is simple, stable, controllable on a real-time basis and applicable to many materials. The characteristics of the resulting powders satisfy criteria for an ideal powder and individual properties can be manipulated. Projected manufacturing costs are lower than conventional powders. It appears to us that this new process is capable of producing better materials at lower cost than are presently available.

### II.4. ACKNOWLEDGEMENTS

Numerous staff and students have contributed to the success of this work. Hopefully, all are properly referenced. This research has largely been sponsored by DOD through DARPA, ONR and AROD. More recently NASA-Lewis, Standard-Oil (Indiana), Corning Glass Works and the 3M Corporation have supported portions of this work. All contributions are gratefully acknowledged.

## II.5. REFERENCES

1. Cannon, W. R., Danforth, S. C., Flint, J. H., Haggerty, J. S., Marra, R. A., "Sinterable Ceramic Powders from Laser Driven Reactions; Part I: Process Description and Modeling", J. Am. Ceram. Soc., 65, 7, 324-30 (1982).
2. Cannon, W. R., Danforth, S. C., Haggerty, J. S., and Marra, R. A., "Sinterable Ceramic Powders from Laser Driven Reactions; Part II: Powder Characteristics and Process Variables", J. Am. Ceram. Soc., 65, 7, 330-5 (1982).
3. Haggerty, J. S., "Sinterable Powders from Laser Reactions", MIT-EL 82-002, Final Report N00014-77-C-0581, September 1981.
4. Danforth, S. C., and Haggerty, J. S., "Synthesis of Ceramic Powders by Laser Driven Reactions", Ceramic Engineering and Science Proceedings, 2, 7-8, 466-79 (1981).
5. Marra, R. A., and Haggerty, J. S., "Synthesis and Characteristics of Ceramic Powders made from Laser-Heated Gases", Ceramic Engineering and Science Proceedings, 3, 1-2, (1981).
6. Haggerty, J. S., "Synthesis of Powders and Thin Films by Laser Induced Gas Phase Reactions", presented at the Nineteenth University Conference on Ceramic Science, Emergent Process Methods for High Technology Ceramics, November 8-10, 1982. To appear in the Proceedings of the Nineteenth University Conference on Ceramic Science, Materials Research Series, Plenum Publishers.
7. Flint, J. H., "Powder Temperature in Laser Driven Reactions", M.S. Thesis, M.I.T., February 1982.
8. Marra, R. A., "Homogeneous Nucleation and Growth of Silicon Powder from Laser Heated Gas Phase Reactants", Ph.D. Thesis, M.I.T., February 1983.
9. Suyama, Y., Marra, R. A., Haggerty, J. S., and Bowen, H. K., "Synthesis of Ultrafine SiC Powders by Laser Driven Gas Phase Reactions". Submitted for publication to the J. Am. Ceram. Soc., October 1982.
10. Golino, C., Haggerty, J. S., and Bowen, H. K., "Gas Phase, Laser Driven Ceramic Powder Synthesis: SiC and Silicon Carbonitrides from Monomeric Organosilicon Precursors". To be presented at the 1983 Annual Meeting of the American Ceramic Society, April 1983.
11. Gattuso, T. R., Golino, C., Haggerty, J. S., and Bowen, H. K., "Synthesis of  $Al_2O_3$  Powders From Laser Heated Organometallic Precursors. To be submitted to the J. Am. Ceram. Soc.

12. Barringer, E., Jubb, N., Fegley, B., and Bowen, H. K., "Processing with Monodispersed Powders", presented at the International Conference on Ultrastructure Processing of Ceramics, Glasses and Composites", February 13-17, 1983, Gainesville, Florida.
13. Gattuso, T. R., Meunier, M., Adler, D., and Haggerty, J. S., "IR Laser-Induced Deposition of Silicon Thin Films", to be published in the Proceedings of the Symposium on Laser Diagnostics and Photochemical Processing for Semiconductor Devices, November 3-4, 1982.
14. Greskovich, G., and Rosolowski, J. H., "Sintering of Covalent Solids", J. Am. Ceram. Soc., 59, 285-8 (1976).
15. Mizuta, S., Cannon, W. R., Bleier, A. and Haggerty, J. S., "Wetting and Dispersion of Silicon Powder Without Deflocculants", Am. Ceram. Soc. Bull., 61, 872-5 (1982).
16. Danforth, S. C., (Rutgers University) and Dahlen, M., (Volvo, Sweden), unpublished results.
17. D'Slessio, A., Dilorenzo, A., Sarofim, A. F., Beretta, F., Masi, S., and Venitozzi, C., "Soot Formation in Methane-Oxygen Flames", Fifteenth Symposium (international) on Combustion (1975) 1427, The Combustion Institute, Pittsburg, PA.
18. Aries, R. S., and Newton, R. D., Chemical Engineering Cost Estimation, Chemonomics, Inc., N.Y., April 1951.
19. Baney, R. H., Dow Corning, private communication.
20. Chambers, F., Standard Oil Co. (Indiana), private communication.
21. Orinsnshky, P., Union Carbide Co., private communication.
22. Cannon, R., M.I.T., private communication.
23. "Comminution and Energy Consumption", National Materials Advisory Board (NAS-NAE), PB81-225708, May 1981

## CHAPTER III

### POWDER TEMPERATURE, SIZE, AND NUMBER DENSITY IN LASER DRIVEN REACTIONS

by

J. H. Flint, R. A. Marra, and J. S. Haggerty

#### ABSTRACT

A technique to accurately measure the temperature of powders in a laser driven reaction has been developed. Particles are formed by heating reactant gases with a 150 watt  $\text{CO}_2$  laser. The brightness temperature of the particulate cloud was measured with a micro-optical pyrometer. The emissivity was determined from scattering and transmission measurements. A correction for high turbidity was derived. The scattering and transmission measurements also allow the determination of the size and number density of the particles. The temperature and particle size as a function of height are reported for five silicon powder reaction conditions, and for one silicon carbide reaction.

The measurements indicate that particles are often nucleated before the reactant gas has reached the  $\text{CO}_2$  laser beam. The reaction zone temperature decreases once most of the reactant gas is consumed, unless the produced powder absorbs  $10.6 \mu\text{m}$  radiation as does  $\text{SiC}$ . The silicon particles nucleate as amorphous silicon, and then crystallize as they move into hotter regions of the reaction zone.

#### III.1. INTRODUCTION

A method of producing sinterable powders through the heating of gases with a  $\text{CO}_2$  laser has been developed which has potential application in the manufacture of silicon nitride and silicon carbide as well as other high temperature ceramics.<sup>1,2</sup> Although variation in the product powder characteristics have been studied extensively as a function of process parameters, the properties of the reaction itself have been more difficult to characterize. The most important of these properties are: the thermal

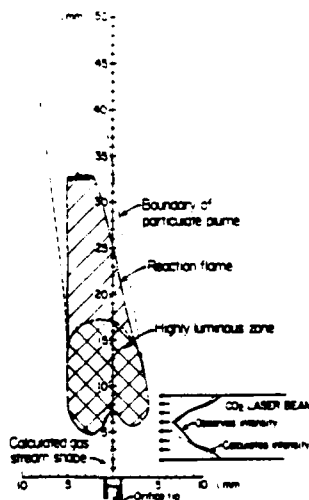
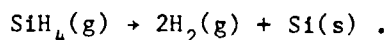
range within which the reaction takes place; and the evolution in time (and space) of the particle size, particle number density, and crystallinity.

This paper describes a technique that has been developed and used to rapidly and accurately measure these properties with a spatial resolution of 1 mm. Results for the laser synthesis of silicon and silicon carbide powders are also presented.

### III.2. EXPERIMENTAL APPARATUS AND METHODOLOGY

The powder synthesis process involves passing a jet of reactant gases through a CW CO<sub>2</sub> laser beam inside a controlled atmosphere reaction cell. Figure III.1 is a schematic of the reaction zone. The reactant gases and the CO<sub>2</sub> laser beam intersect at the center of the cell. The gas is heated rapidly, and reacts to form small particles, which are swept out of the cell and captured in a filter. Argon is injected in a concentric annular flow at the base of the nozzle to constrain the reactant gases in a narrow stream and to carry the products to the filter.

By this method, silane gas is converted into silicon powder by the simple overall reaction:



III.1. Schematic of the reaction zone.



The resulting silicon powder is ideal for forming reaction-bonded silicon nitride because of its small particle size (10-250 nm diameter depending on process parameters), very narrow size distribution, high purity, and loose agglomeration. The same technique has been used to produce silicon nitride<sup>1</sup> and silicon carbide powders<sup>2</sup>.

To measure the process parameters of interest, an apparatus based on a HeNe probe laser was developed. The extinction and scattering of the polarized HeNe beam by the cloud of particles provide the needed data<sup>3</sup>, by the following methodology.

Optical pyrometry determines the brightness temperature,  $S$ , of a radiating body, at a single wavelength. The absolute emissivity,  $\epsilon$ , of the area being viewed must be known before the true temperature can be calculated. This can be readily seen from Wien's approximation to the Plank Radiation Law written<sup>4</sup> in terms of the radiance,  $N_\lambda$ , and the brightness temperature,  $S$ , and the true temperature,  $T$ :

$$N_\lambda = \frac{C_1 \epsilon e^{(-C_2/\lambda T)}}{\lambda^5} = \frac{C_1 e^{(-C_2/\lambda S)}}{\lambda^5} \quad (1)$$

If the emissivity is known, the true temperature  $T$  can be found by rearranging Equation 1 to yield:

$$\frac{1}{T} = \frac{1}{S} + \frac{\lambda \ln \epsilon}{C_2} \quad (2)$$

The accuracy of the true temperature calculation is essentially equal to the accuracy of the brightness temperature measurement ( $\pm 10^\circ\text{C}$ ). This is because the emissivity calculations are insensitive to the only quantity that is not directly measured, the index of refraction of the particles.

The emissivity of a body is given by its absorptivity,

$$\epsilon = \alpha = 1 - \tau - \rho \quad (3)$$

which is the fraction of incident light that is neither reflected,  $\rho$ , nor transmitted,  $\tau$ . For a diffuse cloud of particles such as exists in the reactions of interest, light is scattered in many directions rather than reflected as one wave. It is also scattered from the interior of the cloud, rather than only at the surface. Thus, the emissivity of a cloud is:<sup>5</sup>

$$\epsilon = (1 - \tau) \left( \frac{C_{\text{abs}}}{C_{\text{ext}}} \right) \quad (4)$$

where  $C_{\text{ext}}$  and  $C_{\text{abs}}$  are, respectively, the extinction and absorption cross sections per particle. The integrated scattering cross section  $C_{\text{sca}}$  is related to  $C_{\text{abs}}$  and  $C_{\text{ext}}$  by

$$C_{\text{sca}} = C_{\text{ext}} - C_{\text{abs}} . \quad (5)$$

The cross sections are functions of the wavelength, the particle size and the complex index of refraction,  $m = n - ik$ , of the particles, and can be calculated using the Lorenz-Mie scattering equations.<sup>6</sup>  $C_{\text{ext}}$  is related to the transmissivity through

$$\tau = \frac{I}{I_0} = \exp(-\ln C_{\text{ext}}) \quad (6)$$

where  $I_0$  and  $I$  are the incident and transmitted intensities,  $N$  is the particle number density, and  $l$  is the thickness of the cloud. Using these substitutions, Equation 4 can be rewritten as

$$\epsilon = \left(1 - \frac{I}{I_0}\right) \left(1 - \frac{C_{\text{sca}}}{C_{\text{ext}}}\right) . \quad (7)$$

The first term is determined from a transmission measurement. The second term requires that the scatter-extinction ratio be measured.

If the incident and scattered light are plane polarized orthogonal to the scattering plane, the scatter-extinction ratio is defined by:

$$\frac{\dot{E}_\perp(\theta)}{E_0 \delta\Omega \ln(I_0/I)} = \frac{\lambda^2 i_\perp(\theta)}{4\pi^2 C_{\text{ext}}} , \quad (8)$$

where the quantities on the left side are measurable, and those on the right are calculable.  $\dot{E}_\perp(\theta)$  is the power scattered at angle  $\theta$  into solid angle  $\delta\Omega$  for an incident power of  $E_0$ , and  $i_\perp(\theta)$  is the Mie scattering function for light scattered at angle  $\theta$ . Equation 8 is written for the case where the transmission and scattering measurements are made simultaneously, so that the path length and number density dependencies cancel. The Mie scattering function,  $i_\perp(\theta)$ , depends on the particle radius, the particle index of refraction, and the wavelength of incident light.<sup>6</sup>

Values for  $C_{\text{ext}}$ ,  $C_{\text{sca}}$ , and  $i_\perp(\theta)$  are calculated as a function of particle radius for the values of  $\theta$  and  $\lambda$  used in the experiment with an appropriate index of refraction. The results of this calculation are

plotted as  $C_{sca}/C_{ext}$  versus  $\lambda^2 I_{\perp}(\theta)/4\pi^2 C_{ext}$ . The value of  $C_{sca}/C_{ext}$  corresponding to an experimentally measured scatter-extinction ratio is then determined from this plot. The emissivity of the portion of the cloud on which the transmission and scattering measurements were made can then be calculated from Equation 7. The particle size can be determined from a plot of the scatter-extinction ratio versus particle size. The cross sections  $C_{ext}$  and  $C_{sca}$  can be found using similar plots. Once  $C_{ext}$  and the width of the cloud have been determined, the particle number density can be calculated using Equation 6.

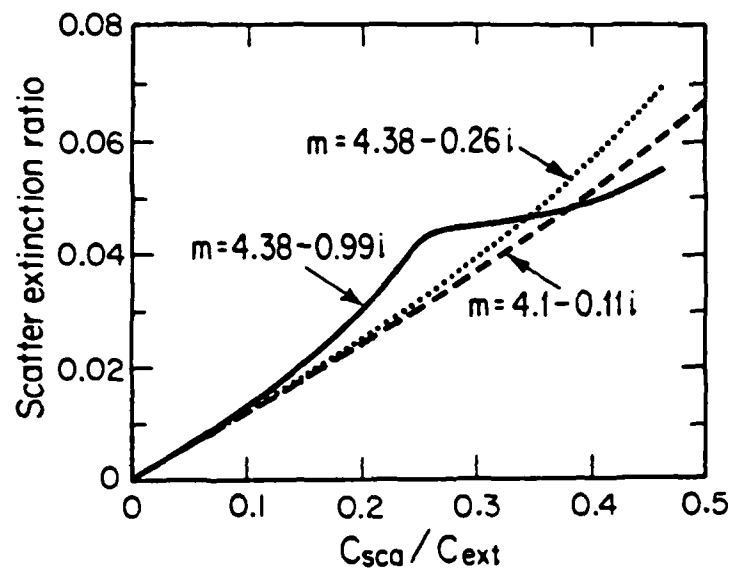
The Lorenz-Mie scattering theory can be applied to the scattering of light by a cloud of spherical particles if the following three conditions are met:<sup>7</sup>

- (a) Each particle scatters separately; that is, the particles are not agglomerated, and are separated by at least 3 radii;<sup>6</sup>
- (b) There is no optical interference among different scattered waves;
- (c) There is no multiple scattering.

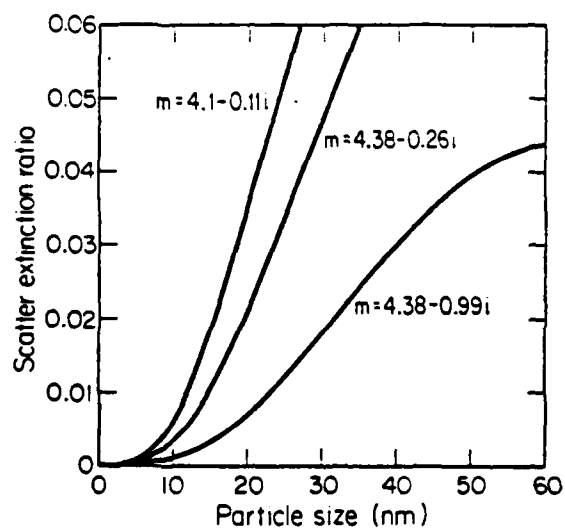
It will be shown in Section III.5 that condition (a) is true. Condition (b) is almost always valid for random systems.<sup>7</sup> But, condition (c) requires that the turbidity be less than 0.1,<sup>6</sup> and is not generally met by regions of the clouds of particles under study. The most significant result of high turbidity is a reduction of the scattered power  $\dot{E}_{\perp}(\theta)$  because both the probe beam and the scattered light from the interior of the cloud are attenuated. For small angle scattering, this effect reduces the scattered power by a factor of  $1 - (I/I_0)^2/2 \ln(I_0/I)$ . (See Appendix III.A for the derivation of this correction.) Therefore, using  $2 \dot{E}_{\perp}(\theta) \ln(I_0/I)/[1 - (I/I_0)^2]$  in place of  $\dot{E}_{\perp}(\theta)$  in Equation 8 allows the use of the Mie scattering theory even in the presence of high turbidity.

The optical properties of silicon have been studied extensively. In the visible region of the spectrum, the complex index of refraction ( $m = n - ik$ ) varies strongly with wavelength, temperature and degree of crystallinity.<sup>8-10</sup> Since the powders being studied are changing temperature rapidly, and perhaps crystallizing as they grow, a series of calculations were performed using various possible values of  $m$ .

Figures III.2 and III.3 were generated from computer calculations<sup>11</sup> of the Mie scattering functions and cross sections using three different values



III.2. Scatter-extinction ratio versus  $C_{sca} / C_{ext}$ .



III.3. Scatter-extinction ratio versus particle radius.

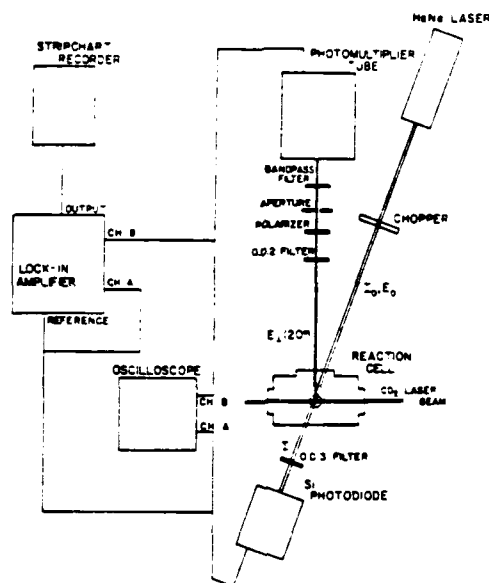
for the index of refraction. An index of  $n = 4.1 - 0.113i$  is appropriate for polycrystalline silicon at 500°C,<sup>10</sup> and  $n = 4.38 - 0.99i$  is for amorphous silicon at 500°C.<sup>10</sup> An extrapolated value of  $n = 4.38 - 0.26i$  should be valid for polycrystalline silicon around 1100°C or for a polycrystalline-amorphous mix at some lower temperature. Figure III.2 shows the calculated scatter-extinction ratios versus  $C_{sca}/C_{ext}$  for  $\theta = 20^\circ$ . It is apparent that the relationship between the scatter-extinction ratio and  $C_{sca}/C_{ext}$  is independent of the index up to a ratio of approximately 0.025. The  $C_{sca}/C_{ext}$  values remain close to one another for the two polycrystalline indices for higher values of the ratio. At a scatter-extinction ratio of 0.04, the maximum uncertainty in  $\epsilon$  results in a true temperature difference of only 26°C for a brightness temperature of 1100°C (~ 2.5%). This indicates that even though the index as a function of position in the reaction zone is not precisely known, the emissivity and the temperature can still be determined to high accuracy.

Figure III.3 is a plot of the scatter-extinction ratio versus particle radius for the same three indices. A much larger dependence on index is noted. Although this introduces some uncertainty to the absolute particle size and number density calculations, this is not a serious problem since the final particle size can be measured by BET surface area analysis and transmission electron microscopy. Without question, the scatter-extinction measurements can be used to monitor changes in particle size and number density throughout the reaction. It may also be possible to extract information on the variation of the index of refraction of the particles within the reaction zone from the scatter-extinction measurements as a function of position.

### III.3. EXPERIMENTAL PROCEDURE

A HeNe laser is used as the probe in an apparatus that simultaneously measures the extinction of the HeNe laser beam and the intensity of the scattered light at an angle of 20°. Figure III.4 is a schematic of the optical layout.

The 5 mW vertically polarized HeNe laser is mounted on a cathetometer, enabling measurements to be made as a function of height by simply translating the laser. The transmitted HeNe laser light,  $I$ , is measured by



III.4. Scatter-extinction optical layout.

TABLE III.1  
POWDER SYNTHESIS REACTIONS STUDIED

Run #	Cell Pressure (atm)	Reactant Gas Flow Rates			Particle Radius by BET (nm)
		Silane (cc/min)	Argon (cc/min)	C <sub>2</sub> H <sub>4</sub> (cc/min)	
631S	0.2	38	0	0	30.5
654S	0.2	13	25	0	17.5
634S	0.2	6.5	31	0	14.8
630S	0.2	109	0	0	22.2
650S	0.6	66	0	0	73.5
910S1C	0.6	36	0	20	17.0

a silicon photodiode mounted on an x-y translator. The scattered HeNe light,  $\dot{E}_\perp(20^\circ)$ , is detected by an RCA C53050 photomultiplier. An 8.13-mm-diameter aperture determines the solid angle viewed, which is  $2.23 \times 10^{-4}$  steradians. Focussing optics are not used to minimize alignment problems as the probe laser is moved. A 632.8 nm bandpass filter passes the HeNe laser light, but rejects most of the thermal emission from the reaction zone. A vertical polarizer analyzes the polarization of the scattered light. The incident probe laser power,  $E_0$ , was measured by directing a calibrated fraction of the HeNe laser beam through the same collection filters to the photomultiplier using a beam splitter temporarily mounted at the center of the reaction cell.

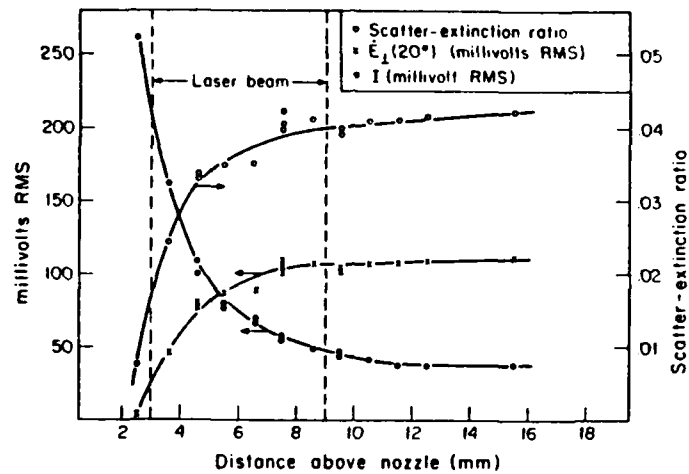
A micro optical pyrometer (made by Pyrometer Instruments, Inc.) is mounted alongside the photodiode so that it views the reaction zone in the scattering plane. The field of view of the pyrometer is such that a  $1 \text{ mm}^2$  area is monitored.

At each height the following sequence of adjustments and measurements is required: the cathetometer is set to the desired height; the photodiode is adjusted with its x-y translator for peak signal;  $I$  and  $\dot{E}_\perp(20^\circ)$  are measured with the lock-in amplifier; the optical pyrometer is focussed on the point where the HeNe beam intersects the reaction zone, then the HeNe laser is blocked while a temperature reading is made. In this way the scattering, extinction, and brightness temperature measurements are all made on the identical volume of the reaction zone.

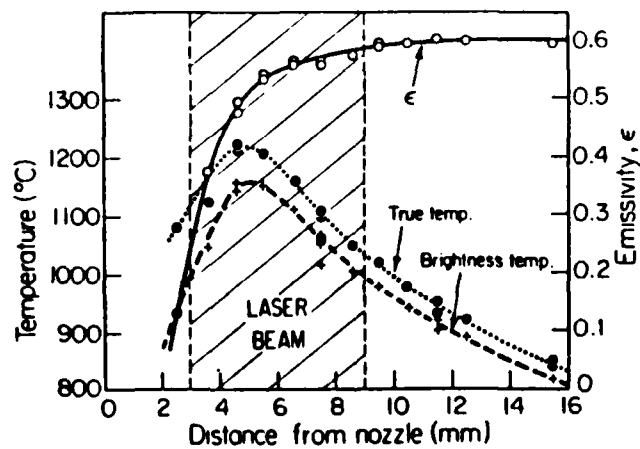
#### III.4. RESULTS AND DISCUSSION

Measurements were made on laser-heated silicon powder synthesis reactions under a range of process conditions. Table III.1 lists the parameters of the reactions studied and the equivalent particle sizes determined by BET surface area analysis for similar runs.<sup>1</sup>

Figure III.5 is the measured scattered power,  $\dot{E}_\perp(20^\circ)$ , and transmitted intensity,  $I$ , in millivolts RMS for Run 631S as a function of position above the reactant gas nozzle. The scatter-extinction ratio is also plotted. Figure III.6 shows the emissivity,  $\epsilon$ , the brightness temperature,  $S$ , and the true temperature,  $T$ , as a function of position for the same reaction.

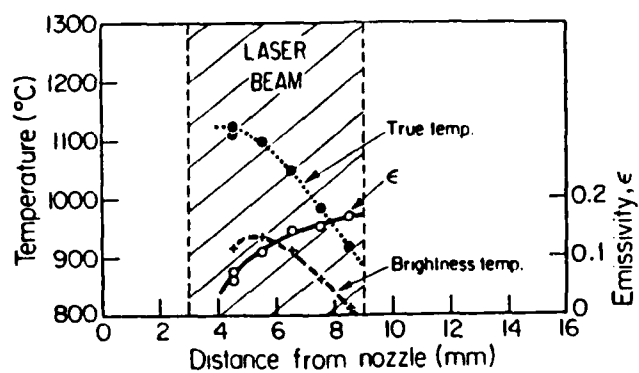


III.5.  $I$ ,  $E_{\perp}(20^{\circ})$ , and scatter-extinction ratio for run 631S.

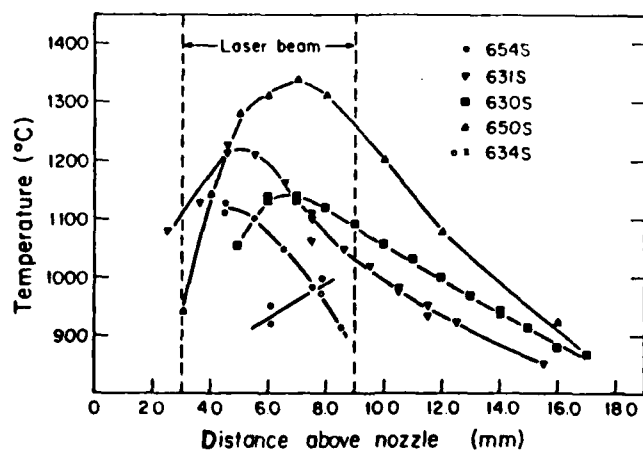


III.6. Temperature and emissivity for run 631S.

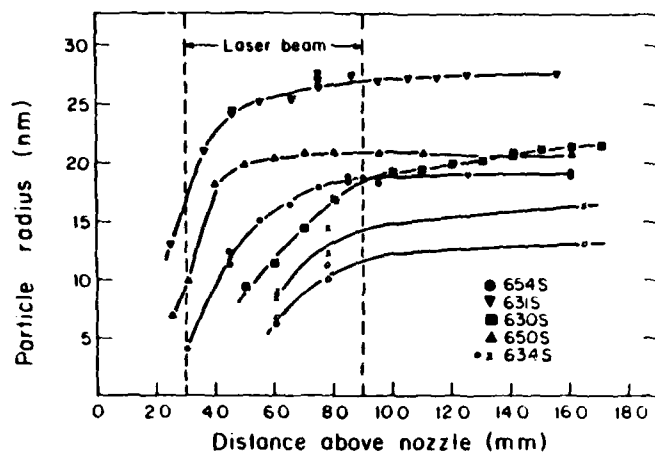




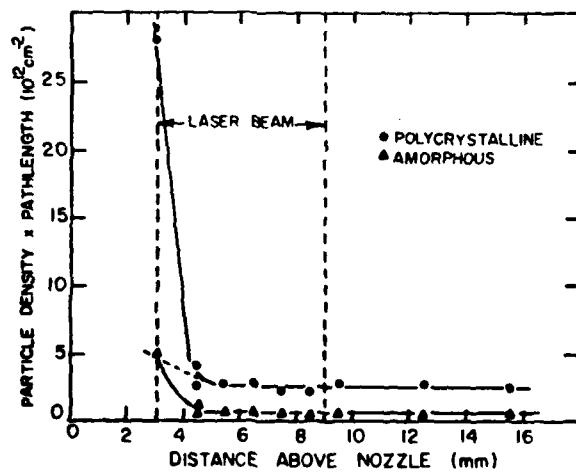
III.7. Temperature and emissivity for run 654S.



III.8. Temperature versus distance from nozzle.



III.9. Particle size versus distance from nozzle.



III.10. Particle number density versus distance from nozzle.

Figure III.7 shows  $\epsilon$ , S, and T for Run 654S. These plots are representative of the data from the other runs. Figure III.8 summarizes the true temperature distributions for all of the reactions studied. Figure III.9 summarizes the calculated particle sizes.

The number density of particles as a function of position in the reaction zone is presented in Figure III.10 for Run 654S. Two different calculations are presented, since the calculated number density is a strong function of the value of the index of refraction used.

Figures III.8 and III.9 reveal that the heating of the reactants is rapid, and the reaction is often underway before the reactants intersect the  $\text{CO}_2$  laser beam. In the case of Runs 650S and 631S, the measured temperatures at the edge of the laser beam are over  $900^\circ\text{C}$ .

Possible heating mechanisms of the gas below the  $\text{CO}_2$  laser beam are thermal conduction from the hot zone, and resonant emission from vibrationally excited  $\text{SiH}_4$  molecules in the hot zone. The maximum rate of infrared emission from the reaction zone can be calculated from the Planck radiation law. At  $\lambda = 4 \mu\text{m}$ , and  $1100^\circ\text{C}$ , the emission rate is about  $3 \text{ W/cm}^2/\mu\text{m}$ . If the width of the  $4 \mu\text{m}$  silane absorption band is  $0.33 \mu\text{m}$ ,  $1.0 \text{ W/cm}^2$  could be transferred by radiation. Hot bands, and the  $10 \mu\text{m}$  band will also contribute to some extent. Thermal conductivity across a 3-mm gap of silane is about  $2 \text{ W/cm}^2$  for a  $1000^\circ$  temperature difference. From this simple analysis it appears that both thermal conductivity and vibrational radiation from excited silane molecules are significant in the preheating of the reactants.

Figure III.8 also indicates that for all reaction conditions studied the temperature of the silicon powder begins decreasing while the particles are still in the  $\text{CO}_2$  laser beam, suggesting that the particles themselves are not strongly heated by the laser. As Figure III.9 shows, virtually all of the particle growth takes place within the  $\text{CO}_2$  laser beam. Note that the continuing growth in Run 630S is due to the high silane concentration and flow rate. Once most or all of the silane has reacted to form solid silicon, the gas/powder mixture stops absorbing and starts to cool off. Since silane decomposition starts around  $800^\circ\text{C}$ , most of it is consumed at temperatures significantly below the silicon melting point.

Since the particle size determinations are sensitive to the index of refraction, the quantitative conclusions based on these measurements must be

more tentative. It is clear that the particles grow rapidly, and that the growth process usually terminates within the  $\text{CO}_2$  laser beam volume. Significant growth past the laser beam only occurs at the high concentration and/or flow rates (as in Run 630S and 631S). For the undiluted 0.2 atm runs, agreement between these measurements and BET size measurements is good, suggesting that the polycrystalline indices extrapolated above  $500^\circ\text{C}$  are the best choice. For diluted reactions, which are not as hot, better agreement is obtained when the lower temperature indices are used. The overall good agreement indicates that the high turbidity correction is reasonably good for turbidities up to about 2.

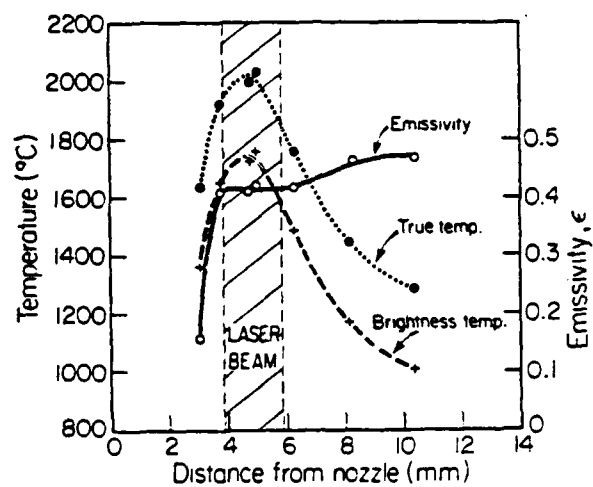
The run at 0.6 atm (650S) requires additional interpretation. The measured particle size is much smaller than the BET results. However, since the turbidity of this reaction is around 6, it is quite possible that the turbidity correction is not accurate at very high turbidities. The other two conditions for the validity of Mie scattering should still hold. Another explanation is that, for such a turbid cloud, virtually all of the detected scattering comes from the outer edge, where the silane reactant is the most strongly diluted with argon. Since diluted conditions produced smaller particles, it is likely that small particles are created at the edges of the reaction zone. The effect of this would be to reduce the scatter-extinction ratio, leading to a small calculated particle size.

Finally, the leveling off of the scatter extinction ratio, hence the particle size, under all conditions indicates that the large loose agglomerates that are typical of the powder after it has been collected in the filter are produced by the collection process. This justifies the assumption that condition (a) for Mie scattering is valid. It also suggests that a liquid collection process should produce a monodisperse suspension of silicon particles. This would allow the fabrication of uniform high density compacts, which would have much improved sintering properties.

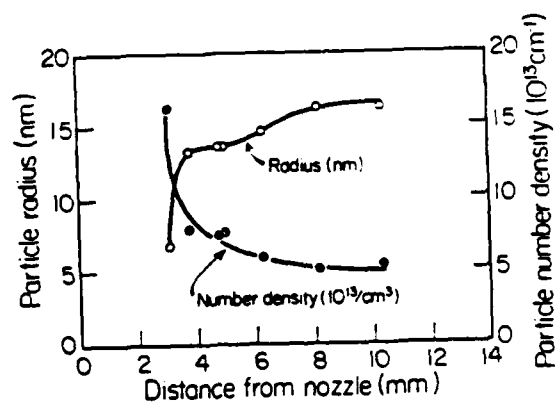
The particle number density calculations are extremely sensitive to the value of the refractive index used in the calculation. A calculation based on a constant index indicates that the number density decreases from a maximum value at the inception of the reaction to a constant value (Figure III.10). Several factors can contribute to the apparent decrease in number density from levels calculated at the base of the reaction zone. Although expansion of the reactant gases with heating is a factor, the

number density change is too great for this to be solely responsible. Small particles could be agglomerating as they move into the  $\text{CO}_2$  laser beam. We feel this is unlikely because there is no reason why the agglomeration process would terminate abruptly, particularly before the reaction had neared completion. Figure III.9 shows that the major portion of the reaction occurs via growth after the number density has reached a constant value. The final explanation is that the particles are amorphous at the base of the reaction zone and crystallize as they grow while travelling into the hotter regions of the zone. Under this assumption, the number density curve would be a combination of the amorphous curve and the polycrystalline curve, as shown by the dashed line in Figure III.10. The transition corresponds to the region within the zone where the amorphous particles crystallize. The temperature at the end of the transition, 4.5 mm from the nozzle, was  $1120^\circ\text{C}$ . At the beginning point, 3 mm from the nozzle, the reaction zone was not luminous, so the temperature there is unknown. A linear extrapolation of the temperature indicates  $750^\circ\text{C}$ , which is probably an upper limit. This low temperature is consistent with the formation of amorphous silicon, just as  $1120^\circ\text{C}$  is consistent with polycrystalline silicon formation. The formation of amorphous powders and their progressive crystallization is therefore probably responsible for the apparent number density decrease with height when a constant refractive index is assumed. The dashed line in Figure III.10 indicates a relatively constant number density.

Preliminary scatter-extinction and temperature measurements have been performed on SiC powders made from  $\text{SiH}_4$  and  $\text{C}_2\text{H}_4$ . Figure III.11 shows the brightness temperature, true temperature, and emissivity for a typical silicon carbide synthesis run. The run conditions are listed in Table III.1. As was observed in the silane reaction, the heating of the reactants is very rapid and the reaction is initiated significantly before the reactants enter the laser beam. The emissivity increased rapidly until a nearly constant value was achieved. The temperature distribution within the laser-irradiated region was sufficiently similar in shape to the Gaussian intensity distribution of the laser beam to suggest that, unlike the silane synthesis process, the SiC particles are heated directly by the  $\text{CO}_2$  laser beam.



III.11. Temperature and emissivity for Run # 910SiC.



III.12. Particle size and number density for Run # 910SiC.

The calculated particle radius is shown in Figure III.12. The high temperature optical properties of  $\text{SiC}^{12}$  are not precisely known, and the imaginary part varies strongly with small departures from stoichiometry. Therefore a series of calculations using various values for the refractive index was carried out; the set of calculations that produces a final particle size that agrees the closest with the BET value is plotted in Figure III.12. It is evident that the nucleation and growth processes are nearly complete by the time the particles reach the laser beam, suggesting a very rapid growth rate. Better data on the SiC optical properties should enable more accurate comparisons between the scatter-extinction results and the particle size determined by other analytical techniques.

Figure III.12 also shows a plot of the particle number density,  $N$ , as a function of position in the reaction zone. The calculated number density decreased from a maximum value at the base of the reaction zone and continues to decrease slightly as the particles travel further from the inlet nozzle. The decrease in particle number density may indicate the particles are agglomerating within the reaction zone or, as suggested in the silicon synthesis, the particles may initially form as amorphous SiC and crystallize in the hotter regions of the reaction zone. A transition from silicon rich to nearly stoichiometric SiC would also explain this decrease. A more detailed study is required to interpret these results with respect to the particle formation mechanisms.

### III.5. CONCLUSION

The analytical techniques presented here are applicable to the accurate determination of the temperature distribution and average particle size and number density of a cloud of particulates, including silicon, silicon carbide or silicon nitride, produced in a  $\text{CO}_2$  laser-driven reaction. While the technique has been primarily used to study the production of Si powder from silane gas, an equivalent study of the SiC and  $\text{Si}_3\text{N}_4$  reactions requires only some idea of their high-temperature optical properties. This technique is relatively insensitive to the optical thickness of the cloud, or to whether the individual particles primarily absorb or scatter light (although a finite absorption cross section is required).

### III.6. ACKNOWLEDGEMENTS

This research was funded by ONR/ARO Contract No. N00014-82-K-0350, 1982-1984, and by NASA/Lewis under Contract No. NSG 7645. We would like to thank Professor Adel Sarofim for the gift of the computer program and helpful discussions. We are also indebted to Professor Tom Eager for the loan of the HeNe laser and for letting us use his computer facility.



### III.7. REFERENCES

1. W. R. Cannon, S. C. Danforth, J. H. Flint, J. S. Haggerty and R. A. Marra, "Sinterable Ceramic Powders from Laser Driven Reactions, Part I: Process Description and Modelling", J. Am. Ceram. Soc., **65**, 7, 330-5 (1982).
2. Y. Suyama, R. M. Marra, J. S. Haggerty and H. K. Bowen, "Synthesis of Ultrafine SiC Powders by Laser Driven Gas Phase Reactions", submitted for publication, J. Am. Ceram. Soc.
3. The scatter-extinction technique was developed to study soot particles in hydrocarbon flames. A. D'Alessio, A. D'lorenzo, A. F. Sarofim, F. Beretta, S. Masi, and C. Venitozzi, "Soot Formation in Methane-Oxygen Flames", Fifteenth Symposium (International) on Combustion (1975) p. 1427, The Combustion Institute, Pittsburg, PA.
4. G. A. W. Rutgers, and J. C. DeVos, "Relation between Brightness Temperature, True Temperature and Colour Temperature of Tungsten", Physica, **20**, 715-20 (1954).
5. T. M. Lowes and A. J. Newall, "The Emissivities of Flame Soot Dispersions", Combustion and Flame, **16**, pp. 191-4 (1974).
6. M. Kerker, The Scattering of Light and Other Electromagnetic Radiation, Academic Press (1969).
7. A. R. Jones, Prog. Energy Combustion Science, **5**, p. 73 (1979).
8. W. C. Dash and R. Newman, "Intrinsic Optical Absorption in Single-Crystal Germanium and Silicon at 77°K and 300°K", Phys. Rev., **99**, pp. 1151-5 (1955).
9. Ch. Kuhl, H. Schlotterer, and F. Schwedfsky, "Optical Investigation of Different Silicon Films", J. Electrochemical Soc.: Solid-State Science and Technology, **121**, pp. 1496-1500 (1974).
10. M. Janai and B. Karlson, "Temperature Variation of the Absorption Edge of CVD Amorphous and Polycrystalline Silicon", Solar Energy Materials, **1** (1979) pp. 387-95.
11. Koon Gee Neoh, "Soot Burnout in Flames", S. D. Thesis, M.I.T., October, 1980.
12. S. Nishino, H. Matsunami, and T. Tanaka, "Optical Properties of  $\beta$  Si:C Crystals Prepared by Chemical Vapor Deposition", Japan Journal of Applied Physics, **14**, 1833-4 (1975).

# APPENDIX III.A.

## Correction for High Turbidity in Scattering Measurements

The derivations from Lorenz-Mie Scattering theory are valid only when the three conditions cited in the text for single scattering are met. If the probe beam is attenuated significantly by the cloud, the last volume element will experience an incident power less than  $E_0$ , so it will scatter less light than does the first volume element. In small angle scattering, the light from the last volume element of the cloud will have to travel back through the cloud, being further attenuated. From Lorenz-Mie theory, the light scattered at position  $p$ ,  $\dot{E}(\theta, p)$  is

$$\dot{E}(\theta, p) = N C_{sca}(\theta) E(p) \delta\Omega \delta p, \quad (A-1)$$

where  $N$  is the particle number density,  $C_{sca}(\theta)$  is the scattering cross section at angle  $\theta$ ,  $E(p)$  is the probe power at position  $p$ , and  $\delta\Omega$  and  $\delta p$  are the solid-angle and volume depth respectively. If the cloud is optically thin,  $E(p) = E_0$ , and the scattered light is not attenuated as it leaves the cloud, so the total scattered light from the entire cloud of thickness  $D$  is

$$\dot{E}(\theta) = \int_0^D \dot{E}(\theta, p) dp = N C_{sca}(\theta) E_0 \delta\Omega D. \quad (A-2)$$

where  $D$  is the thickness of the cloud. If the cloud is not optically thin, then the power at position  $p$  is

$$E(p) = E_0 e^{-NC_{ext} p} \quad (A-3)$$

and the scattered light is attenuated by  $e^{-NC_{ext} L}$ , where  $L$  is the distance out of the cloud at an angle  $\theta$  from position  $p$ . Figure III.A-1 illustrates these relations for a circular cloud with the probe beam passing along the diameter,  $D$ . The total scattered power is

$$\dot{E}(\theta) = \int_0^D \dot{E}(\theta, p) dp = \int_0^D N C_{sca}(\theta) \delta\Omega E_0 e^{-NC_{ext} p} e^{-NC_{ext} L} dp. \quad (A-4)$$

For  $\theta = 20^\circ$ ,  $L$  is equal to  $p$  within 5% so Equation A-4 can be integrated:

$$\begin{aligned}\dot{E}(\theta) &= N C_{\text{sca}}(\theta) \delta\Omega E_0 \int_0^D e^{-2NC_{\text{ext}}p} dp \\ &= N C_{\text{sca}}(\theta) \delta\Omega E_0 D \left( \frac{1 - e^{-2NC_{\text{ext}}D}}{2NC_{\text{ext}}} \right) .\end{aligned}\quad (\text{A-5})$$

From the Beer-Lambert relation:

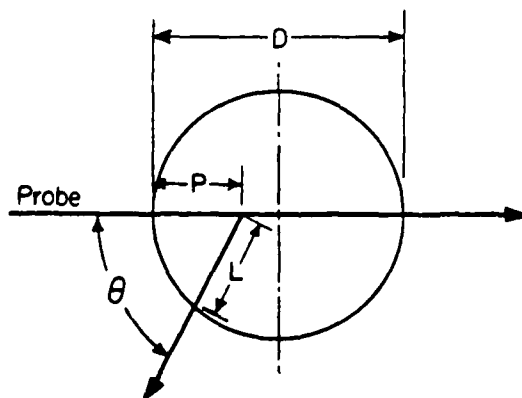
$$\frac{I}{I_0} = e^{-NC_{\text{ext}}D} \quad (\text{A-6})$$

or

$$\ln(I_0/I) = NC_{\text{ext}}D \quad (\text{A-7})$$

Equation A-5 can therefore be rewritten as

$$\dot{E}(\theta) = N C_{\text{sca}}(\theta) \delta\Omega E_0 D \left( \frac{1 - (I/I_0)^2}{2 \ln(I_0/I)} \right) . \quad (\text{A-8})$$



### III.A-1. Scattering diagram with cylindrical symmetry.

For the case where the incident and scattered waves are orthogonal to the scattering plane,  $\frac{\lambda^2}{4\pi^2} i_{\perp}(\theta)$  is substituted for  $C_{sca}(\theta)$ , leading to

$$\frac{2\dot{E}_{\perp}(\theta) \ln(I_0/I)}{E_0 \delta \Omega (1 - (I/I_0)^2)} = \frac{\lambda^2 i_{\perp}(\theta) N D}{4\pi^2} \quad (A-9)$$

Again, the right side is calculable from the Mie equations, the left is measured. Dividing by  $\ln(I_0/I) = NC_{ext} D$  leads to the scatter-extinction ratio corrected for high turbidity,

$$\frac{2 \dot{E}_{\perp}(\theta)(\text{measured})}{E_0 \delta \Omega (1 - (I/I_0)^2)} = \frac{\lambda^2 i_{\perp}(\theta)}{4\pi^2 C_{ext}} \quad (A-10)$$

## CHAPTER IV

### HOMOGENEOUS NUCLEATION AND GROWTH OF SILICON POWDER FROM LASER HEATED $\text{SiH}_4$

by

R. A. Marra, J. H. Flint and J. S. Haggerty

#### ABSTRACT

Nucleation and growth kinetics of Si particles from  $\text{CO}_2$  laser heated  $\text{SiH}_4$  gas have been measured by means of a HeNe laser light scattering and transmission technique. This has permitted the reaction kinetics to be monitored in terms of temperature and reactant partial pressures.

With heating at rates between  $10^5$ - $10^7$ °C/s silicon particles nucleate homogeneously at rates in excess of  $10^{14}$ /cm<sup>3</sup>.s. The rates are in reasonable agreement with Volmer-Weber theory. The rate is controlled by the concentration of silicon atoms in the vapor phase; the high level of supersaturation results in a negligible barrier. Nucleation ceased after the reaction proceeded only a few percent apparently resulting from the rapid decrease in supersaturation and relatively favored heterogeneous growth. Growth rate is controlled by vapor phase transport of reactants to the particle surfaces. The condensation coefficient is estimated to be 0.002-0.02. The growth process is terminated by the depletion of reactants; the final particle size is established by the initial  $\text{SiH}_4$  concentration and the number of nuclei formed.

Separation of the nucleation and growth processes permits final particle dimensions to be controlled through process variables. It also results in uniform particle dimensions needed for ceramic processes based on ordered dispersions.

#### IV.1. INTRODUCTION

Reconsideration of the relationships between the properties of fired ceramic bodies and the characteristics of their constituent powders suggested that uniform diameter powders should be substituted for the traditionally

used powders with broad particle size distributions.<sup>1</sup> Achieving reliable slip stability also requires highly controlled powder purity, stoichiometry, crystallinity, agglomeration, shape and size. Because comminution will not produce submicron powders exhibiting all of these characteristics, they must be synthesized in a manner that achieves these properties simultaneously. In turn, this requires that nucleation, growth, and agglomeration processes be understood and controlled.

Gas phase synthesis generally achieves the required attributes.<sup>2,3</sup> The establishment of high supersaturation levels results in small, equiaxial particles because nucleation rates are high and growth is isotropic.<sup>4</sup> Agglomeration can be controlled with dilution and by minimizing exposure to high temperatures. Overall purities and compositions are controlled through the reactants.

Numerous techniques<sup>5,6</sup> are utilized to synthesize powders from vapor phase reactants. These include tube furnaces, arc and rf plasmas, flash thermolysis, evaporation/condensation in inert atmospheres and shock tubes. While all achieve some of the required process attributes, each but the last fails to achieve them all. Usually, the thermal profiles within reaction zones result in nonuniform nucleation and growth histories, or particles do not cool rapidly enough to avoid formation of hard agglomerates.

The laser-driven gas phase reaction process<sup>2</sup> permits the achievement of all the desired powder characteristics.<sup>3</sup> In this process, an optical energy source, a CO<sub>2</sub> laser, is used to initiate and sustain a vapor phase chemical reaction. The gaseous molecules absorb the laser energy, which is thermalized through molecular collisions. The reaction vessel walls remain cold, avoiding contamination and heterogeneous nucleation sites. The reaction zone is well defined by the intersection of the laser beam and reactant gas stream. A wide range of uniform and precise heating rates with controlled maximum temperatures can be achieved by varying the laser intensity as well as the gas mixture, pressure, and flow rates. The amount of energy supplied to the gas and the resulting heating are defined by the absorptivity of the gaseous products. If the wavelength of the emitted light and the absorption lines of the gaseous molecules are in near coincidence, the optical-to-thermal efficiency is very high. Importantly, the physical geometry of the laser synthesis process enables nucleation and growth

kinetics to be monitored in terms of measured temperatures and calculated reactant partial pressures.

The research described in this paper involves the nucleation and growth mechanisms of silicon powders synthesized from laser-heated silane gas. The pyrolysis of silane to form silicon was modeled first because the reaction path is relatively simple compared to  $\text{Si}_3\text{N}_4$  and  $\text{SiC}$  synthesis processes, and because of the technical importance of high-purity silicon powder for reaction-bonded silicon nitride. The empirical modeling<sup>2,7</sup> of the synthesis process and the effect process variables have on the reaction zone and particle characteristics<sup>3,8,9</sup> were reported in earlier publications. The experimental techniques used to measure particle diameter, number density and temperature were developed by Flint<sup>10</sup> and are reported in detail elsewhere.<sup>11</sup>

#### IV.2. EXPERIMENTAL AND ANALYTICAL PROCEDURES

The powder synthesis cell is shown in Figure IV.1. A cross-flow configuration is used in which a laser beam orthogonally intersects the reactant gas stream. The gas stream is made optically thin so all portions of the gas stream are uniformly exposed. The laser beam enters and leaves the cell through KCl windows. The silane reactant gas, under some conditions diluted with argon, enters the cell through a 1.5 mm ID stainless steel nozzle located 6 mm from the beam center line. The powders produced in the reaction zone are carried to a microfiber filter by the product gases and a surrounding coaxial stream of argon.

Synthesis process variables were manipulated to determine the interactions between the reaction zone and particle characteristics. The synthesis conditions are listed in Table IV.1.

The reaction temperature in the laser powder process is not an extrinsically controllable parameter but is dependent on the process variables. Because the temperature within the reaction zone determines the thermodynamic driving forces, vapor phase reaction kinetics, and particle crystallinity, it is important to measure the temperature distribution within the reaction zone.

A micropyrometer was used to determine the brightness temperature of the hot particles in a small region of the reaction zone. True temperatures were

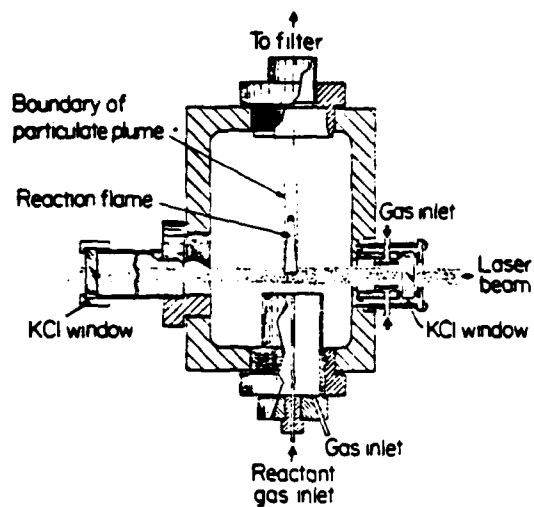


Figure IV.1. Schematic of powder synthesis cell.

TABLE IV.1  
POWDER SYNTHESIS CONDITIONS

Run Number	SiH <sub>4</sub> Flow Rate (cm <sup>3</sup> /min)	Average Velocity (cm/s)	Max. Temp. (°C)
630S	104	490	1130
631S	38	179	1215
634S	6.5	179	1000
645S	13	179	1115
650S	66	104	1338



calculated using the local emissivity of the particulate cloud determined by probing the reaction zone with a HeNe laser and measuring the scattered and transmitted light intensities.<sup>10,11</sup> The ratio of the scattering to extinction cross-sections determined from experimental results and Lorenz-Mie scattering theory permits the emissivity of the particulate cloud to be calculated.

The scatter-extinction method also permits the particle number density and particle diameter to be measured as functions of position in the reaction zone.<sup>10,11</sup> The Mie scattering function and extinction cross-sections are highly dependent on the particles' refractive index.<sup>12</sup> Calculated and measured values of final particle diameters were compared to insure that correct refractive indices were used in calculations.<sup>8,10,11</sup> Local reactant partial pressures were determined by the difference between the initial reactant concentration and the local product concentration calculated from the local particle number density and diameter. Combined with calculated gas velocities, this information permits nucleation and growth kinetics to be determined as functions of temperature and reactant partial pressures.

#### IV.3. RESULTS AND OBSERVATIONS

##### IV.3.A. Temperature Measurements

The general features of the temperature distribution in the reaction zones were similar for all synthesis conditions. Figure IV.2 shows the emissivity, brightness temperature, and true temperature for Run 631S (see Table IV.1 for synthesis conditions). For this and some other run conditions, it is evident that the reaction was well underway before the reactants reached the CO<sub>2</sub> laser beam. Thermal analyses<sup>8,10</sup> showed that at low flow rates, the silane gas is preheated by conduction of heat toward the inlet nozzle. The temperature gradient increases rapidly and reaches a maximum before the gas reaches the beam center. There is no apparent correlation between the particle temperature and the laser intensity distribution, indicating that the silicon particles are not strongly heated by the CO<sub>2</sub> laser beam; this is expected since the absorption efficiency of 50 nm silicon particles to 10.6  $\mu$ m light is quite low.

The time-temperature history conforms to our requirements. Heating rates are high, typically 10<sup>6</sup>-10<sup>8</sup>°C/s. The particles experience no sustained

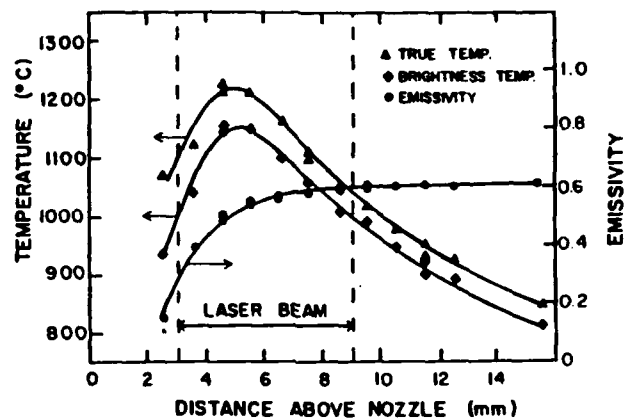


Figure IV.2. True temperature, brightness temperature, and emissivity as a function of distance above the inlet nozzle for Run 631S.

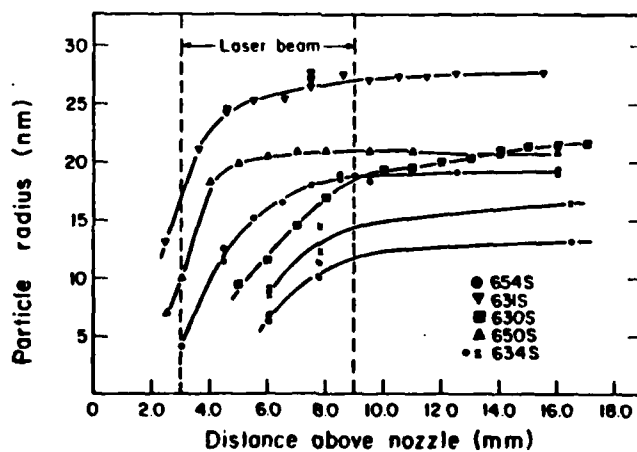


Figure IV.3. Particle size calculated from the scatter-extinction results as a function of distance above the inlet nozzle for various synthesis runs.

exposure to elevated temperatures. The level of the maximum temperature is low compared to many techniques and its value can be controlled over a wide range to an accuracy of  $\pm 20^\circ\text{C}$ . Finally, the cooling rates are rapid enough,  $\sim 10^5^\circ\text{C/s}$ , to retain metastable structures.

#### IV.3.B. In Situ Nucleation and Growth Measurements

Figure IV.3 summarizes the particle size measurements as a function of distance above the inlet gas nozzle. The particles grow at a rapid, nearly constant rate,  $\sim 10^6\text{\AA/s}$ , to their final diameter while still in the laser beam. Under certain conditions, the reaction begins prior to reaching the laser beam. Comparison of the results in Figure IV.3 with corresponding temperature profile measurements shows that the maximum temperature is reached at a point corresponding to the termination of the growth process.

For runs using undiluted silane reactant gas at  $2 \times 10^4\text{Pa}$  (0.2 atm), the closest agreement<sup>10</sup> between the directly measured TEM and BET diameters and the calculated diameters resulted when the particles were assumed to have a refractive index of  $m = 4.38 - 0.26i$  suitable for polycrystalline silicon<sup>13</sup> at around  $1100^\circ\text{C}$  (Runs 630S and 631S). For runs diluted with argon, (Runs 654S and Runs 634S), the best agreement<sup>10</sup> was obtained using a refractive index corresponding to a somewhat lower temperature; both were consistent with the temperature measurements and the crystal structures of the final particles.<sup>6</sup> For the run performed at 0.6 atm (Run 650S), the calculated particle size was smaller than the measured diameter for all reasonable refractive index values. For these process conditions, 90% of the incident HeNe laser light was attenuated in the first millimeter of the particulate plume; thus, the majority of the scattered probe signal originates from the outer edge of the particle cloud. This outermost region is most highly diluted by the surrounding argon gas flow and is subjected to a lower  $\text{CO}_2$  laser intensity than is the reactant gas that passes through the beam center. Therefore, it is likely that the gas stream temperature in this outer zone and resulting particle diameter will be significantly smaller than the average values.

Particle number density calculations employ the HeNe path length and the results of the scatter-extinction measurements. Because it is difficult to measure the path length  $l$  through the reaction zone accurately, the product of the number density and the path length was calculated and is reported. For most synthesis conditions, the path length was relatively constant and

approximately equal to 1 cm, so the number density is well represented by this product.

Figure IV.4 shows the calculated number-density·path-length product,  $Nl$ , as a function of position above the gas inlet nozzle for the same conditions as in Figure IV.3.<sup>10</sup>

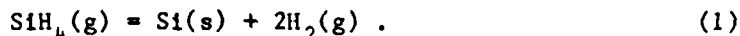
The calculated  $Nl$  values decrease from maximum values at the initiation of the reaction zone until they reach constant values further into the particulate cloud. The volumetric expansion of the heated gas has only a very small effect on the  $Nl$  product. The decrease in  $Nl$  might indicate that particles coagulate as they penetrate the reaction zone; however, an abrupt termination of the agglomeration process is unlikely. Alternatively, the number density remains essentially constant if the particles are assumed to have a refractive index appropriate for amorphous silicon when they form and then change to a polycrystalline index with further penetration into the reaction zone. This behavior indicates that particles form as amorphous silicon and then crystallize in the deeper regions of the reaction zone; this is consistent with the final particle microstructure and possible particle formation mechanisms.<sup>14</sup>

The constant number density indicates that for these synthesis conditions the particles do not agglomerate within the observed region of reaction zone. These results also indicate that nucleation occurred only at the very base of the reaction zone, ceasing before significant particle growth occurred. Both results are critical for producing powders with the desired characteristics.

#### IV.4. PARTICLE NUCLEATION AND GROWTH MECHANISMS

##### IV.4.A. Nucleation

The exact reaction path and rate-controlling step for silane decomposition are not known with certainty; both simple decomposition<sup>15</sup> and polymerization mechanisms<sup>16</sup> have been proposed. Several investigations<sup>17,18,19</sup> of CO<sub>2</sub> laser-induced silane pyrolysis have shown the absence of higher silanes in the reaction products, suggesting that the laser induced pyrolysis occurs by the simple decomposition reaction;



We have developed our analyses on this basis. Because this reaction has a negative free energy and is exothermic,<sup>20</sup> it is apparent that kinetic rather than thermodynamic factors would dominate nucleation and growth processes.

For nucleation to occur, the vapor phase must be sufficiently supersaturated to overcome the free energy barrier created by the new surface of a nucleus. The nucleation rate depends on the number of silicon atoms in the vapor phase, since nucleation occurs by an accretion process limited by the rate at which monomeric silicon collides with other monomers or existing clusters to create nuclei of supercritical size. Thus, the description of the nucleation process requires the determination of the molecular silicon vapor concentration, the supersaturation ratio, and the nucleation rate from the existing theories.

The supersaturation ratio, SS, is defined by the quotient of the actual partial pressure of Si(g) in the reactant gas stream and by the equilibrium vapor pressure of Si°(g)

$$SS = \frac{P_{\text{Si}(\text{g})}}{P_{\text{Si}^\circ(\text{g})}} . \quad (2)$$

Assuming that SiH<sub>4</sub>(g), Si(g) and H<sub>2</sub>(g) are the predominant vapor species, the equilibrium concentration of Si(g) in the reactant gas stream is given by the reaction:



with an equilibrium constant

$$k_1 = \frac{P_{\text{Si}(\text{g})} P_{\text{H}_2}^2}{P_{\text{SiH}_4}} . \quad (4)$$

The equilibrium vapor pressure  $P_{\text{Si}^\circ}$ , is determined by the reaction:



with an equilibrium constant:

$$k_2 = P_{\text{Si}^\circ} . \quad (6)$$

With known equilibrium constants,  $P_{\text{Si}(\text{g})}$  and  $P_{\text{Si}^\circ(\text{g})}$  can be determined.

Figure IV.5 shows the effects of temperature and the extent of gas phase decomposition on the supersaturation ratio for a reaction zone initially comprised of pure silane at  $2 \times 10^4 \text{ Pa}$  (0.2 atm). For all temperatures the

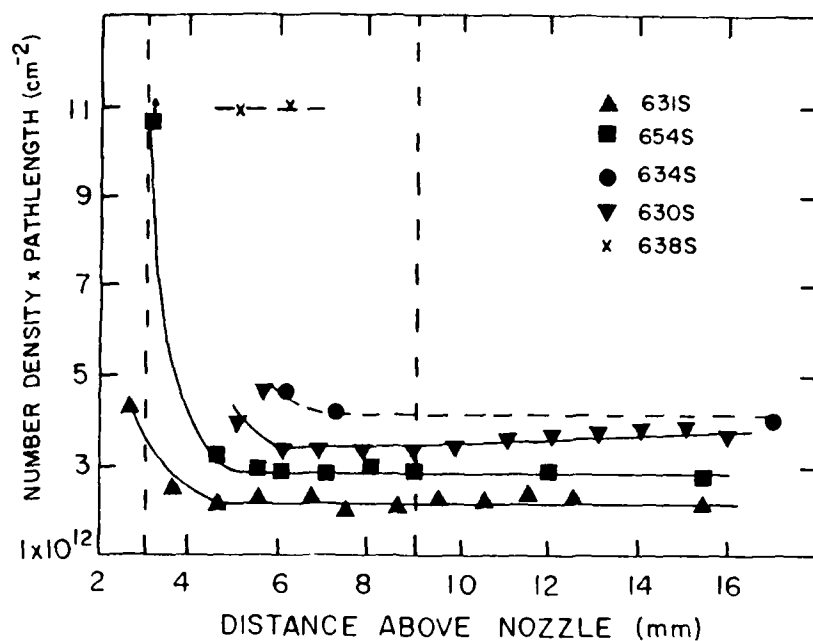


Figure IV.4. Product of the particle number density and optical pathlength as a function of distance above the inlet nozzle.

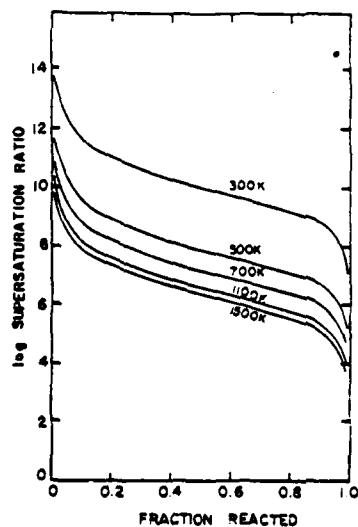


Figure IV.5. The effect of temperature and percent reaction on the supersaturation ratio for silane pyrolysis.

supersaturation ratio decreases sharply from infinity as the reaction begins to proceed.

Both the nucleation rate,  $J$ , and the critical radius size,  $r^*$ , in a supersaturated vapor can be approximated by the application of homogeneous nucleation theory. The critical size nucleus is related to the supersaturation ratio by the Gibbs-Kelvin equation:<sup>21</sup>

$$r^* = \frac{2\sigma v_{Si}}{kT \ln SS} \quad (7)$$

where  $\sigma$  is the interfacial energy between the solid and vapor and  $v_{Si}$  is the molecular volume of silicon. The free energy of formation of the critical size nucleus is given by:

$$\Delta F^* = - \frac{16 \pi \sigma^3 v_{Si}^2}{3 (kT \ln SS)^2} \quad (8)$$

Using Volmer-Weber theory,<sup>22</sup> the equation describing the homogeneous nucleation rate is:

$$J = \alpha \frac{P_{Si}}{(2\pi mkT)^{1/2}} 4\pi r^{*2} \frac{P_{Si}}{kT} \exp\left[\frac{-\Delta F^*}{kT}\right] \quad (9)$$

where  $\alpha$  is the condensation coefficient and  $m$  is the mass of a silicon atom. The nucleation rate is dependent on both the thermodynamic driving force for the phase transformation and kinetic factors related to the collisions of vapor phase silicon atoms with critical size silicon nuclei.

Table IV.2 summarizes nucleation rate calculations for a reactant gas stream initially composed of pure silane gas at  $2 \times 10^4$  Pa (0.2 atm). The critical size nucleus contains only a few silicon atoms as a consequence of the extremely large supersaturation, for example,  $SS = 7.8 \times 10^4$  at 300K. Consequently, there is essentially no thermodynamic barrier for nucleation. Rather, the nucleation rate is primarily controlled by the collision rate between silicon atoms and subcritical nuclei; at low temperatures the rate is low because the equilibrium concentration of silicon vapor is extremely small.

The actual nucleation rates can be estimated from the scatter-extinction measurement. The calculated particle number densities ranged from  $1.1 \times 10^{11}$  to  $2.2 \times 10^{12}$  nuclei/cm<sup>3</sup>. The reactant gas traveled from the inlet nozzle to the position where the particles were first observed in less than  $10^{-2}$ s with

TABLE IV.2

NUCLEATION CALCULATIONS FOR A REACTION ZONE INITIALLY  
COMPRISED OF 0.2 ATM. OF PURE SILANE

Temp (°K)	P <sub>Si</sub> (atm)	P <sub>Si</sub> <sup>0</sup> (atm)	ln SS	r <sup>*</sup> (nm)	ΔG <sub>r</sub> <sup>*</sup> (J)	J (#/cm <sup>3</sup> ·s)
300	1.65x10 <sup>-21</sup>	2.12x10 <sup>-71</sup>	114.9	0.075	2.15x10 <sup>-20</sup>	7.4x10 <sup>-17</sup>
400	2.02x10 <sup>-15</sup>	8.77x10 <sup>-55</sup>	90.6	0.072	1.94x10 <sup>-20</sup>	3.5x10 <sup>-4</sup>
500	9.64x10 <sup>-12</sup>	5.16x10 <sup>-40</sup>	65.1	0.080	2.40x10 <sup>-20</sup>	7.4x10 <sup>3</sup>
600	2.82x10 <sup>-9</sup>	3.59x10 <sup>-32</sup>	52.7	0.082	2.55x10 <sup>-20</sup>	7.6x10 <sup>8</sup>
700	1.64x10 <sup>-7</sup>	1.43x10 <sup>-26</sup>	43.9	0.085	2.70x10 <sup>-20</sup>	2.4x10 <sup>12</sup>
800	3.50x10 <sup>-6</sup>	2.24x10 <sup>-22</sup>	37.3	0.087	2.70x10 <sup>-20</sup>	1.4x10 <sup>15</sup>
900	3.78x10 <sup>-5</sup>	4.06x10 <sup>-19</sup>	32.2	0.090	3.03x10 <sup>-20</sup>	1.7x10 <sup>17</sup>
1000	2.53x10 <sup>-4</sup>	1.63x10 <sup>-16</sup>	28.1	0.093	3.23x10 <sup>-20</sup>	7.5x10 <sup>18</sup>
1100	1.25x10 <sup>-3</sup>	2.20x10 <sup>-14</sup>	24.8	0.095	3.43x10 <sup>-20</sup>	1.8x10 <sup>20</sup>
1200	4.29x10 <sup>-3</sup>	1.30x10 <sup>-12</sup>	21.9	0.099	3.70x10 <sup>-20</sup>	2.1x10 <sup>21</sup>
1300	1.22x10 <sup>-2</sup>	4.09x10 <sup>-11</sup>	19.5	0.103	3.97x10 <sup>-20</sup>	1.6x10 <sup>22</sup>
1400	2.78x10 <sup>-2</sup>	7.81x10 <sup>-10</sup>	17.4	0.107	4.30x10 <sup>-20</sup>	8.3x10 <sup>22</sup>
1500	4.85x10 <sup>-2</sup>	1.00x10 <sup>-8</sup>	15.4	0.113	4.78x10 <sup>-20</sup>	2.3x10 <sup>23</sup>
1600	6.21x10 <sup>-2</sup>	9.35x10 <sup>-8</sup>	13.4	0.121	5.55x10 <sup>-20</sup>	3.2x10 <sup>23</sup>



all flow conditions; a time that may be significantly longer than the period in which nucleation actually occurs. Therefore, the actual Si nucleation rates are in excess of  $10^{14}$  nuclei/cm<sup>3</sup>.s.

It was not possible to observe the actual nucleation events with the scatter-extinction technique<sup>10</sup> since the minimum detectable particle diameter is approximately 8 nm with a HeNe light source. Also, the temperature at which nucleation begins could not be measured by optical pyrometry as a consequence of the low radiance of small particles (~ 1.0 nm) having true temperatures below 900°C. The lowest temperature at which particles were first observed ranged from approximately 900°C to 1100°C. It is believed that the nucleation actually occurred at temperatures significantly below these measured temperatures: probably between 600 and 900°C.

The nucleation rates calculated with the Volmer-Weber theory, Table IV.2, can be compared to the nucleation rate estimated from the scatter-extinction results. For pure SiH<sub>4</sub> at 0.2 atm, the calculated nucleation rate varies from  $1.7 \times 10^{17}$  nuclei/cm<sup>3</sup>.s at 900K to  $2.1 \times 10^{21}$  nuclei/cm<sup>3</sup>.s at 1200K. These values are approximately 3 to 7 orders of magnitude higher than the minimum nucleation rate value estimated by scatter-extinction measurements.

There are many possible reasons for the discrepancy between the measured and calculated nucleation rates. It was assumed that the condensation coefficient,  $\alpha$ , was equal to 1.0 for the calculation of the nucleation rate using the Volmer-Weber theory. However, the condensation coefficient is always less than unity for bulk samples and is expected to be even lower for nucleus-size clusters because they are unable to absorb the heat of condensation to the extent that the large clusters can.<sup>23</sup>

It was assumed that SiH<sub>4</sub>(g) and Si(g) were the primary silicon-containing vapor species within the reaction zone. If other vapor species (SiH<sub>2</sub>, SiH<sub>3</sub>, etc) are present, then the actual concentration of Si(g) will be less than that was calculated presuming the existence of only SiH<sub>4</sub>(g) and Si(g). This correction would be quite large, because the calculated nucleation rate is dependent on the square of the Si(g) monomer concentration.

It is probable that the time interval during which nucleation actually occurs is much shorter than the value estimated from the gas velocity and the onset of observed nucleation. Also, the nucleation temperature may be lower

than that used in the calculations. Several plausible combinations of nucleation time and temperature, ranging from  $10^{-7}$ s at 1000K to  $10^{-2}$ s at 800K, yield calculated nucleation rates that agree with experimental observations.

One of the major uncertainties of the classical homogeneous nucleation theory lies in the assumption that clusters containing only a few atoms can be described in terms of bulk material properties. For single-component systems, several workers have proposed that the interfacial energy increases as the cluster radius decreases.<sup>24,25</sup> If the nucleating temperature is assumed to be 1000K, an increase in the interfacial energy from  $0.9 \text{ J/m}^2$  to  $1.5 \text{ J/m}^2$  would result in approximately a  $10^4$  decrease in the calculated nucleation rate, bringing the calculated value into good agreement with the measured nucleation rate.

Finally, there are both corrections and alternatives to the classical Volmer-Weber theory.<sup>26</sup> The actual steady-state nucleation rate is always lower than the equilibrium rate predicted by the Volmer-Weber treatment. The corrected steady-state solution<sup>27</sup> generally introduces a nonequilibrium or Zeldovich factor into Equation 9. For pure silicon at 0.2 atm and nucleation temperatures of 900K and 1200K, the Zeldovich factor is calculated to be 0.51 and 0.49 respectively. Therefore, this correction is only partially responsible for the discrepancy between the measured and calculated nucleation rates. The Lothe-Pound relation<sup>28</sup> which considers the statistical mechanical contributions to the free energy of formation of the critical nuclei is an important alternative to the classical nucleation theory. At  $T = 1000\text{K}$ , for a spherical cluster containing 2 to 3 silicon atoms, the Lothe-Pound correction factor is approximately  $10^{20}$ . Thus the Lothe-Pound theory is not applicable because it predicts an even larger nucleation rate.

In light of these uncertainties, it is of little value to pursue the differences between measured and calculated nucleation rates. The most fundamental problem is one of utilizing bulk material properties to describe clusters containing only a few individual atoms. We accept the Volmer-Weber model as an adequate semiquantitative description of the nucleation process.

The number densities calculated from the scatter-extinction measurements indicate that nucleation ceases before the reaction proceeds to an appreciable extent. Murthy et al.<sup>29</sup> observed similar behavior for the thermal decomposition of silane in a resistance heated reaction tube furnace.

They found that particles formed at the beginning of the hot zone of the reactor (approximately 700°C) and that very little further nucleation occurred after the particles achieved macroscopic size.

The rapid cessation of nucleation is probably a consequence of two factors. As solid silicon is produced, the silicon monomer concentration within the reaction zone is reduced; this is evident from Figure IV.5 which shows that the supersaturation ratio decreases sharply as the silane decomposition reaction proceeds. Nucleation effectively ceases when the silicon monomer concentration drops below a critical level. Also, once nuclei are formed, they act as heterogeneous sites, and growth by simple condensation is favored over further nucleation.<sup>8</sup>

#### IV.4.B. Growth

The light scattering results show that once nucleation ceases, the particles grow to their final dimensions via the accretion of vapor phase molecules; growth by coagulation was not evident under the reaction conditions studied. The final particle size is limited by the depletion of the available silane, and not by the elapsed growth time at elevated temperatures. Thus, the final size is dependent on the number of nuclei formed and the concentration of silicon atoms available to the growing nuclei rather than growth rate. However, analysis of the growth process is important in understanding the particle formation mechanisms.

The growth process involves transport of a vapor species to the surface of the silicon nucleus and condensation or deposition steps at the surface. A typical vapor phase growth process involves the following steps.

1. Transport of the reactive species to the particle surface.
2. Adsorption of the reactants on the particle surface.
3. Formation of the solid product either by simple condensation or a chemical reaction.
4. Desorption of any gaseous reaction products.
5. Transport of the gaseous reaction products away from the particle surface.

The overall growth rate will be determined by the slowest step. Steps 1 and 5 involve the transport of material in the vapor, generally by gaseous diffusion. Steps 2, 3 and 4 occur at or on the particle surface; growth limited by one of these steps is termed chemical or surface controlled.

The rate laws for growth limited by vapor transport have been derived by various investigators.<sup>30</sup> Ignoring the effects on the growth rate of a plurality of particles and the moving boundary, the volumetric growth law for particles much larger than the mean free path in the vapor phase is

$$\frac{dV}{dt} = \frac{4\pi D r_p v_{Si} (P_{Si(g)} - P_{Si^{\circ}(g)})}{kT}, \quad (10)$$

and for particles smaller than the mean free path is

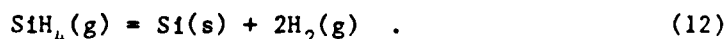
$$\frac{dV}{dt} = \frac{4\alpha\pi r_p^2 v_{Si} (P_{Si(g)} - P_{Si^{\circ}(g)})}{(2\pi mkT)^{1/2}}. \quad (11)$$

where  $D$  is the gaseous diffusion coefficient,  $r_p$  is the particle radius,  $v_{Si}$  is the molecular volume,  $P_{Si(g)}$  is silicon partial pressure in the reactant gas stream,  $P_{Si^{\circ}(g)}$  is the equilibrium silicon partial pressure, and  $m$  is molecular mass. For all the reaction conditions studied, the mean free path within the reaction zone was greater than  $1 \mu m$ . Because this is significantly larger than the particle size, it is anticipated that the particle growth rate will be represented by Equation 11 if the growth rate is limited by vapor transport. Consequently, the radial growth rate  $dr/dt = (1/4\pi r_p^2) dV/dt$  will be independent of the particle radius and directly proportional to the concentration of  $Si(g)$  since the vapor pressure over solid silicon,  $P_{Si^{\circ}(g)}$  is much smaller than the equilibrium pressure of  $Si(g)$  within the vapor phase. However, if vapor transport processes are rapid, particle growth rates will be controlled by processes occurring at the particle surfaces.

Seto<sup>31</sup> studied the growth rate of polycrystalline silicon from the pyrolysis of silane at temperatures where the growth kinetics are rate limited at the surface. A reaction mechanism involving the chemisorption of silane onto the silicon surface, the decomposition of silane into silicon and hydrogen, and the desorption of hydrogen explained the experimental results satisfactorily. He found that the desorption step could be assumed to be fast in comparison with adsorption and decomposition steps because the hydrogen gas produced by the decomposition reaction did not effect the decomposition rate.

Seto found that the reaction rate is determined by the relative values of the Langmuir adsorption coefficient  $\beta_{SiH_4}$  and the reaction rate constant

$k_R$  where  $\beta_{\text{SiH}_4} = k_{\text{SiH}_4} / k_{-\text{SiH}_4}$ , with  $k_{\text{SiH}_4}$  representing the silane absorption rate constant and  $k_{-\text{SiH}_4}$  being the desorption rate constant, and  $k_R$  being the rate constant for the silane decomposition reaction:



The overall growth rate<sup>31</sup> is represented by:

$$\frac{dV}{dt} = \frac{v_{\text{Si}} k_R \beta_{\text{SiH}_4} [\text{SiH}_4]}{1 + \beta_{\text{SiH}_4} [\text{SiH}_4]} \quad (13)$$

where  $[\text{SiH}_4]$  is the molar concentration of  $\text{SiH}_4$  in the gas stream. For silane concentrations ranging from  $5 \times 10^{-7}$  mole/cm<sup>3</sup> to  $4 \times 10^{-8}$  mole/cm<sup>3</sup> and temperatures from 650 to 800°C, Seto found that the following expressions fit experimental observations.

$$\beta_{\text{SiH}_4} = 2.0 \times 10^{13} \exp - \frac{15200}{T} \quad (14)$$

and

$$k_R = 9.4 \times 10^{-4} \exp - \frac{5900}{T} \quad (15)$$

Equations 10, 11 and 13 predict specific functional dependencies between growth rate and variables such as temperature, particle size, and reactant concentration. Our synthesis experiments permitted the identification of the rate-controlling step. Particle diameter, number density, and temperature were measured directly by the scatter-extinction technique. Radial growth rates were determined from data like that shown in Figure IV.3. The concentration of silicon remaining in the vapor phase was calculated throughout the reaction zone by subtracting the local amount of silicon existing in solid particles from the inlet concentration.

Figure IV.6 shows the calculated concentration of silicon in the vapor phase as a function of position in the reaction zone for Run 654S, in which a 2:1 Ar: $\text{SiH}_4$  gas mixture was used. It is evident that the reaction occurred in a continuous manner and was essentially complete while the particles and gases were still in the laser beam. The concentration profiles for the other runs were similar to that shown in Figure IV.6.

Figure IV.7 plots the natural logarithm of the growth rate versus the natural logarithm of the concentration of silicon within the reaction zone for Runs 630S and 654S. The growth rates were determined from the slopes of the curves in Figure IV.3 assuming that the velocity remains constant in the

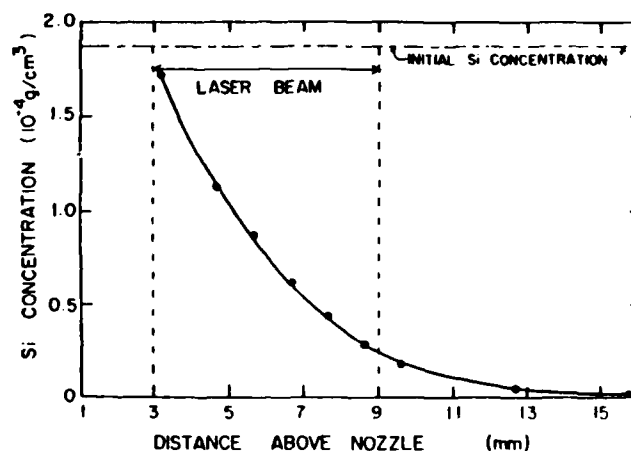


Figure IV.6. Calculated silicon concentration in the reaction zone as a function of distance above the inlet nozzle for Run 654S.

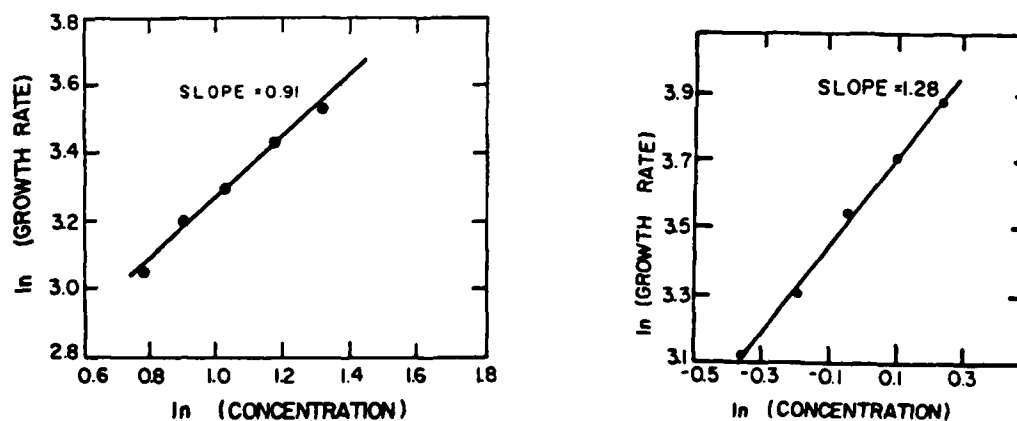


Figure IV.7. The logarithm of the growth rate calculated from the scattering-extinction results versus the logarithm of the silicon concentration in the reaction zone. (a. Run 630S. b. Run 654S.)

spatial intervals examined. This assumption introduces little error since these intervals are small. For both runs, the reaction temperature is relatively constant in the regions plotted. Therefore, the change in the growth rate is expected to be directly related to the change in the vapor concentration. The slopes of these curves are in reasonable agreement with the value (1.0) predicted by Equation 11 for transport rate-controlled growth.

This conclusion agrees with findings of others. At temperatures above 900°C, Bloem<sup>32</sup> determined that growth rate was dependent on vapor transport for chemical vapor deposition of silicon from silane; at lower temperatures, the surface reaction kinetics determined the overall growth behavior. Everstyn et al.<sup>33</sup> also found the deposition from silane at 1050°C to be a transport limited process.

It is possible to estimate the condensation coefficient by comparing the growth rate measured from light scattering with that predicted by Equation 11. Table IV.3 shows the growth rate calculated using Equation 11 for Runs 630S and 654S (see Table IV.1 for reaction conditions). The partial pressure of  $\text{SiH}_4(\text{g})$  and  $\text{Si}(\text{g})$  was determined from the amount of silicon in the vapor phase (estimated from Figure IV.6 and a similar curve for Run 630S) and equilibrium thermodynamics. The silicon particles can grow by two mechanisms: through gas phase decomposition of the silane according to Equation 1 and condensation of the  $\text{Si}(\text{g})$  molecules onto the growing particle or by the adsorption of  $\text{SiH}_4(\text{g})$  molecules and the decomposition of adsorbed  $\text{SiH}_4$  to form  $\text{Si}(\text{g})$  and  $\text{H}_2(\text{g})$  which must be desorbed from the particle surface. Therefore, the growth was calculated by assuming: (1) only the adsorption of silicon vapor leads to particle growth and (2) both silicon and silane vapor molecules are adsorbed during growth. In both cases a condensation coefficient of unity was assumed.

It is evident that the experimentally observed growth rate is 2 to 3 orders of magnitude lower than the calculated growth rate. The effects of a plurality of particles and of the moving growth surface result in negligible corrections to the calculated growth rate.<sup>8</sup> Therefore, it is assumed the growth is limited by the bombardment of vapor molecules, which have a condensation coefficient significantly less than unity; the condensation coefficient required to bring the experimental and calculated results into agreement is shown in Table IV.3. If it is assumed that both  $\text{SiH}_4(\text{g})$  and

**TABLE IV.3**  
**COMPARISON OF EXPERIMENTAL GROWTH RATE**  
**AND CALCULATED GROWTH RATE (TRANSPORT LIMITED)**

Distance From Nozzle (mm)	$P_{SiH_4}$	$P_{Si}$	Growth Rate (nm/sec)			$\alpha$	$\alpha$
	(Nt/m <sup>2</sup> )		Measured	Calc.A	Calc.B	Si	Si+SiH <sub>4</sub>
Run 654S							
3.5	4.1x10 <sup>3</sup>	6.7x10 <sup>2</sup>	4.5x10 <sup>3</sup>	1.9x10 <sup>5</sup>	1.1x10 <sup>6</sup>	0.02	0.004
4.5	1.2x10 <sup>3</sup>	9.1x10 <sup>2</sup>	2.4x10 <sup>3</sup>	2.4x10 <sup>5</sup>	5.7x10 <sup>5</sup>	0.01	0.004
5.5	6.1x10 <sup>2</sup>	8.0x10 <sup>2</sup>	1.6x10 <sup>3</sup>	2.2x10 <sup>5</sup>	3.8x10 <sup>5</sup>	0.008	0.004
6.5	4.9x10 <sup>2</sup>	4.8x10 <sup>2</sup>	7.0x10 <sup>2</sup>	2.5x10 <sup>5</sup>	2.6x10 <sup>5</sup>	0.005	0.003
7.5	7.0x10 <sup>2</sup>	2.6x10 <sup>2</sup>	4.8x10 <sup>2</sup>	7.4x10 <sup>4</sup>	2.7x10 <sup>5</sup>	0.007	0.002
8.5	4.6x10 <sup>2</sup>	1.0x10 <sup>2</sup>	2.0x10 <sup>2</sup>	2.9x10 <sup>4</sup>	1.4x10 <sup>5</sup>	0.007	0.002
Run 630S							
5.5	1.1x10 <sup>4</sup>	2.2x10 <sup>3</sup>	1.2x10 <sup>4</sup>	6.1x10 <sup>5</sup>	3.8x10 <sup>6</sup>	0.02	0.003
6.5	7.4x10 <sup>3</sup>	2.2x10 <sup>3</sup>	8.2x10 <sup>3</sup>	6.1x10 <sup>5</sup>	2.6x10 <sup>6</sup>	0.01	0.003
7.5	5.2x10 <sup>3</sup>	2.1x10 <sup>3</sup>	4.2x10 <sup>3</sup>	5.7x10 <sup>5</sup>	1.9x10 <sup>6</sup>	0.008	0.002
8.5	4.7x10 <sup>3</sup>	1.2x10 <sup>3</sup>	3.6x10 <sup>3</sup>	3.4x10 <sup>5</sup>	1.7x10 <sup>6</sup>	0.01	0.002

A calculates growth assuming only Si(g) atoms are absorbed.  
B calculates growth assuming Si(g) and SiH<sub>4</sub> atoms are absorbed.



Si(g) species are adsorbed on the particle surface, the condensation coefficient is essentially constant, ranging from 0.002 to 0.004. For silicon adsorption, the calculated condensation coefficient is larger and exhibits a larger range. The possible existence of the vapor species  $\text{SiH}_2$  and  $\text{SiH}_3$  has been ignored. If they are present in the vapor phase and also contribute to the particle growth, the theoretical growth rate will be approximately equal to that calculated above for  $\text{SiH}_4(\text{g})$  and  $\text{Si}(\text{g})$  adsorption since the total concentration of silicon containing species in the vapor phase will be equivalent.

#### IV.4.C. Control of Particle Size, Shape and Size Distribution

This powder synthesis process was investigated with the goal of achieving control of particle size, shape, and size distribution. It is essential that resulting powders be uniform in size, equiaxial and small in diameter.

Since the particle growth is limited by vapor transport and not a surface reaction, a thermodynamic equilibrium can be assumed to exist at the particle surface. Therefore, the growth rate will not be dependent on the crystallographic nature of the surfaces and particles will tend to grow isotropically, resulting in equiaxed shapes.<sup>34</sup> All powders examined by electron microscopy were found to be spherical in shape.

The early cessation of homogeneous nucleation during the reaction results in a large number of independent nuclei that grow to their final dimensions by the depletion of the available silane gas. The general separation of nucleation and growth processes tends to produce uniform size particles. However, there is a short period of time during which nucleation and growth probably occur simultaneously, which results in an initial distribution of particle sizes. It can be ascertained whether the difference in the particle sizes becomes accentuated or whether the system tends toward monodispersivity with further growth.

If all the nuclei are exposed to the same temperature and concentration profiles, the differences in the particle growth should result only from the initial differences in particle size when nucleation ceased. When growth is limited by vapor transport, Firsch and Collins<sup>35</sup> showed that the growth rates of particles with different radii are related by the expression

$$\frac{dr/dt}{dr'/dt} = \frac{\gamma + r'}{\gamma + r} \quad (16)$$

where  $r$  and  $r'$  are the radii of particles that had radii equal to  $r_0$  and  $r'_0$  at the time when nucleation ceased, and  $\gamma = \rho/\alpha$  where  $\rho$  is on the order of the mean free path and  $\alpha$  is the probability that impinging molecules will be adsorbed. If  $\gamma \gg r$ , the particles will grow at equal rates. Even if  $\gamma > r$  throughout the entire growth period, the initial differences in the particle sizes will become insignificant as the particles approach their final sizes, because the nucleation process terminated early in the growth process. If with continued growth  $r > \gamma$ , the relative growth rate will become inversely proportional to the ratio of the radii tending to suppress the initial differences in the relative particle radii. Therefore, it may be concluded that a synthesis process characterized by early cessation of homogeneous nucleation and transport limited growth will result in a particle size distribution that tends towards monodispersity. For all synthesis conditions, the final particle size distribution was always somewhat polydispersed. This result is probably a consequence of temperature and compositional gradients within the reaction zone.

The large thermodynamic driving force for the production of solid silicon from silane gas leads to the complete utilization of the silane. Final particle size is determined by the amount of silane available for each growing nuclei. Assuming 100% conversion, a material balance gives the following relation for the final particle size:

$$d = \left( \frac{6}{\pi} \frac{C_0 M^{1/3}}{N \rho} \right) \quad (16)$$

where  $d$  is the average diameter of the particles formed,  $C_0$  is the initial concentration of silane in the reaction zone,  $N$  is the number of nuclei formed per unit volume of reacting gas,  $M$  is the molecular weight of silicon, and  $\rho$  is the density of the product. The particle size can be controlled by manipulating the concentration of the reactant gas and the number of nuclei produced.

#### IV.5. CONCLUSIONS

It was found that the laser synthesis process produces powder with nearly ideal characteristics. The particle characteristics can be systematically and reproducibly varied by the manipulation of the laser intensity, reaction pressure, dilution of the reactant gas, and reactant gas flow rates. The conversion efficiency to solid particles is nearly 100%.

The silane decomposition reaction is thermal in nature with the temperature of the reactant gas determined by the laser intensity, the effective absorption coefficient at the particular emission line, the heat capacity of the reactant gas mixture, and the residence time in the laser beam.

Gas phase nucleation is initiated at the beginning of the reaction zone and ceases just after the reaction is initiated. The cessation is a result of the depletion of silicon vapor reducing the supersaturation as well as the kinetic favoring of particle growth by the accretion of vapor molecules over further nucleation. The observed nucleation rate,  $>10^{14}$  nuclei/cm<sup>3</sup>.sec, is in reasonable agreement with the calculated rate using Volmer-Weber theory.

The growth was determined to be rate limited by the transport of vapor species to the particle surface. The experimentally observed growth rate is 2 to 3 orders of magnitude lower than the growth rate calculated from the vapor transport model assuming a condensation coefficient of unity. A condensation coefficient of 0.002 to 0.02 brings the theoretical growth rate into agreement with the observed growth rate. The nature of the growth process results in spherical particles with narrow distribution of particle sizes.

Under the synthesis conditions investigated, particle agglomeration did not occur within the reaction zone. Chainlike agglomerates formed as the particles travelled to the collection filter or as they were collected.

#### IV.6. ACKNOWLEDGEMENTS

This research was funded in part by ARPA under contract number N00014-77-C-0581, by NASA-Lewis under contract number NSG-7645, and by ONR/ARO under contract number N00014-82-K-0350.

#### IV.7. REFERENCES

1. H. K. Bowen et al., "Basic Research Need on High Temperature Ceramics for Energy Applications," *Mat. Sci. and Eng.* 4, 41-56 (1980).
2. W. R. Cannon, et al., "Sinterable Ceramic Powders from Laser Driven Reactions, Part I: Process Description and Modelling," *J. Am. Ceram. Soc.*, 65, 324-30 (1982).
3. W. R. Cannon, et al., "Sinterable Ceramic Powders from Laser Driven Reactions, Part II: Powder Characteristics and Process Variables", *J. Am. Ceram. Soc.*, 65, 331-35 (1982).
4. A. Kato, et al., "Formation of Ultrafine Powder of Refractory Nitrides and Carbides by Vapor Phase Reaction," *Memoirs of the Faculty of Eng., Kyushu Univ.*, 41, 319-34 (1981).
5. D. W. Johnson, Jr., "Non-Conventional Powder Preparation Techniques" *Bull. Am. Ceram. Soc.*, 60, 221 (1981).
6. J. S. Haggerty, Sinterable Powders from Laser Driven Reactions, Under Contract N00014-77-C0581, Final Report, M.I.T., Cambridge, MA, 1981.
7. R. A. Marra and J. S. Haggerty, "Synthesis and Characteristics of Ceramic Powders made from Laser Heated Gases", *Ceramic Engineering and Science Proceedings*, 3, 1-2, 3-19 (1982).
8. R. A. Marra, "Homogenous Nucleation and Growth of Silicon Powder from Laser Heated Gas Phase Reactants," PhD Thesis, Department of Materials Science and Engineering, MIT, Cambridge, MA, January 1983.
9. Y. Suyama, et al., "Synthesis of Ultrafine SiC Powders by Laser Driven Gas Phase Reactions" submitted to *J. Am. Ceram. Soc.*
10. J. H. Flint, "Powder Temperatures in Laser Driven Reactions," M.S. Thesis, MIT, Cambridge, MA 1982.
11. J. H. Flint, R. A. Marra and J. S. Haggerty, "Powder Temperature, Size, and Number Density in Laser Driven Reactions" To be submitted for publication.
12. M. Kerker, The Scattering of Light and Other Electromagnetic Radiation, Academic Press, 1969.
13. M. Janai and B. Karlson, "Temperature Variation of the Absorption Edge of CVD Amorphous and Polycrystalline Silicon," *Solar Energy Materials*, 1, 387-95 (1979).
14. R. A. Marra and J. S. Haggerty, "Microstructure and Formation Mechanism of Si Powders Produced from Laser Driven Reactions", to be published.
15. G. G. Deryatyk, et al. "Kinetics of the Thermal Decomposition of Monosilane, Arsine, and Monosilane with Arsine Impurity," *Russ., J. Inorg. Chem.*, 18, 1528 (1965).

16. J. H. Purnell and R. Walsh, "Pyrolysis of Monosilane," Proc. Royal Soc., Series A, London, p. 545 (1966).
17. T. F. Deutsch, "Infrared Laser Photochemistry of Silane," J. Chem. Phys., 70, 1187 (1979).
18. A. N. Oraevskii, et al., "Laser-Chemical Decomposition of Monosilane," High Energy Chem., 12, 48 (1978).
19. R. Bilenchi and M. Musci, "Laser Enhanced Chemical Vapor Deposition of Silicon," in Proc. 8th Int. Conf. on Chemical Vapor Deposition, Eds. J. M. Blocher and G. E. Vulillard, The Electrochemical Soc., Pennington, N.J., 1981 p. 275-85.
20. JANAF, Thermodynamic Tables, NSRDS-NBS, 37, 1971.
21. R. A. Swalin, Thermodynamics of Solids, John Wiley & Sons, New York, 1972, p. 182.
22. M. Volmer and A. Weber, "Keimbildung in ubersattigten Gebilden," Z. Phys. Chem., 119, 277 (1926).
23. J. Hirth and G. M. Pound, "Condensation and Evaporation: Nucleation and Growth Kinetics" in Progress in Materials Science, Vol. 11, MacMillan Co., New York, 1963, p.5.
24. F. F. Abraham, Homogeneous Nucleation Theory, Academic Press, New York, 1974, pp. 184-91.
25. A. W. Castleman, Jr., et al., "The Properties of Ion Clusters and their Relationship to Heteromolecular Nucleation," J. Chem. Phys., 68, 1760-7 (1978).
26. H. Reise, et al., "Translation-Rotation Paradox in the Theory of Nucleation," J. Chem. Phys., 48, 5553-60 (1968).
27. J. Zeldovich, Soviet Phys. JETP, 12, 525 (1942).
28. J. Lothe and G. M. Pound, "Reconsideration of Nucleation Theory," J. Chem. Phys., 36, 2080-5 (1962).
29. T.U.M.S. Murthy, et al., "Gas Phase Nucleation During the Thermal Decomposition of Silane in Hydrogen," J. Crystal Growth, 33, 1-7, (1976).
30. S. K. Friedlander, Smoke, Dust, and Haze, Chap. 7, John Wiley and Sons, New York, 1977.
31. J. Y. W. Seto, "Deposition of Polycrystalline Silicon by Pyrolysis of Silane in Argon," J. Electrochem. Soc.: Solid State Science and Technology, 122, 701-6 (1975).
32. J. Bloem, "Gas Phase Diffusion and Surface Reactions in the Chemical Vapor Deposition of Silicon," Pure Appl. Chem., 50, 435-47, (1978).

33. F. C. Eversteyn, et al., "A Stagnant Layer Model for the Epitaxial Growth of Silicon from Silane in a Horizontal Reactor," J. Electrochem. Soc: Solid State Science and Technology, 117, 925 (1970).
34. M. E. Jones and D. W. Shaw, "Growth from the Vapor," in Treatise on Solid State Chemistry, Vol. 5, N. B. Hannay, Plenum Press, New York, 1976.
35. H. L. Frisch and F. C. Collins, "Diffusional Processes in the Growth of Aerosol Particles, II," J. Chem. Phys., 21, 2158-65 (1953).

## CHAPTER V

### DISPERSION OF SILICON IN N-PROPANOL

by

G. Garvey and J. S. Haggerty

#### ABSTRACT

Dispersions of laser-formed silicon powders in n-propanol were evaluated. Parameters studied included boron doping, fraction solids and water concentration in the n-propanol. FTIR was used to evaluate the chemical composition of the powder. Powder agglomeration was evaluated by TEM and photon correlation spectroscopy; macroscopic dispersion stability was measured by sedimentation rates. Microelectrophoretic mobility was used to evaluate surface potentials.

The results are interpreted in terms of the DLVO model. In general, coulombic repulsion does not provide an adequate potential barrier because the double layer is very large in the alcohol. Water has an adverse effect on stability. It may be possible to achieve stable dispersions with ionic additions; but, steric stabilization by adsorbed macromolecules appears more likely to succeed.

#### V.1. INTRODUCTION

The objective of the dispersion task of this program is to find means of dispersing nonpolar, covalent particles in a manner that will permit defect free, high coordination number green bodies to be formed. Dispersion must be accomplished in liquids and with additives that will not degrade the properties of densified bodies. Superior microstructural characteristics and reduced sintering cycles have been demonstrated with  $\text{TiO}_2$ <sup>1</sup> with green bodies made from the special dispersions that are possible only with uniform diameter particles. This research strives to achieve similar results with Si,  $\text{Si}_3\text{N}_4$  and SiC powders produced by the laser heated gas phase synthesis process.

It was postulated<sup>2</sup> and now has been shown<sup>3</sup> that essentially defect free green ceramic bodies can be formed from ordered dispersions of ceramic

particles. The particles must conform to a rigid set of criteria for ordered dispersions to be feasible; principally they must be uniform in diameter and absolutely free of agglomerates. Conformance to other criteria requires specific particle sizes, purities and stoichiometries. The laser heated gas phase synthesis process generally appears capable of producing powders with these characteristics.

Establishment of ordered dispersions with minimum interparticle distances requires precise manipulation of interparticle forces thereby maximizing the volume fraction of solids. The theoretical understanding of these interparticle forces in nonaqueous liquids is far less developed than for ionic particles in aqueous liquids. Thus, our research has begun with empirical screenings and fundamental property measurements to permit definition of guidelines for feasible approaches.

The research supported by this program has focused on Si powders in alcohols, building on the research carried out in programs previously supported by ONR and ARO.<sup>4,5</sup> Dispersion research with laser synthesized SiC powders is being supported by DOE<sup>6</sup> and NASA<sup>7</sup>. Combined they will extend MIT's generic research in presintering science to this important class of ceramics.

Silicon was selected for these studies for several important reasons. Its higher overall purity, our ability to control particle size over wider range, the absence of crystalline polytypes and the nonexistence of the stoichiometry issue make Si a simpler system than the other two materials. It is an excellent choice for modelling dispersion of covalent materials in nonaqueous liquids. Also, the material has great technical importance for reaction bonded silicon nitride and reaction bonded silicon carbide.

Beyond the obvious adverse effect flaws have on strength, highly perfect green microstructures are particularly important for RBSN products. Specific surface areas and interparticle neck sizes control the uniformity and rates of nitridation; both issues have been troublesome in RBSN processing. In principle it should be possible to make nearly fully dense RBSN bodies without any dimensional change from the ordered, green Si bodies. Also, the absence of large diameter interparticle voids will improve the oxidation properties of RBSN<sup>8</sup>, permitting superior high temperature properties exhibited in nonoxidizing atmospheres to be retained in oxidizing atmospheres.



## V.2. THEORETICAL CONSIDERATIONS

Particles can exist in stable suspension if attractive and repulsive forces are equal in magnitude at a noncontacting distance and repulsive forces exceed attractive forces for interparticle distances less than the equilibrium distance. Thermally induced oscillations cause interparticle positions to change continuously about the equilibrium position; instability results if the repulsive force barriers are exceeded. Van der Waals forces attract particles, steric barriers repel, and coulombic forces can either attract or repel. Typically coulombic forces are used to repel particles against van der Waals attraction. Each force exhibits a different functional dependence on interparticle spacing and all are extremely sensitive to the properties of the specific materials (powders, solvents, solutes...).

The particle interactions are generally described in terms of an energy which is the integral of the force-distance relationship corresponding to bringing two particles from an infinite separation to a specific interparticle spacing. The total interaction energy is the sum of the individual contributions. The relative stability of a dispersion is dependent on the barrier height-to-thermal energy ratio.

A charged particle in a partially ionized medium will attract ions of the opposite sign which can either adsorb (Stern layer) onto the particle surface or remain in the medium surrounding the particle. These redistributed ions constitute the electrical double layer. When two such particles approach each other, the diffuse clouds of counter ions interact by repelling each other. The structure of the double layer is governed by the type and concentration of ions in solution ( $\sum n_i$ ), and the dielectric constant of the medium ( $\epsilon$ ) and the sign and magnitude of the surface charge. The double layer thickness,  $1/\kappa$ , is a measure of the structure of the double layer. It is both the thickness of an equivalent capacitor and the distance at which the electrical potential in the medium drops to  $1/e$  of the particle's surface potential ( $\psi_0$ ). This thickness is given by:<sup>9</sup>

$$1/\kappa = \left( \frac{\epsilon kT}{4\pi e^2 \sum n_i z_i^2} \right)^{1/2}$$

where  $e$  is the electronic charge,  $z_i$  is the valence of the ion  $i$ , and  $kT$  has its normal meaning.

The ionic concentration in a pure aqueous medium is approximately  $10^{-7}\text{m}$  at room temperature (defined by its self dissociation constant). Electrolytes are normally added to dispersions to control surface charge; typical ionic concentrations range from  $10^{-5}$  to  $10^{-1}\text{m}$ . These values result in double-layer thicknesses of  $0.1\text{ }\mu\text{m}$  and  $0.001\text{ }\mu\text{m}$  respectively. In pure n-propanol, the ionic concentration is approximately  $10^{-9}\text{m}$ ; the resulting double-layer thickness is approximately  $2\text{ }\mu\text{m}$  as shown in Figure V.1. The addition of an organic salt which dissociates to a high degree in n-propanol may be useful in condensing the double layer thickness ( $1/\kappa$ ), although, surface charge neutralization may occur.

Although the equations that govern the coulombic interactional energies have not been solved explicitly, solutions exist for the limiting cases of large double layers ( $\kappa a < 2$ ) and small double layers ( $\kappa a > 5$ ) where  $a$  = particle radius. Organic dispersions fall into the former case with  $\kappa a \approx 0.01$  for  $0.1\text{ }\mu\text{m}$  diameter Si particles in n-propanol. For this case, the coulombic repulsive potential ( $V_R$ ) as a function of interparticle distance ( $\Delta$ ) is given by:<sup>9</sup>

$$V_R = \frac{\epsilon a^2 \psi_0^2}{\Delta + 2a} \beta e^{-\kappa \Delta},$$

where  $\beta$  is a geometrical correction factor which ranges from 0.6 to 1.0. An error of less than one percent results from ignoring the exponential term for  $\kappa \Delta < 0.01$  (i.e.  $\Delta < 500\text{\AA}$ ). The denominator is dominated by particle radius for close interparticle spacings, so the potential barrier does not rise rapidly as the particles approach.

There are three mechanisms for generating surface charge and thus surface potential, in the systems under consideration. These are:

- Distribution of electrons within the semiconducting particles: Surface states can adsorb electrons or holes resulting in the development of a surface charge.<sup>10</sup>
- Adsorption of dipolar molecules: The adsorption of neutral dipolar molecules from solution can effect the space charge<sup>11</sup> distribution in the double layer.
- Surface reaction: Any reaction that results in the production and desorption of ions at the surface will generate a surface charge;<sup>11-15</sup> e.g., Bronsted and Lewis mechanisms.

Surface charge in silicon is expected from some combination of all three of these mechanisms. The magnitudes of each are interdependent. Electronic distribution can be most easily manipulated by varying the dopant level in the silicon and by the specific electrical characteristics of the solvent. Dipolar effects scale with the dipole moment of the solvent. Surface reaction is manipulated by controlling the solid surface and solvent chemistries. The sign of each contribution can be either positive or negative. Because the potential decays slowly from the surface in nonaqueous liquids, the surface potential can be equated to the  $\zeta$ -potential.<sup>14</sup> The magnitude and sign of the net surface potential can be measured by electrophoretic experiments.<sup>11</sup>

The van der Waals potential energy between two equal diameter particles of the same material is given by:

$$V_A = - \frac{A}{12} \left( \frac{1}{x^2 + 2x} \right)$$

where  $x$  is  $\Delta/2a$  and  $A$  is the Hamaker constant. Because the denominator goes to zero as  $\Delta$  goes to zero, these forces become large for small interparticle spacing. Literature values of  $A$  used in the following calculations are summarized in Table V.1.

Steric interference causes repulsive forces between interacting particles with adsorbed macromolecular layers. The magnitude of the repulsive force depends on the macromolecule size, adsorption density and conformation. Most of the theories for steric stabilization can be classified in either entropic or osmotic categories. Decreased configurational entropy caused by compressed, interpenetrating adsorbed molecules is responsible for repulsive forces in the entropic theory.<sup>15-20</sup> For the osmotic theory, the repulsive forces result from a combination of positive enthalpic change and reduced configurational entropy during interparticle collisions.<sup>21-24</sup> Entropic and osmotic repulsion theories have been tested by many authors and both have been found to apply for specific systems.

Although there is relatively little guidance for steric stabilization in the Si/n-propanol system, this approach must be considered very important in light of the diffuse nature of coulombic repulsive potentials. Steric repulsive forces operate at interparticle distances approximately the same as

TABLE V.1

## HAMAKER CONSTANTS

<u>Material Interaction</u>	<u>A (J x 10<sup>20</sup>)</u>
Si-Si	25.6*
n-Propanol-n-Propanol	5.0 <sup>+</sup>
H <sub>2</sub> O-H <sub>2</sub> O	4.4*

\* J. Visser, "On Hamaker Constants", Adv. Coll. Inter. Sci., 3,331-63, 1972.

<sup>+</sup> B. Vincent, "The van der Waals Attraction Between Colloidal Particles Having Adsorbed Layers. II", J. Coll. Inter. Sci., 42, 270-85, 1973.

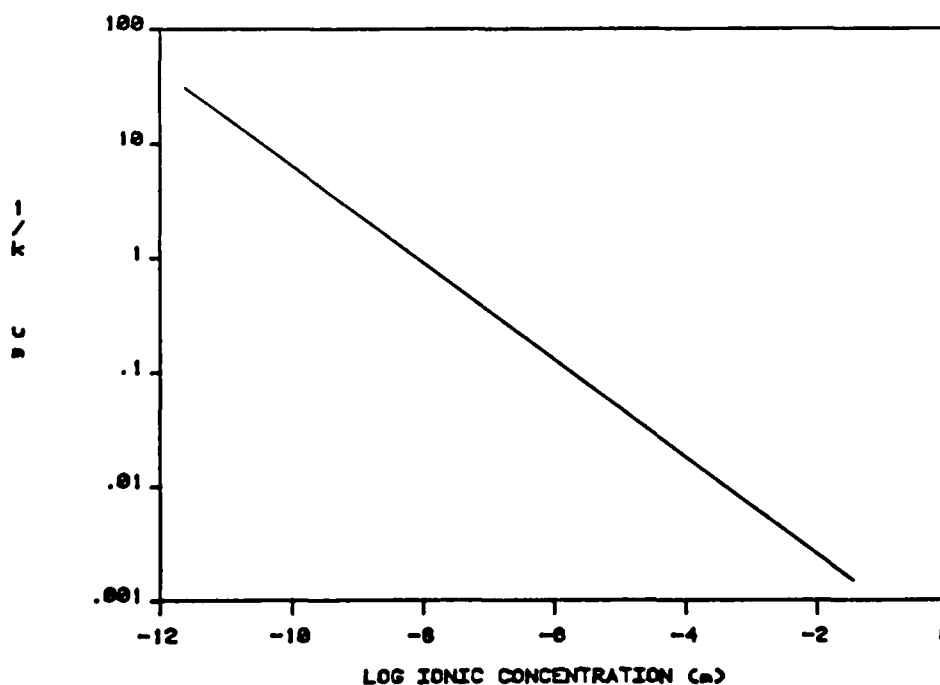


Figure V.1. Double layer thickness as a function of ionic concentration,  $\epsilon = 20.4$ ;  $T = 300^\circ\text{K}$ .

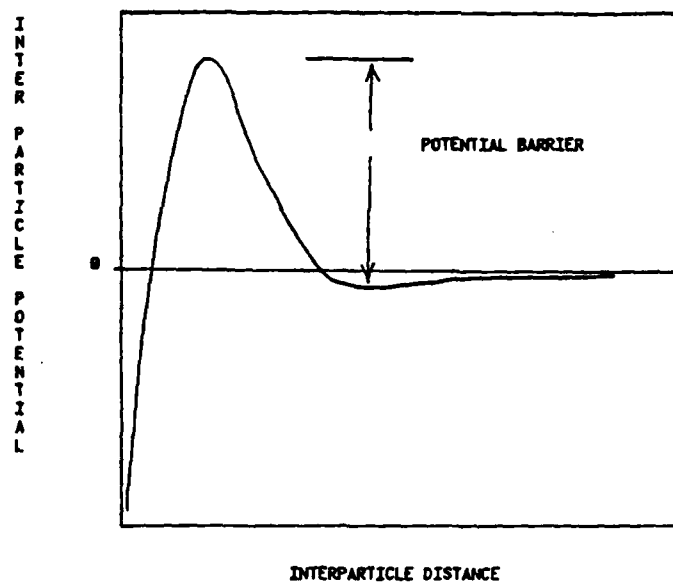


Figure V.2. Schematic of interparticle energies for a typical stable aqueous dispersion.

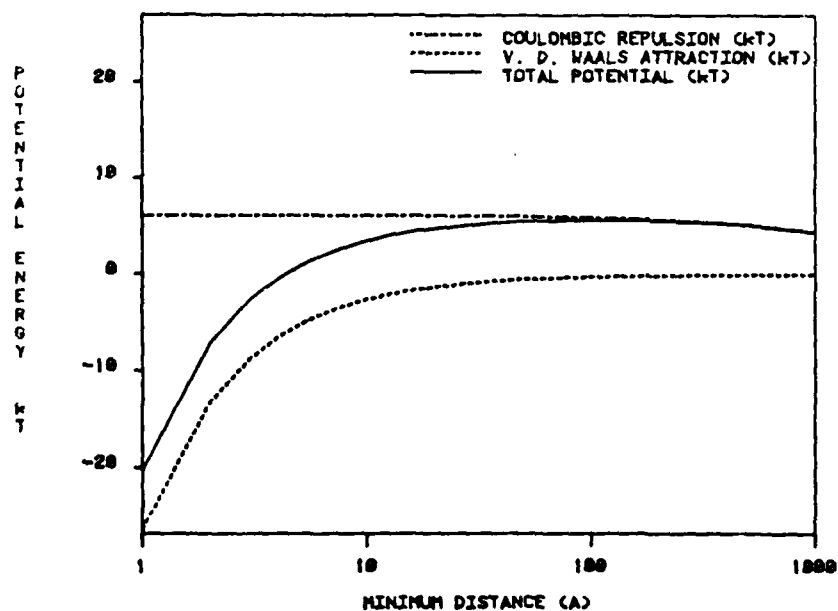


Figure V.3. Interparticle energies for charged silicon particles in n-propanol as a function of interparticle distance; particle radius =  $400\text{\AA}$ ; surface charge =  $80\text{ mV}$ ;  $[\text{ion}] = 1 \times 10^{-9}\text{ M}$  at  $300^\circ\text{K}$ .

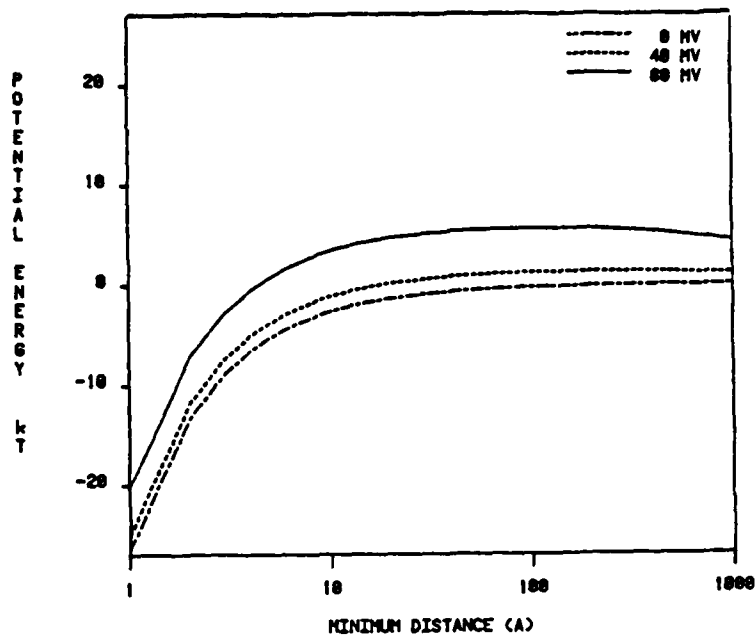


Figure V.4. Interparticle energies for silicon in n-propanol as functions of interparticle distance and surface charge. Radius =  $400\text{\AA}$ ;  $[\text{ion}] = 1 \times 10^{-9} \text{ m}$ ;  $T = 300^\circ\text{K}$ .

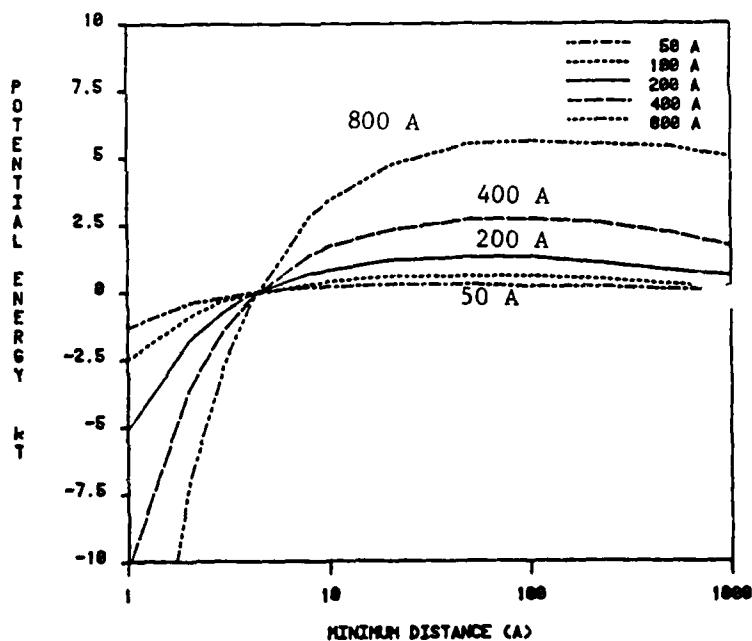


Figure V.5. Interparticle energies for silicon in n-propanol as functions of interparticle distance  $\Delta$  and particle radius.  $\psi_0 = 80 \text{ mV}$ ;  $[\text{ion}] = 1 \times 10^{-9} \text{ m}$ ;  $T = 300^\circ\text{K}$ .

the macromolecule sizes. Thus, they provide repulsive forces that operate on the same scale as the van der Waals forces. If balanced, their use can produce a stable dispersion with very small interparticle spacings; a critical feature for achieving a high percentage of solids in green bodies with small particles.

The van der Waals and coulombic potential terms included in Figures V.2 and V.3 compare these interactional energies in a typical stable aqueous dispersion and in a Si/n-propanol dispersion respectively. A substantial potential barrier is developed in the aqueous example (Figure V.2). If this barrier is greater than 10 kT, the dispersion will be stable to flocculation for a period of days. In contrast, the maximum potential is less than 10 kT and the potential barrier is very diffuse for the nonaqueous example, Figure V.3. Substantial changes in the interparticle distance result in relatively minor changes in potential. For example, the increase in potential experienced by two particles as they approach a separation of 100Å from an initial distance of 1000Å is small, on the order of 1 kT. This approach can be driven by thermal energy. Once the particles reach a distance of 100Å, agglomeration is energetically favored. Such a dispersion is not stable.

Figures V.4 and V.5 show the effects of surface potential and particle diameter for Si particles in n-propanol. These plots are similar to those of Figure V.3; the potential barriers are small and diffuse. Varying the particle size or surface potential within these limits (0 to 80 mV, 50 to 800Å) does not result in stable dispersions.

The Vold<sup>25</sup> approach can be used to predict the effects of an adsorbed water layer on the van der Waals potential. A brief discussion of this model is given by Parfitt<sup>11</sup>. In short, the model assumes that the total van der Waals' potential of two particles with adsorbed layers is the sum of the interactions of each of the phases with every other phase present in the system. The adsorbed layer is treated as a sphere of liquid with a sphere of the particle's geometry subtracted from it. Figure V.6 shows that for all interparticle separations, adsorbed water increases the van der Waals attractive potential. The presence of a 20Å layer of pure water may change the surface potential substantially, but is not expected to affect the diffuse double layer structure significantly. On the basis of these results

it is expected that dispersions of silicon in n-propanol containing water should be less stable than those without water.

In summary, interparticle forces have the same origins in aqueous and nonaqueous liquids; however, their character differs. The nature of the coulombic repulsive potential between silicon particles in pure n-propanol is the most important difference. In contrast to aqueous dispersions, the weak, diffuse coulombic repulsion does not provide a sufficient potential barrier to prevent coagulation. Although the approach is unproven, it may be possible to compress the coulombic barrier (make less diffuse) and increase the surface potential with easily dissociated electrolytes as is done with aqueous dispersions. Steric stabilization appears particularly important for these dispersions because these forces act on very small interparticle distances providing the opportunity to achieve stability with high percent solids of small particles. Water impurities can be anticipated to reduce stability through increased van der Waals attraction. Experiments were designed to examine these issues.

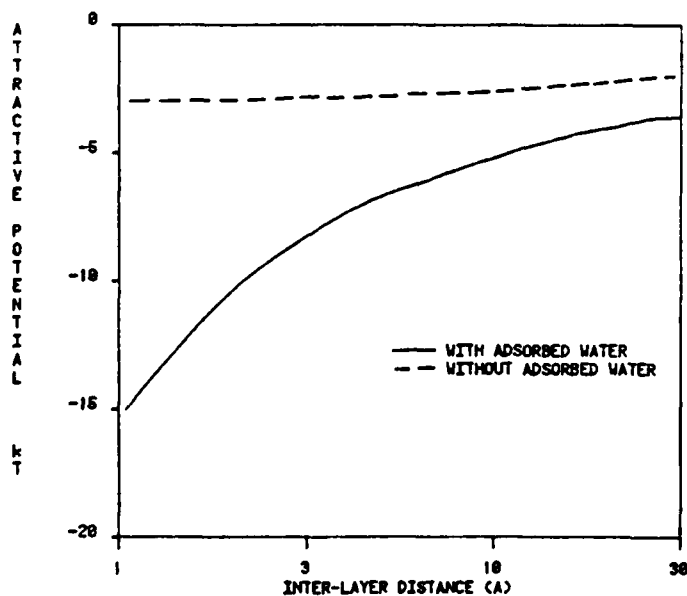


Figure V.6. Interparticle attraction of silicon in n-propanol with and without adsorbed water. Radius =  $100\text{\AA}$ ; water layer thickness =  $20\text{\AA}$ ;  $T = 300^\circ\text{K}$ .



### V.3. PROCEDURES

#### V.3.A. IR Spectroscopy

The infra-red spectra (IR) of two silicon powders (226S and 227SB) were obtained using a Nicolet 7000 FTIR. Pressed pellets were prepared by milling 0.1 mg of silicon powder with 0.4 g IR-grade KBr obtained from Fisher Scientific. Pellets were pressed in a round 1.27 cm diameter Perkin-Elmer stainless steel die to  $1.4 \times 10^2$  MPa. A blank sample was similarly prepared at the same time for background determination. After the spectra were obtained and stored, the base line corrections were made by subtracting the blank's spectrum.

#### V.3.B. Specific Surface Area, TEM and Photon Correlation Determinations of Particle and Agglomerate Sizes

Specific surface areas were determined by single-point BET analysis with a 30% N<sub>2</sub>-70% He atmosphere. Equivalent spherical diameters were calculated assuming a density of 2.33 (g/cm<sup>3</sup>).

Particles and agglomerate sizes were measured after powders had been dispersed. The dispersions were formed in the following manner. A 10 mg sample of dry powder was weighed into a Pyrex<sup>™</sup> scintillation vial in a dry, deoxygenated, nitrogen-filled glove box. The vial was stoppered with a rubber septum and removed from the box. Stock n-propanol (10 ml) was injected into the vial via a polypropylene syringe. The water content in the alcohol was determined to be ~ 250 ppm by weight using Karl Fisher Reagent (KFR) titration. The vial was shaken and sonicated using an Ultrasonics and Heat Systems model W-220 ultrasonicator at a setting of 6 for three minutes. The exterior of the vial was maintained at room temperature using a water bath.

For photon correlation (PC) measurements, the dispersion was transferred to a PC cuvette and evaluated in a Malvern K7025 Photon Correlator. Both the transfer of the dispersed particles and the PC characterization were done with air exposures. Measurements were initiated 2 minutes after the cessation of sonication. For TEM measurements, a carbon TEM film grid was dipped into the dispersion 2 minutes after sonication then dipped into pure n-propanol. The second dip prevented a nonrepresentative sample of silicon dispersion from concentrating on the grid as the alcohol evaporated. It is

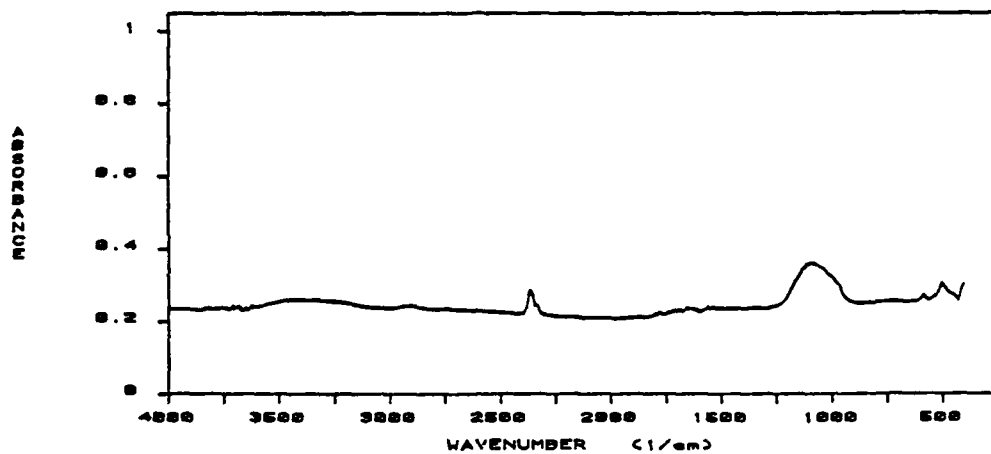


Figure V.7. FTIR absorbance plot of sample 226S; KBr pellet.

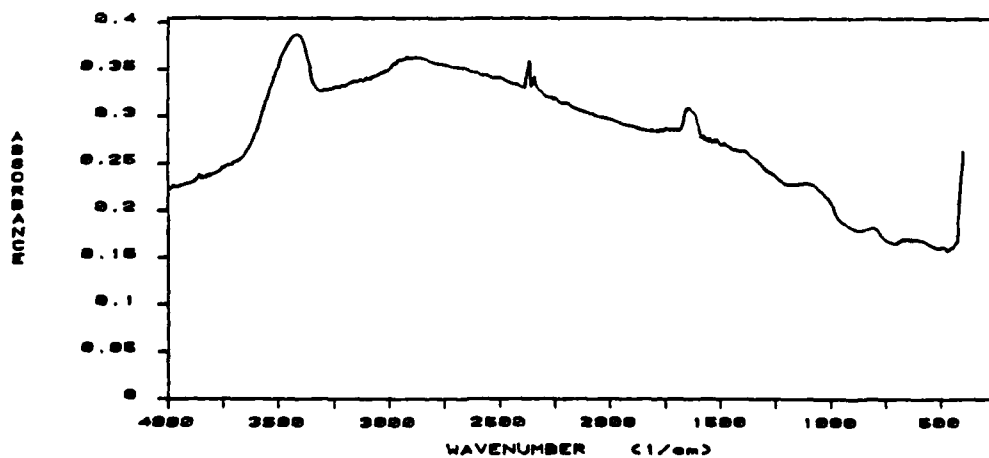


Figure V.8. FTIR absorbance plot of sample 227SB; KBr pellet.

AD-A144 439

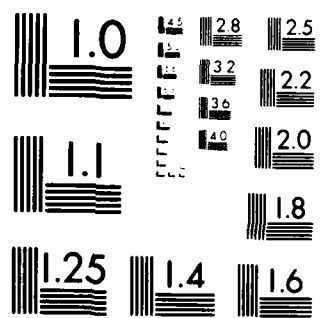
SINTERABLE CERAMIC POWDERS FROM LASER HEATED GAS PHASE  
REACTIONS AND RAPID (U) MASSACHUSETTS INST OF TECH  
CAMBRIDGE ENERGY LAB J S HAGGERTY JUL 84 MIT-EL-84-009  
N00014-82-K-0350

UNCLASSIFIED

F/G 11/2

NL

END  
DATE  
FILMED  
9 84  
DTIC



MICROCOPY RESOLUTION TEST CHART  
NATIONAL BUREAU OF STANDARDS-1963-A

believed that the silicon agglomerates that remained on the film were representative of the agglomerates in the 10 ppm dispersion although this is difficult to demonstrate unequivocally.

The effects of water on the agglomerate size were determined by photon correlation. Three dispersions were formed as described above, starting with stock n-propanol containing approximately 250 ppm by weight water. A small amount of water was added to two of these vials gravimetrically bringing the water contents to 2740 and 13,700 ppm by weight. The dispersions were ultrasonicated, transferred to PC vials and assessed for agglomerate size as a function of time.

### **V.3.C. Electrophoretic Mobility Determinations**

Microelectrophoretic mobility was determined by the method described by R. J. Hunter<sup>26</sup> using the Rank Brothers apparatus. A cylindrical vitreous silica electrophoretic cell with 2 mm ID was used. Applied fields ranged from 3 to 7 V/cm.  $\zeta$ -potentials were calculated as indicated in the cited reference. Typical values ranged from -30 to -70 mV. A minimum of forty measurements were made at two different voltages with direction alternated. N-propanol used in this study was distilled after drying over 4x molecular sieves for 3 days or was used in the as-received condition. Water content was determined by Karl Fisher reagent titration. All glassware was dried with a heat gun in a N<sub>2</sub> glove box; the O<sub>2</sub> and H<sub>2</sub>O content in the box was minimized by a copper getter. The microelectrophoretic cell was loaded and capped in the glove box.

A 0.04 wt.% dispersion of silicon was prepared with water assayed n-propanol as described above. This was again diluted by a factor of 100:1 with the appropriate n-propanol solution to produce a 4 ppm by weight dispersion which was sonicated as previously described. The diluted dispersion was used for microelectrophoretic mobility determination.

## **V.4. RESULTS AND DISCUSSION**

### **V.4.A. IR Study**

The FTIR spectrographic analyses of undoped and boron doped Si powders are shown in Figures V.7 and V.8 respectively. The spectrum of the boron doped powder (Figure V.8, 227-SB) has a very broad spectral roll centered at

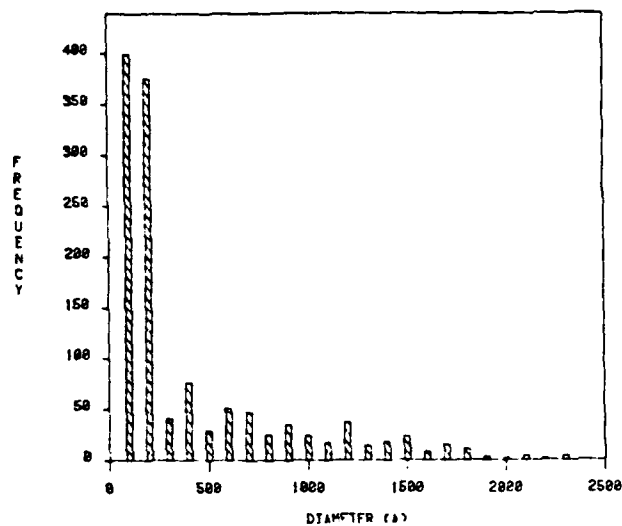


Figure V.9. TEM particle size distribution of sample 226S.

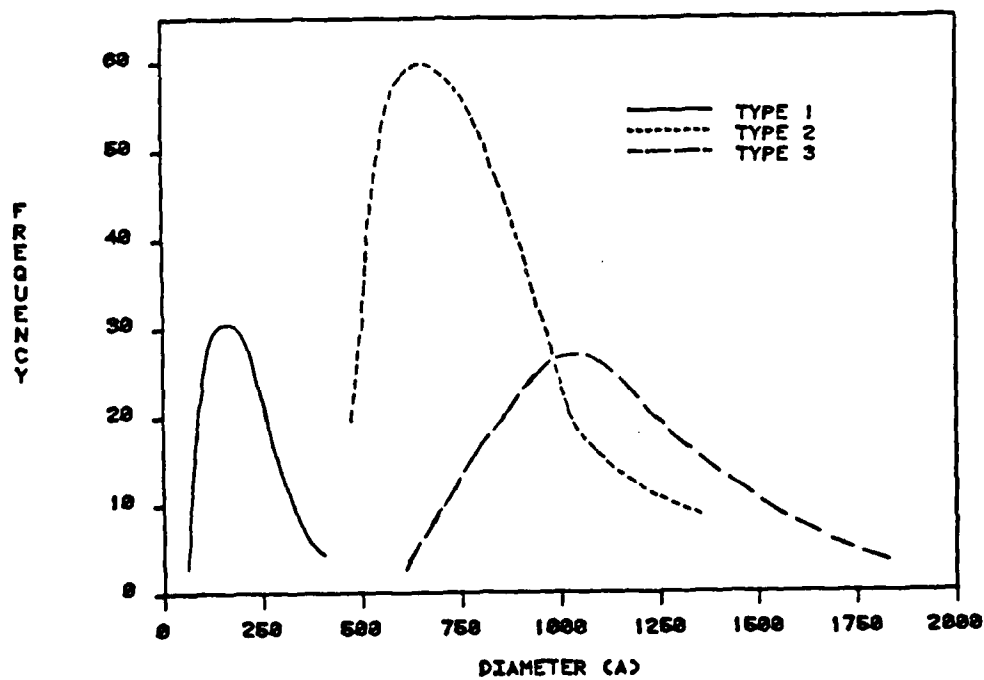


Figure V.10. TEM particle size distribution of sample 227SB.

2200  $\text{cm}^{-1}$ . V. S. Vavilov, et al.<sup>28</sup> have reported a similar, less intense spectral feature for boron doped single crystal silicon.

Two large absorption bands at 3435  $\text{cm}^{-1}$  and 1645  $\text{cm}^{-1}$  are apparent in the spectrum of 227-SB that are not present in the spectrum of 226-S. O-H stretching vibrations of the water molecule lead to a very broad and intense band near 3400  $\text{cm}^{-1}$  and H-O-H bending vibrations of molecular water lead to a band near 1650  $\text{cm}^{-1}$ .<sup>29</sup> In contrast, surface hydroxyl in the form of silanol, SiOH, is characterized by a very narrow band<sup>29</sup> near 3750  $\text{cm}^{-1}$ . This species does not produce a band near 1650  $\text{cm}^{-1}$ . As water adsorbs on a silanol surface the band at 3750  $\text{cm}^{-1}$  decreases in intensity and is displaced to lower frequencies<sup>29</sup> until the peak is obscured by the water spectrum. The observed results may be explained by concluding that the boron doped silicon is hydroxylated and covered by an adsorbed layer of molecular water. Pure silicon has neither adsorbed water nor a hydroxylated surface because neither of the characteristic peaks are observed.

Both spectra contain broad, small absorbance peaks at the low wave numbers. A peak centered at 1100  $\text{cm}^{-1}$  is most easily discerned in the 226-S spectrum. Many absorption bands in this region (e.g. 1106  $\text{cm}^{-1}$ , 1136  $\text{cm}^{-1}$ , 1127  $\text{cm}^{-1}$ , 1130  $\text{cm}^{-1}$  and 1111  $\text{cm}^{-1}$ ) have been examined and attributed to lattice oxygen impurities.<sup>30,31,32</sup>

Peaks observed in the 420-640  $\text{cm}^{-1}$  region may be due to a Si-O-Si symmetric stretch.<sup>33</sup> Also, Si-H species (e.g. SiH and SiH<sub>2</sub>) exhibit vibration modes in this region. Such species can be anticipated, being products of silane decomposition. The appearance of a peak at 2350  $\text{cm}^{-1}$  reinforces the case for the presence of SiH which has a peak assigned in this region.<sup>34</sup>

In summary, it appears that both powders contain some subsurface, lattice oxygen contamination. This implies that a small amount of oxygen enters the system during the synthesis process. Possible sources include contamination of the reactant and shielding gases and leaks. In addition the boron-doped silicon (227-SB) has adsorbed molecular water and perhaps some surface silanol unlike the pure silicon. This water is probably introduced during transfer of the powder after forming. A hydroxylated surface is expected to exist for this powder but its broad characteristic peak is obscured by water of hydration which has a large similar peak in this region. The disposition of the B-doped silicon to adsorb water corresponds to other

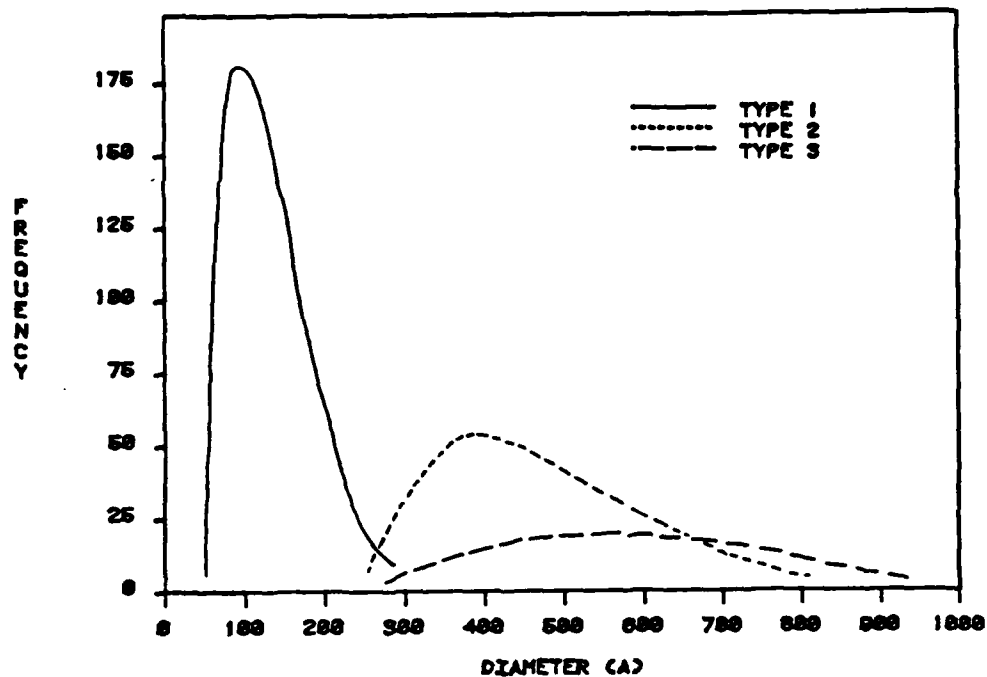


Figure V.11. TEM particle size distribution of sample 806SB.

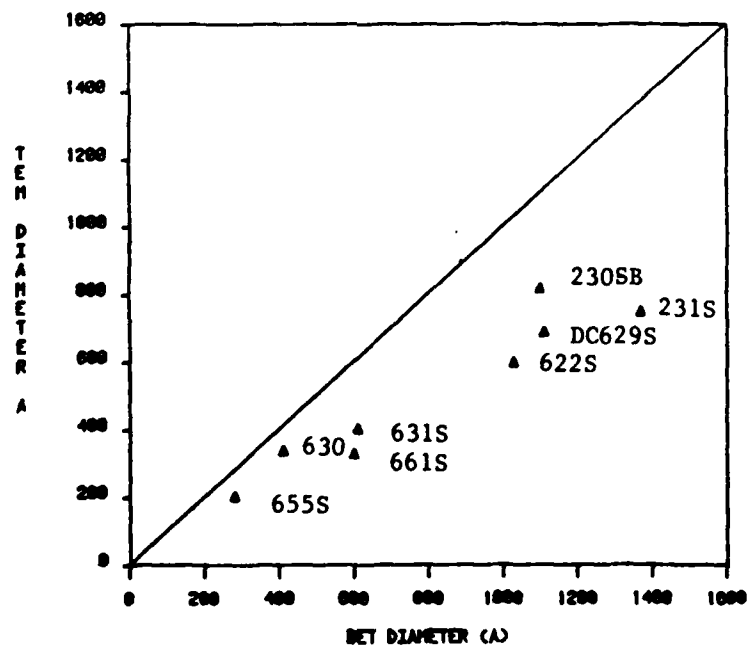


Figure V.12. BET equivalent spherical diameters versus TEM arithmetic means for eight silicon powders.



independent observations. Dahlén<sup>35</sup> showed that boron doped silicon is wetted by water while nonoxidized, pure silicon powder is not wetted by water and floats on the surface. From peaks appearing at  $2350\text{ cm}^{-1}$ ,  $495\text{ cm}^{-1}$  and  $570\text{ cm}^{-1}$ , it is concluded that SiH is also present in the powders.

#### V.4.B. Particle and Agglomerate Size Distributions

Samples were prepared for particle size analysis as described in Section V.3.B. Particle size measurements were made from TEM photomicrographs. A minimum of 400 particles were sampled randomly from each powder sample. The results are reported in Figures V.9, V.10 and V.11.

Figures V.10 and V.11 reflect the observance of three different types of particles. Type one particles are small ( $< 300\text{\AA}$ ), have a narrow particle size distribution and commonly occur in agglomerates of more than twenty. It is not evident from the micrographs whether these particulate assemblages are hard aggregates (i.e. have sintered necks). However it is apparent that they either are not dispersed by the applied techniques or agglomerate during TEM sample preparation. The type two particles referred to in Figures V.10 and V.11, with an average diameter of  $500\text{\AA}$ , commonly occur in chainlike agglomerates some of which appear to be aggregated. The number of particles per agglomerate,  $\sim 5$ , is less than the number for agglomerates of type one particles. The type three particles are large and spherical, occurring normally as single, non-agglomerated particles. The weight fractions of each type depend on the individual powder sample.

The results of TEM particle size distributions were compared with BET equivalent spherical diameter measurements. The TEM arithmetic means are compared with BET equivalent spherical diameters in Figure V.12. As expected, the TEM arithmetic means are consistently lower than BET equivalent spherical diameters which weight larger particles more. Figure V.13 applies the BET weighting factor to the TEM particle size distributions. There is very good agreement between the two methods; however, the TEM values are again consistently smaller. This small difference may result from neck formation between the particles because simple particle-particle contact does not account for all of the discrepancy.

The number of particles per agglomerate are presented in Figures V.14 and V.15. Many of the particle assemblages are singlets or doublets. This plot represents nearly the maximum dispersion possible by the sample

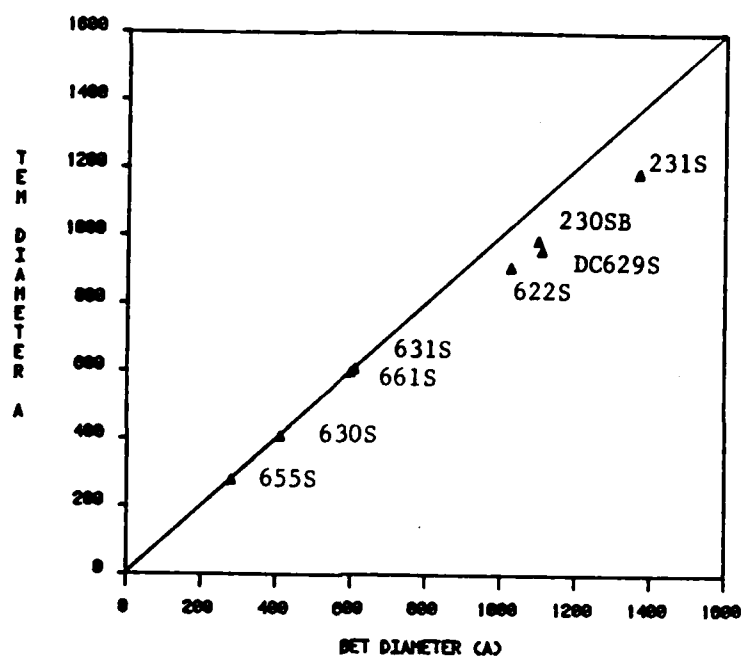


Figure V.13. BET equivalent spherical diameters versus TEM weighted mean diameters for eight silicon powders.

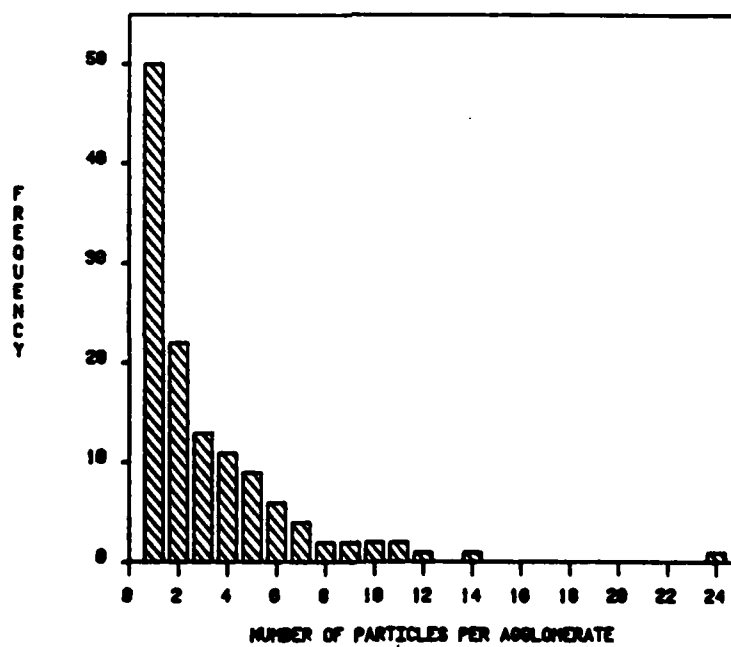


Figure V.14. TEM agglomerate size distribution for sample 226S.

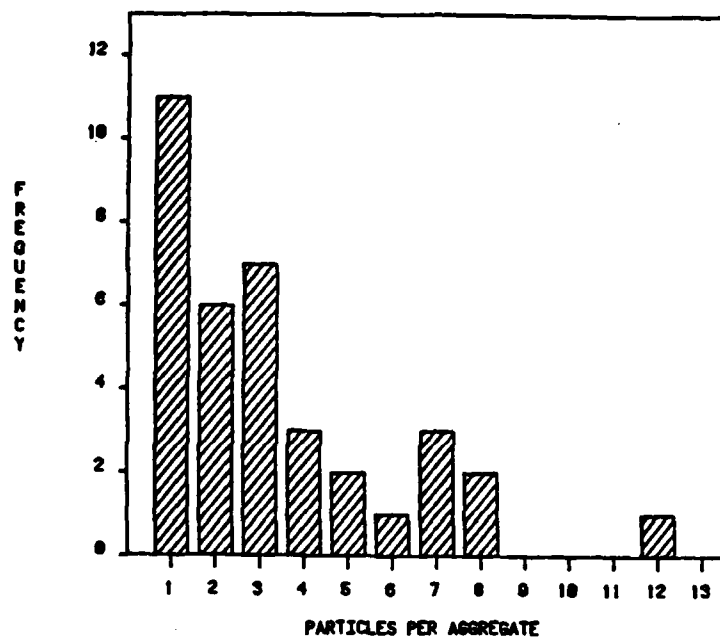


Figure V.15. TEM agglomerate size distribution for sample 231S.

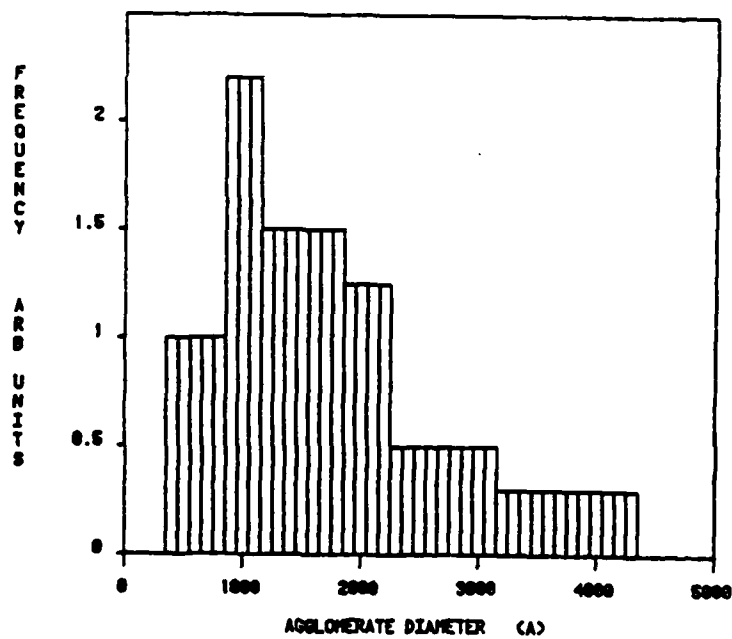


Figure V.16. TEM agglomerate size distribution for sample 806SB; 10 ppm silicon in n-propanol.

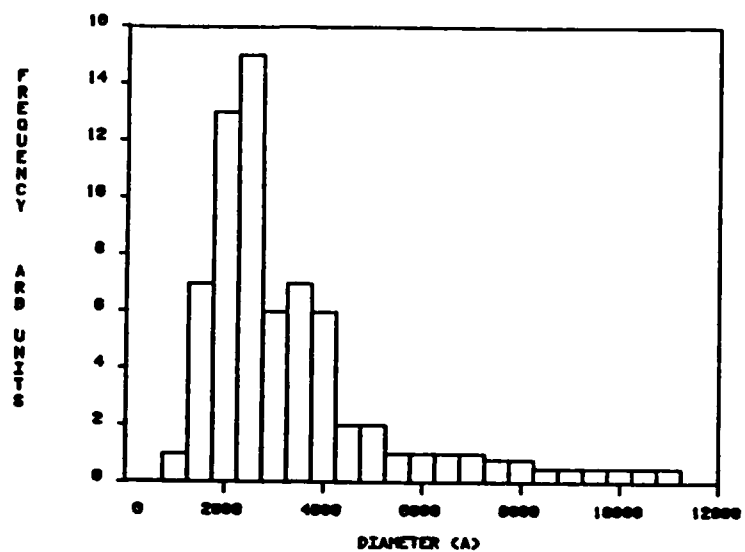


Figure V.17. TEM agglomerate size distribution for sample 226S; 10 ppm silicon in n-propanol.

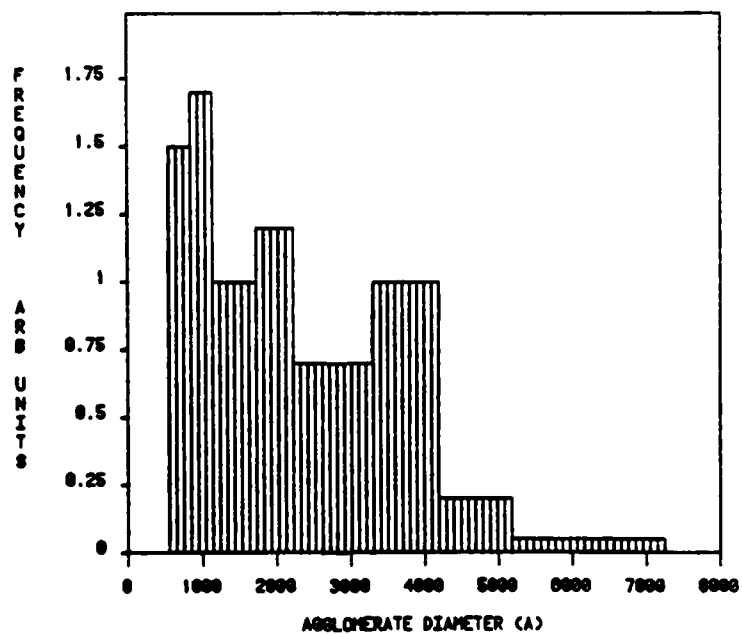


Figure V.18. TEM agglomerate size distribution for sample 227SB; 10 ppm silicon in n-propanol.

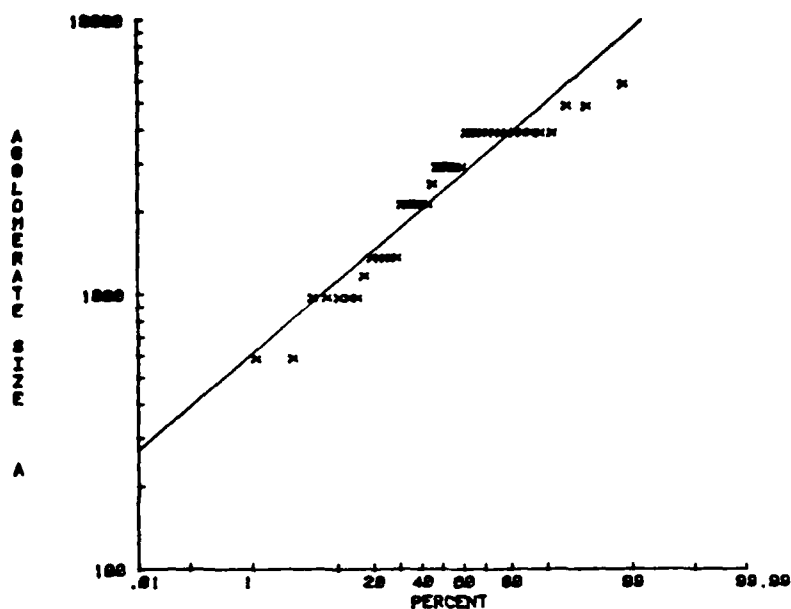


Figure V.19. Log-normal agglomerate size plot of data in Figure V.16 sample 806SB.

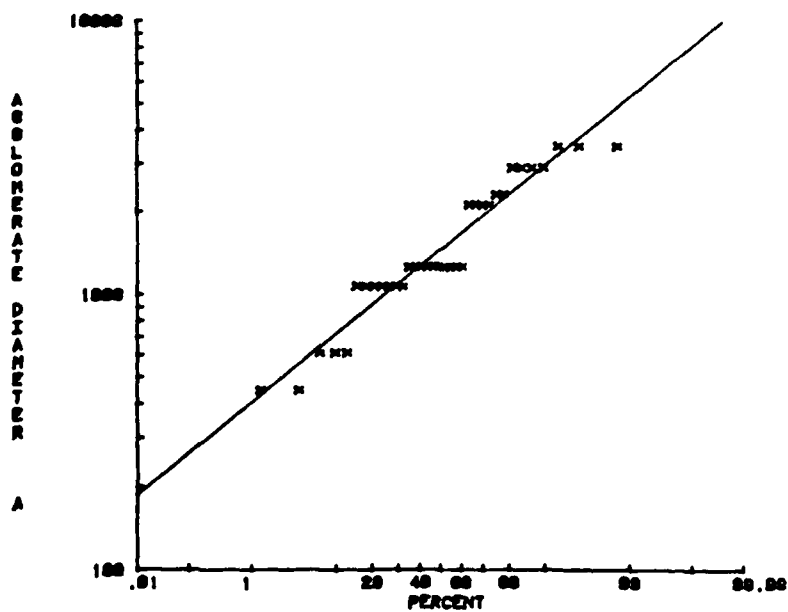


Figure V.20. Log-normal agglomerate size plot of data in Figure V.17 sample 226S.

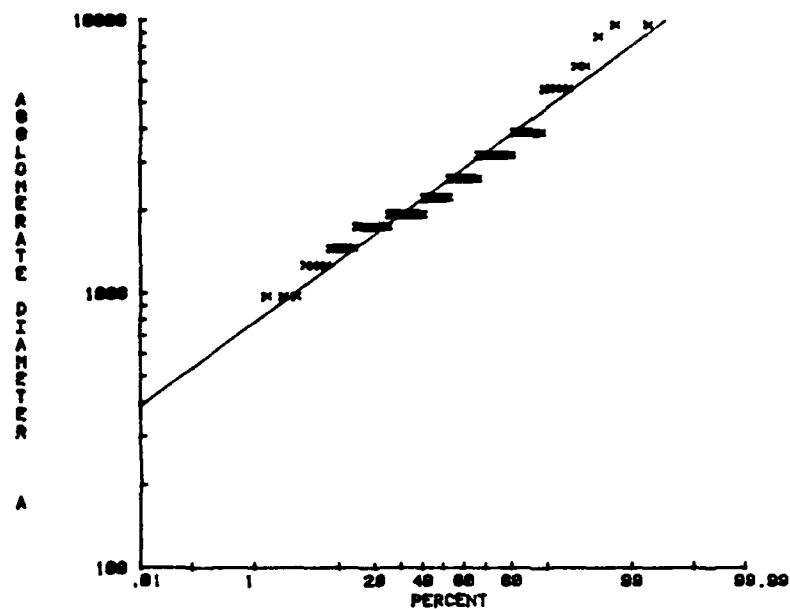


Figure V.21. Log-normal agglomerate size plot of data in Figure V.18 sample 227SB.

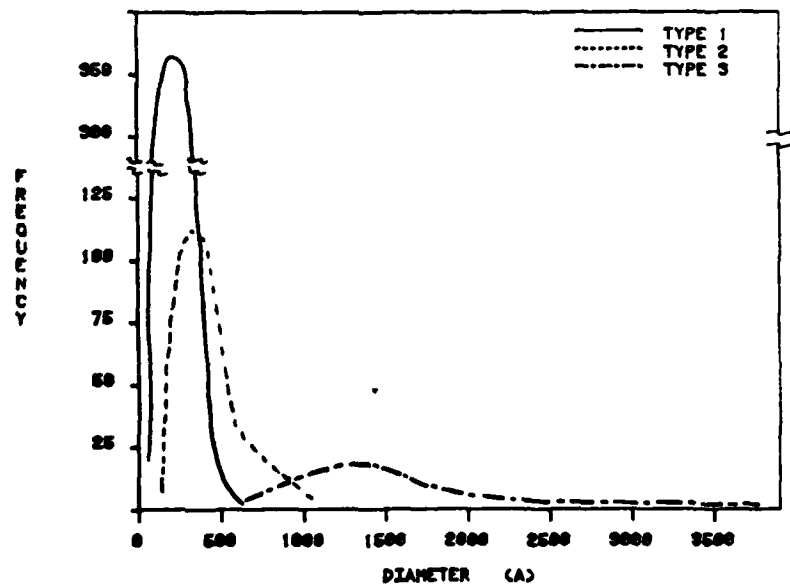


Figure V.22. TEM particle size distribution for sample B004S showing three types of particles. Bar length = 10,000Å.

preparation procedure, as samples were taken only a few minutes after sonication.

Figures V.16, V.17 and V.18 report the results of the TEM agglomerate size distribution study. The type of distribution must be known to properly characterize these results with respect to statistical means and standard deviations. The results were tested for their agreement with log-normal, normal, Weibull, exponential and logistic distributions. The log-normal distribution gave good straight line agreement as indicated in Figures V.19, V.20 and V.21. Values of the log-normal means and standard deviations are tabulated in Table V.2. The values of the means and standard deviations obtained by photon correlation are also tabulated in Table V.2. Very good agreement is found to exist between the TEM and the photon correlation distribution means. The standard deviations differ somewhat more but are within acceptable limits.

The effect of centrifugal separation on particle size and type was studied with powder B-004-S. This powder was chosen because it had a large fraction of type three particles, Figure V.22. A 0.1 wt.% dispersion in n-propanol was prepared as described in V.3.B. The dispersion was centrifuged for a time and speed calculated to settle 2000Å particles from the top of the container. The supernate was decanted and the sediment redispersed in fresh n-propanol a total of three times. A TEM micrograph of the final product is presented in Figure V.23. The majority of the particles are large, spherical and unaggregated. Also, there is a narrow particle size distribution which is necessary for the formation of ordered compacts.

These characterization results provide a self consistent description of the powders. The standard deviation of particle sizes is fairly small, usually less than half the mean. Three types of particles have been observed. Type one particles are found in agglomerates of nominally 30 small particles, type two in agglomerates of nominally 5 intermediate size particles and type three particles are completely dispersable singlets. The diameters of type one and two agglomerates are approximately equal to the largest type three particles.

#### V.4.C. Zeta Potential Measurements

The apparent  $\zeta$ -potential must be interpreted with care because agglomeration affects the agglomerate's total charge and drag coefficient

TABLE V.2  
A COMPARISON OF TWO METHODS OF AGGLOMERATE  
SIZE DISTRIBUTION CHARACTERIZATION

Sample	BET	TEM		PC	
	Equiv. Spher. Dia. (Å)	Mean (Å)	Std. Dev. (Å)	Mean (Å)	Std. Dev. (Å)
806-SB	460	1380	307	1250	420
226-S	1200	2720	766	2950	930
227-SB	850	2310	790	2500	700

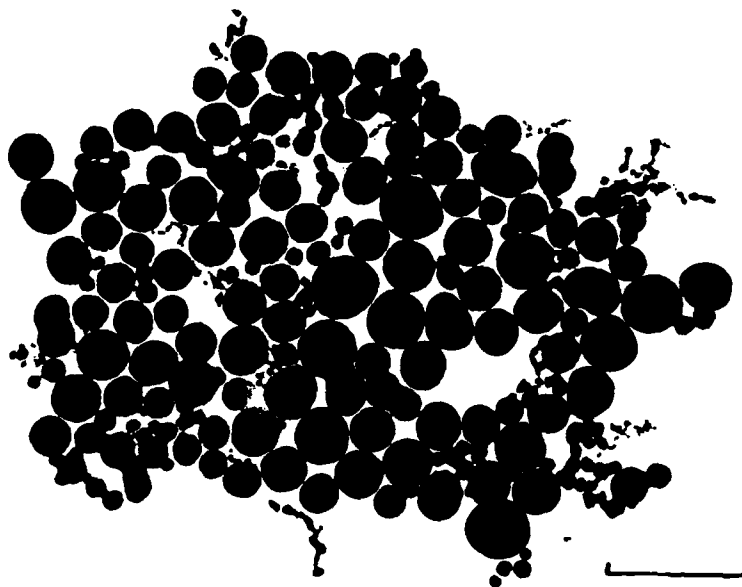


Figure V.23. TEM micrograph of centrifuged sediment of sample B004S. Bar length = 10,000Å.



through its cross-sectional area. As will be shown in the next section, dilute dispersions of both pure and boron doped Si powders did not exhibit continued agglomeration in n-propanol when the water content was less than 275 ppm by weight. Thus, the calculated  $\zeta$ -potentials provide a qualitative measure of surface potential even if the population contains agglomerates.

The results in Table V.3 show that water causes  $\zeta$  to increase for both pure and boron doped powders and that  $\zeta$  for pure Si is constantly higher than for the boron doped Si. The latter result is surprising because FTIR and wetting experiments showed that the boron doped Si has a relatively high affinity for water. The effect of adsorbed water at the particle-liquid interface on  $\zeta$ -potential can be interpreted as resulting from the partial hydroxylation of the surface followed by partial deprotonation. This results in a negative surface charge as is the case for silica in aqueous dispersions. Hunter<sup>17</sup> reports a  $\zeta$ -potential of -110 mV for silica at low ionic concentration ( $10^{-4}M$ ). The Si  $\zeta$ -potential remains below this value because it is expected that hydroxylation will remain incomplete throughout the water concentration range investigated. The trend of increasing  $\zeta$ -potential with increased water concentration is consistent with these expectations. It is concluded from these results that the dominant charge generating mechanism in this system is a surface chemical reaction.

#### V.4.D. Dispersion Stability

The sedimentation of dispersions and the agglomeration rate of samples prepared as described in Section V.3.B. were observed. Weight concentrations of silicon (227-SB) in n-propanol ranged from 4 ppm to 3% in the stock n-propanol solution. With higher water contents, the Si concentration was maintained at 4 ppm.

The sedimentation rates were measured for stock n-propanol containing 275 ppm  $H_2O$ . A sediment layer was observed after 24 hours for the highest concentration of silicon; a clear supernate developed with longer times. Lower concentrations of silicon produced sediment at longer times; a fine layer appeared in the 10 ppm dispersion after 1 week. Clear supernate did not form in the suspensions when the initial silicon concentrations were less than 0.1 wt.%, instead a cloudy suspension remained for months. Quantifying previous observations,<sup>35, 36</sup> high stability was demonstrated at low concentrations but not at high concentrations.

TABLE V.3

ZETA POTENTIALS OF SILICON POWDERS  
IN N-PROPANOL WITH VARIED WATER CONCENTRATION

Silicon Sample (Run #)	Water (ppm)	$\zeta$ -Potential (mV)
226-S	275	-60
226-S	40	-33
227-SB	275	-55
227-SB	40	-29

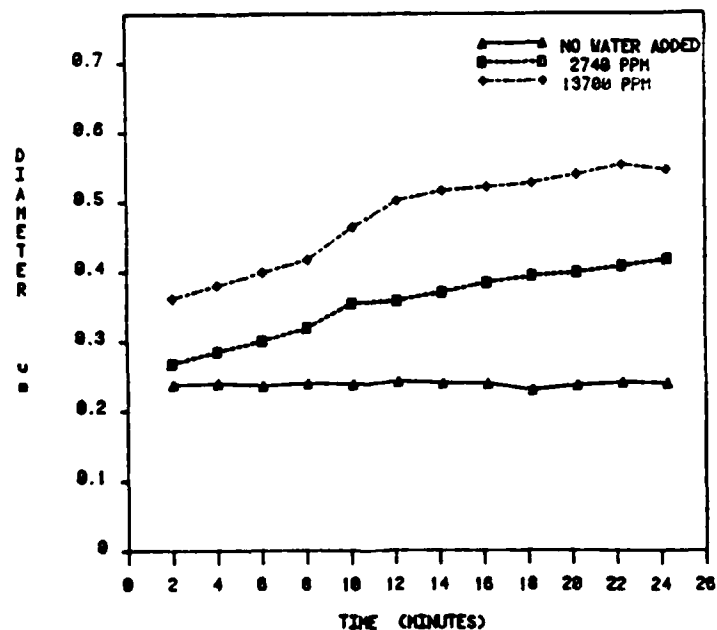


Figure V.24. The effect of water on the rate of agglomeration as measured by photon correlation. Sample 227-SB, 4ppm in n-propanol.

Figure V.24 shows the agglomerate diameters in boron doped Si powder 227SB measured as a function of time by photon correlation for three water contents. The rate of agglomeration increases with water content. In agreement with the sedimentation results, a 4 ppm Si sample in the stock n-propanol exhibited no agglomeration over the period examined; samples of this type did not sediment for periods in excess of 1 week. Pure Si powder, 645S, also did not exhibit agglomeration in the stock n-propanol. The enhancement of agglomeration rate with increased water content has been reported.<sup>37-39</sup>

The above phenomena can be explained by considering certain implications of the DLVO model. First it was shown in Section V.2 that the double-layer thickness for pure n-propanol is large, nominally 5  $\mu\text{m}$ . The average interparticle distance is 800Å for 500Å diameter Si particles at a 3 wt.% concentration. This interparticle spacing is well within the double-layer thickness and is near the maximum potentials indicated in Figures V.3 through V.6. These maximum potentials provide no effective barrier to agglomeration, so the agglomerates probably grow to large proportions, settle out of suspension, thus leaving a clear supernate.

For lower solids concentrations, a small potential barrier exists but is easily overcome by thermal agitation. Many agglomerates grow to a large size and settle out. Some however remain small and remain suspended for extended periods resulting in turbid supernates. Even with very dilute dispersions and large interparticle separations, the diffuse potential barrier is not great enough to restrict particle approach. The stability results from another factor.

The collision frequency between gas molecules (Z) is given by:

$$Z = 1/2 \sqrt{2} \pi r^2 \bar{c} n^2$$

where  $r$  = collision diameter;  $\bar{c}$  = mean velocity and  $n$  = molecular concentration. The same relation holds for dispersed particles moving under the influence of Brownian motion. The rate of agglomeration is proportional to the collision frequency between particles; or is proportional to  $n^2$ .

Dilute dispersions can be stable while concentrated dispersions are not simply because the collision frequency is low. If small agglomerates remain after substantial sedimentation has occurred, the dilute supernated dispersion may appear stable. However, in initially concentrated dispersions, the agglomerates grow rapidly to very large size. Because no substantial

fraction of small agglomerates will exist a clear supernate remains upon sedimentation.

#### V.5. CONCLUSIONS

The DLVO model examined in this paper predicts the unstable behavior of silicon in n-propanol at high concentrations. The double layer remains very diffuse due to the low concentration of counter-ions in the medium and the potential barrier necessary for stability is not established. The manipulation of surface charge or particle size within reasonable limits does not result in stability. For this reason steric means of stabilization is recommended.

The application of the Vold method of calculating van der Waals attractive potential for silicon particles with adsorbed water in n-propanol predicted reduced stability as compared with the non-water bearing system. These results are in accord with experimental findings using photon correlation and TEM.

Photon correlation (PC) was compared with TEM as a means of determining agglomerate size distribution. Good agreement was found establishing PC as a rapid method of determining this parameter. Application of this method was demonstrated in determining the effect of water on dispersion stability. Agglomerate size distribution was found to be log-normal by TEM.

FTIR spectra of boron and non-boron doped silicon powders were examined. Both samples contained lattice oxygen and SiH. Physically adsorbed water was found on the surface of boron doped powder, but not on the pure Si powder. FTIR was shown to be a rapid means of chemical characterization of silicon powders.

Microelectrophoresis was applied to dispersions of both doped and undoped powders with both moderate and low concentrations of water. Doping had little effect on mobility, whereas mobility increased sharply with increased water.

#### V.6. ACKNOWLEDGEMENTS

The support of ONR/ARO Contract # N00014-82-K-0350 is gratefully acknowledged. The authors would also like to thank E. Barringer, C. Cali, D. Casey, M. Dahlén, S. Danforth, J. Flint, T. Kramer, M. Kniffen and M. Strauss for their contributions.

## V.7. REFERENCES

1. E. A. Barringer, "The Synthesis, Interfacial Electrochemistry, Ordering, and Sintering of Monodispersed  $\text{TiO}_2$  Powders", MIT, Cambridge, MA (1983).
2. H. K. Bowen, October 1980, Physics and Chemistry of Packing Fine Ceramic Powders, under Contract DE-AC02-80ER10511, M.I.T., Cambridge, MA.
3. E. A. Barringer, and H. K. Bowen, "Formation, Packing, and Sintering of Monodispersed  $\text{TiO}_2$  Powders", MIT, Cambridge, MA (1982).
4. J. S. Haggerty, Sinterable Powders from Laser Driven Reactions, Under ONR/ARO Contract N00014-77-C0581, Final Report, M.I.T., Cambridge, MA, 1981.
5. S. Mizuta, W. R. Cannon, A. Bleier, and J. S. Haggerty, Wetting and Dispersion of Silicon Powder Without Deflocculants, Am. Ceram. Soc. Bull., 61, 872-875 (1982).
6. H. K. Bowen, D.O.E. 90413, 1981.
7. J. S. Haggerty and H. K. Bowen, Principal Investigators, "Processing of Laser Formed SiC Powders", NASA Contract No. NAG 3-312, 1982.
8. F. Thummler, "Sintering and High Temperature Properties of  $\text{Si}_3\text{N}_4$  and SiC" in Sintering Processes, Proceedings of the Fifth International Conference on Sintering and Related Phenomena, Materials Science Research, 13, 247-60 (1980).
9. H. R. Kruyt, ed. Colloid Science I: Irreversible Systems Hydrophobic Colloids. New York: Elsevier Pub. Co., 1952.
10. M. J. Sparnaay, Advan. Colloid Interface Sci., 1: 277 (1967).
11. G. D. Parfitt, "Fundamental Aspects of Dispersion" Dispersion of Powders in Liquids (G. D. Parfitt, ed.) Englewood: Applied Science Publishers, 1981.
12. F. M. Fowkes, F. W. Anderson, and R. J. Moore Abstracts, 150th ACS Meeting, September 1965.
13. F. M. Fowkes, Disc. Faraday Soc., 42: 246, 1966.
14. J. L. Van der Minne, and P. H. J. Hermanie. J. Colloid. Sci., 7: 600, 1952.
15. J. S. Haggerty, and W. R. Cannon, July 1980, Sinterable Powders from Laser Driven Reactions, under Contract N00014-77-C0581, M.I.T., Cambridge, MA.

16. A. G. Gaydon, and H. G. Wolfhard, Flames: Their Structure, Radiation, and Temperature, Chapman and Hall, Ltd., London, 1970.
17. H. C. Van de Hulst, Light Scattering by Small Particles, John Wiley and Sons, Inc., N.Y., 1957, Chap. 14.
18. Y. Suyama, R. Marra, J. S. Haggerty, and H. K. Bowen, "Synthesis of Ultrafine SiC Powders by Laser Driven Gas Phase Reaction", to be published.
19. T. M. Kramer, "Dispersion and Surface Studies of Laser Synthesized SiC", Ph.D. Research in progress, M.I.T.
20. A. C. G. Mitchell, And M. W. Zemansky, Resonance Radiation and Excited Atoms, Cambridge Univ. Press, Cambridge, 163, 1961.
21. J. W. C. Johns, and W. A. Krieiner, "Measurement and Analysis of the  $\nu_4$  Band of Silane", J. Mol. Spectrosc. 60, 400-11 (1976).
22. J. H. Purnell, and R. Walsh, "Pyrolysis at Monosilane", Proc. Royal Soc., Series A, London, p. 545, 1966.
23. C. H. Haas, and M. A. Ring, "Reaction of Silyl Radical and Silylene with Acetylene and Application to Orbital Symmetry to the Pyrolysis of Silane and Disilane", Inorganic Chemistry, 14, 2253, (1975).
24. F. S. Galasso, R. D. Veltri, and W. J. Croft, "Chemically Vapor Deposited  $\text{Si}_3\text{N}_4$ ", Bull. Am. Ceram. Soc., 57, 453 (1978).
25. M. J. Vold, J. Colloid. Sci., 16: 1, 1961.
26. R. J. Hunter, Zeta Potential in Colloid Science New York: Academic Press, 1981.
27. J. Barthel, R. Wachter, and H. J. Gores, Faraday Disc. of Chem. Soc., 64: 287, 1977.
28. V. S. Vavilov, E. N. Lotkora and A. F. Plotnikov, J. Phys. Chem. Solids, 22: 31, 1961.
29. R. K. Iler, The Chemistry of Silica, N.Y., J. Wiley & Sons, 1979.
30. S. Smakula, and J. Kalnaja, J. Phys. Chem. Solids., 6: 46, 1958.
31. D. L. Stierwalt, and R. F. Potter, J. Phys. Chem. Solids., 23: 99, 1962.
32. B. N. Brockhouse, J. Phys. Chem. Solids, 8: 400, 1959.
33. R. C. Weast, ed., Handbook of Chemistry and Physics, Cleveland: The Chemical Rubber Co., 1972.

34. M. Dahlen, Silicon Dispersion (Internal Report Material Science and Engineering Department, Massachusetts Institute of Technology, Dec. 1, 1982).
35. S. Danforth, The Dispersion Work of the Laser Synthesized Powder, (Internal Report: Materials Science and Engineering Department. MIT, April 4, 1982).



## CHAPTER VI

### SURFACE TENSIONS OF ALUMINA-CONTAINING LIQUIDS

by

J. M. Lihmann and J. S. Haggerty

#### ABSTRACT

The surface tensions of CO<sub>2</sub> laser-melted alumina-containing liquids have been measured by a static, pendant-drop technique in air, helium, and a 90% helium and 10% hydrogen mixture. The influences of up to 10 wt.% Cr<sub>2</sub>O<sub>3</sub>, MgO and TiO<sub>2</sub> have been studied. Surface tension data are also reported throughout the whole concentration range between liquid alumina and zirconia in air. An improved analytical technique based on comparing calculated and observed melt contours is reported.

#### VI.1. INTRODUCTION

Except for salts and glasses, relatively few data<sup>1-5</sup> exist for the physical and chemical properties of liquid ceramics. This paper reports static surface tensions of alumina-containing melts measured by the pendant drop technique. Future dynamic techniques will provide independent measurements of the surface tension-to-density ratios as well as the melt viscosities. The Al<sub>2</sub>O<sub>3</sub>-Cr<sub>2</sub>O<sub>3</sub>, Al<sub>2</sub>O<sub>3</sub>-MgO, Al<sub>2</sub>O<sub>3</sub>-TiO<sub>2</sub> and Al<sub>2</sub>O<sub>3</sub>-ZrO<sub>2</sub> systems were selected because at present they represent the commercially most important and technically most interesting alumina-based ceramics.

#### VI.2. ANALYTICAL

Broken and distorted bonds between atoms at the liquid-vapor interface cause an excess energy defined as the surface energy. For incompressible liquids, the surface energy is equal to the surface tension because surface stresses are relieved by viscous flow. The surface tension causes a pressure difference,  $\Delta P$ , across a curved interface,<sup>6-7</sup> defined by:

$$\Delta P = \gamma(1/R_1(z) + 1/R_2(z)) , \quad (1)$$

where  $\gamma$  is the surface energy or tension of the liquid-vapor interface, and  $R_1$  and  $R_2$  are the principle radii of curvature of the interface at an altitude  $z$ . The internal pressure within a fluid body having a density  $\rho$  varies with altitude as  $\rho g z$ ; the changing pressure causes the local shape to vary accordingly.

The drop shape is used to define the surface tension in the pendant-drop technique. Figure VI.1 shows the pendant-drop geometry and Equation 2 defines the analytical relationship between the liquid properties and pendant-drop shape:

$$2\gamma/b - \gamma(1/R_1(z) + 1/R_2(z)) = \rho g z \quad (2)$$

where  $b$  is the drop radius at  $z=0$ .

Pendant-drop shapes can be analyzed using the differential form of Equation 2:

$$\left(\frac{\rho g b^2}{\gamma}\right)\left(\frac{z}{b}\right) = 2 - b \left[ \left( \frac{d^2 z / dr^2}{(1 + (dz/dr)^2)^{3/2}} \right) + \left( \frac{dz/dr}{r(1 + (dz/dr)^2)^{1/2}} \right) \right] \quad (3)$$

Solutions to Equation 3 are families of curves parameterized by  $\beta$  (Figure VI.1) where:

$$\beta = -\rho g b^2 / \gamma \quad (4)$$

and  $r/b$  and  $z/b$  values are tabulated<sup>8-10</sup> as a function of  $\beta$ . Although Bashforth and Adams' tables<sup>8</sup> contain exact solutions to Equation 3, they have not been extensively used since they require the experimental determination of  $b$ .

Alternatively, the pendant drops can be analysed<sup>11-13</sup> using the relationship

$$\frac{\gamma}{\rho g} = \frac{b^2}{(-\beta)} = \frac{4r_e^2}{H} \quad (5)$$

where  $H$  is a numerical factor tabulated as a function of  $S = r_s/r_e$  (Figure VI.1). This procedure is simpler and potentially more accurate since it eliminates the necessity of measuring  $b$ . The method is still subject to considerable error since it depends on the  $r_s$  value measured at an altitude  $2r_e$ .

Stauffer<sup>14</sup> analyzed the errors expected using this analytical procedure. Assuming a 1% measurement error, he showed that the uncertainty in  $\gamma/\rho$  is 20% for  $S = 0.4$  while it decreases to 2.6% for  $S = 0.85$ . The extreme sensitivity of the technique to measurement errors is evident from the small differences

in the positions of curves A, B and C in Figure VI.1, at an altitude  $z = 2r_e$ .

The use of longer length-to-diameter ratios improves the precision because the pendant-drop contours separate from one another as shown in Figure VI.1. The accuracy also improves because the actual pendant-drop shape is less subject to distortions caused by non-circular cross-sections, non-planar solid-liquid interfaces and non-freely hinging solid-liquid interfaces. Many authors<sup>12-15</sup> have recommended using pendant-drop lengths that exceed  $3.0-4.0 r_e$ .

We found this procedure gave unacceptable accuracy with the oxides investigated. In fact, pendant-drop lengths in excess of  $2.2-2.6 r_e$  could not be achieved with the  $\gamma/\rho$  values characteristic of this work, because Rayleigh instability caused the pendant-drops to neck off when drop length-to- $r_s$  ratios exceeded a critical value ( $\approx 3.0$ ) apparently related to the zone-height instabilities<sup>16</sup> found for floating-zone crystal growth between unequal rod diameters. Longer drop lengths would require lower  $\gamma/\rho$  values. Also, we were not able to reliably measure  $r_s$  values with 1.0% precision because of the combined effects of  $r_e$  errors, absence of a sharp image boundary caused by optical flare and an uncertain position caused by vibrations that appeared intrinsic to the high-temperature melts.

Therefore, we elected to compare shapes computed from Equation 3 directly with observed shapes to minimize the errors resulting from short pendant-drops. By making a visual comparison over the entire lengths of the contours, it was possible to make a precise selection of the correct computed curve.

The procedures used to calculate the pendant-drop shapes followed those given in References 17-19. The entire contour is defined by the assumed  $r_e$  and  $\beta$  values;  $\beta$  is defined by  $r_e/b$ . For an assumed  $r_e$  value, a family of contours was generated as a function of  $b$ . Typical such contours, A-H, are shown in Figure VI.1 for a particular value of  $r_e$ . Iteration over a range of  $r_e$  values provided a complete set of curves, each of which correspond to a specific  $b^2/\beta$ . Equation 4 is used to calculate  $\gamma/\rho$  for the best fitting curve.

It is important that the observed and calculated contours be the same over their entire lengths. Figure VI.1 illustrates the expected shapes for constant  $r_e$  values with different  $\gamma/\rho$  values. Curves A-C, Figure VI.2,

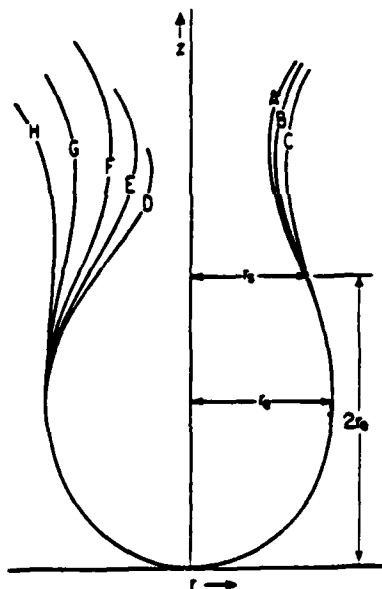


Figure VI.1. Shows some pendant-drop shapes computed for a constant  $r_e$  value. Curves D through H in this order correspond to  $\beta_e$  values (Equation 3) of -0.25, -0.31, -0.37, -0.475, and -0.55. Curves A, B and C, though defined by very close values of  $S = r_s/r_e$  (Equation 6) and almost undistinguishable at the altitude  $z = 2r_e$ , correspond to  $\gamma/\rho$  values as different as 214.73, 201.79 and 187.24, respectively.

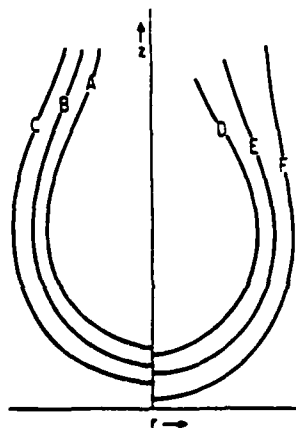


Figure VI.2. Illustrates the non-linear aspect of Equation 3. Parallel curves like A, B, and C correspond to very different  $\gamma/\rho$  values: 190.4 (A), 253.7 (b) and 352.5 (C), whereas non-parallel contours D, E and F define similar values of  $\gamma/\rho$ : 249.5 (D) 253.7 (E), 258.2 (F).

illustrate the error in  $\gamma/\rho$  resulting from selecting a contour that parallels the observed pendant-drop shape. Curves D-F, Figure 2, illustrate that the pendant-drop shapes are in fact quite a strong function of  $r_e$  for similar  $\gamma/\rho$  values. With a little practice, it is possible to distinguish between matching and incorrect contours.

Except for pure  $\text{Al}_2\text{O}_3$ <sup>20,21</sup> and  $\text{Cr}_2\text{O}_3$ <sup>5</sup>, the densities of the investigated liquids have not been reported. Rule of mixture approximations and assumptions given in Reference 3 were used to calculate liquid densities of  $\text{Al}_2\text{O}_3$ - $\text{Cr}_2\text{O}_3$ ,  $\text{Al}_2\text{O}_3$ - $\text{MgO}$ ,  $\text{Al}_2\text{O}_3$ - $\text{TiO}_2$  and  $\text{Al}_2\text{O}_3$ - $\text{ZrO}_2$  mixtures. Our calculations assumed the density of liquid  $\text{Al}_2\text{O}_3$  at the melting point to be  $3.01 \text{ g/cm}^3$ . The densities of other end-member molten oxides assumed a 20.4% volumetric expansion upon melting. Summarized in Figure VI.3 are the  $\rho$  results used in  $\gamma$  calculations.

### VI.3. EXPERIMENTAL

Experimentally, melts were created on the bottom ends of polycrystalline feed rods in a controlled atmosphere chamber. The incandescent melts were

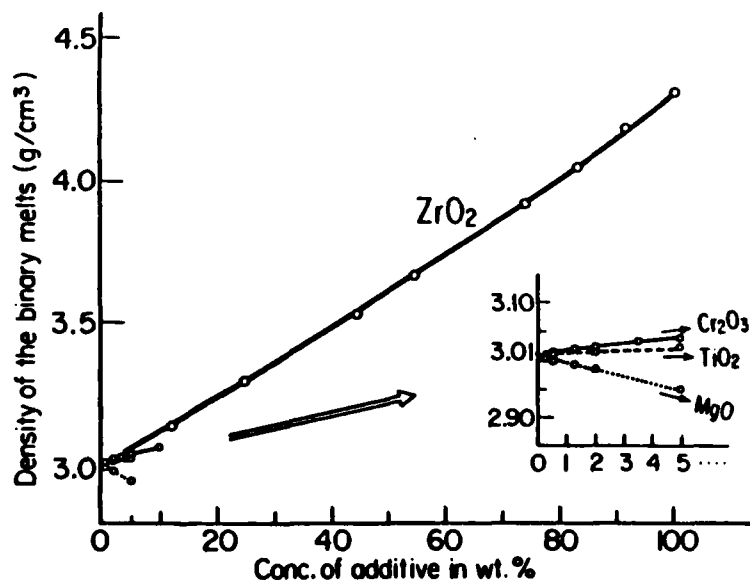


Figure VI.3. Density of the various melts as calculated with the approximations detailed in Section VI.2.

projected with a single lense (20x magnification) onto a surface where they were compared with calculated contours.

Heating was accomplished with four 10.6  $\mu\text{m}$  wavelength beams of light that orthogonally impinged onto the melts in a radial direction. The light source was a 1350 watt- $\text{CO}_2$  laser custom-designed to emit two beams. Each of the emitted beams was divided into two beams with roof-prisms. The beam dimensions on the melt surfaces were controlled by the relative positions of the focusing lenses and the melt. Typical spot diameters equaled the feed-rod diameters.

Laser heating is particularly applicable to high temperature materials. The laser has no characteristic temperature to set maximum temperature limits. Also ambient atmospheres can be selected without serious restrictions.

Feed rods were isostatically pressed from powders batched to the desired overall compositions with mixtures of pure oxide powders. Nominally 3 mm diameter rods were sintered for 12 hours at 1200°C, typically producing a 65% dense, 10  $\mu\text{m}$  grain size rod. Further densification occurred over a distance of nominally one rod diameter when they were melted. No material was withdrawn from the melt onto the feed rod, so the melt composition was equal to the batch composition. With the exception of the high  $\text{ZrO}_2$  compositions, vaporization losses were negligible.

The relative beam positions on the melt and beam powers were adjusted to make the solid-liquid interface as flat as possible. When properly adjusted, the altitude of the solid-liquid interface was uniform within  $\pm 0.05$  mm. Shaft rotation flattened the interface further but could not be used effectively in surface tension measurements because vibrations made the drop shape uncertain and severely limited the maximum drop length that could be achieved before it fell from the feed rod.

Some superheating<sup>22,23</sup> occurred where the laser beams intersected the melts. By expanding the beam diameters to equal the feed diameters, the radiant flux onto the melt surfaces was made as uniform as possible. This adjustment combined with the action of a spherical radiation shield positioned to refocus reflected and emitted radiation on the center of the melt minimized the superheat to  $\approx 20^\circ\text{C}$ . Free convection in the melt acted to reduce temperature gradients and insure compositional uniformity.

Melt contours were analysed with progressively increasing melt volumes until the melt dropped off to maximize the length-to-diameter ratio. The final  $S$  values were  $\approx 0.85$ . For this study, 300 theoretical contours were computed for 15 values of  $r_e$  ranging from 2.17 to 4.07 mm and 20 values of  $(-8)$  ranging from 0.25 to 0.55. The incremental  $\gamma/\rho$  between successive curves is approximately 1%. Generally each data point represents an average of 5 measurements.

#### VI.4. RESULTS AND DISCUSSION

The results demonstrate the superior precision of this technique for analyzing pendant-drops. The extreme between  $\gamma/\rho$  values for 5 independent measurements was typically 1% when determined by comparing contours. This reproducibility is comparable to the incremental differences between the calculated contours used to analyse the experimental contours. In contrast,  $\gamma/\rho$  values determined from measured  $r_e$  and  $r_s$  values varied as much as  $\pm 10\%$ .

The accuracy potential provided by this technique exceeds our knowledge of the melt densities. For pure alumina, reported liquid densities at the melting point range from  $2.51^{24}$  to  $3.05 \text{ g/cm}^3^{25}$ . We adopted the more recent and accepted value of  $3.01 \text{ g/cm}^3^{1,27}$ . Since the densities of other studied liquids have not been characterized experimentally, we calculated them using an average value of the thermal expansion coefficient of the solid between the ambient temperature and the melting point, and assuming a 20.4% volume expansion upon melting. It is evident that the  $\gamma$ -accuracy is limited by the  $\rho$  accuracy at this time. We would speculate that our  $\gamma$ -errors are in the range of 2-3% ( $13\text{--}20 \text{ ergs/cm}^2$ ). As can be seen from Table VI.1, this precision is much better than those obtained so far with other surface tension-measurement technique. The difference between our measured value for the surface tension of  $\text{Al}_2\text{O}_3$  in He and that cited in Reference 5 ( $570 \text{ ergs/cm}^2$ ) exceeds this estimate of error. This difference may reflect a systematic difference between the pendant drop and bubble pressure measurement techniques.

The results of  $\gamma$  determinations for  $\text{Al}_2\text{O}_3\text{--Cr}_2\text{O}_3$ ,  $\text{Al}_2\text{O}_3\text{--MgO}$ ,  $\text{Al}_2\text{O}_3\text{--TiO}_2$  and  $\text{Al}_2\text{O}_3\text{--ZrO}_2$  systems for each of the three atmospheres investigated are shown in Figures VI.4 through VI.7. The  $\gamma$ -axes are truncated to expand the

TABLE VI.1

## CITED SURFACE TENSION VALUES OF LIQUID ALUMINA

Surface Tension (ergs/cm <sup>2</sup> )	Atmosphere	Method Used	Reference
665±15 625±14 610±13	air He He+10%H <sub>2</sub>	pendant drop ( $\rho=3.01$ )	this study
700		theoretical value (based on the (electrostatic) forces between ions in a coordination or nearly ordered melt)	Sokolov <sup>26</sup>
577±80 586±81	vacuum vacuum	drop-weight method ( $\rho=2.5$ ) drop-weight method ( $\rho=3.2$ )	Von Wartenberg <sup>24</sup>
690±48	He	pendant drop ( $\rho=2.97$ )	Kingery <sup>3</sup>
551	not specified	sessible drop, from contact angle value	Bartlett <sup>25</sup>
574±68	vacuum	pendant drop ( $\rho=3.01$ )	Rasmussen <sup>27</sup>
570	He	maximum bubble pressure ( $\rho=3.03$ )	Anisimov <sup>5</sup>



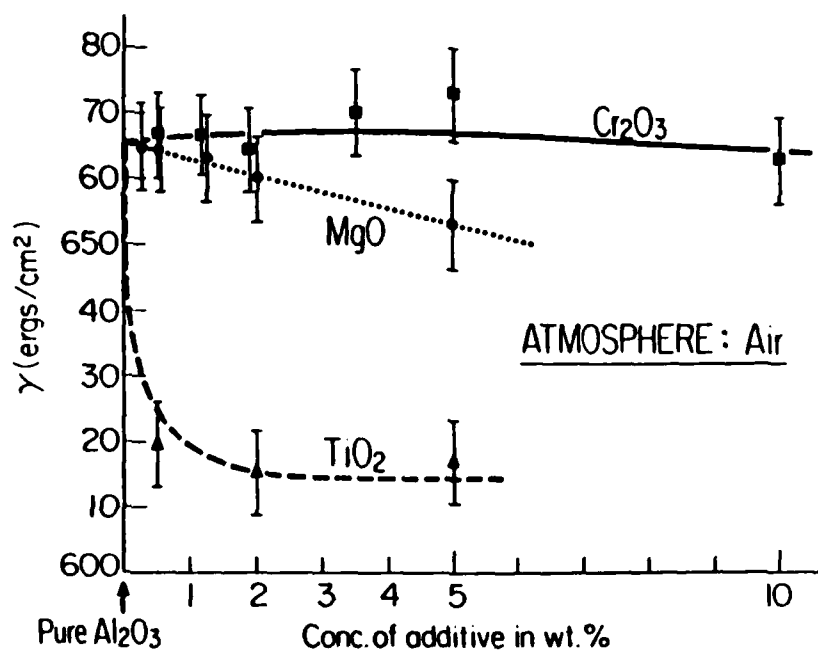


Figure VI.4. Experimental surface tension of the liquids in air.

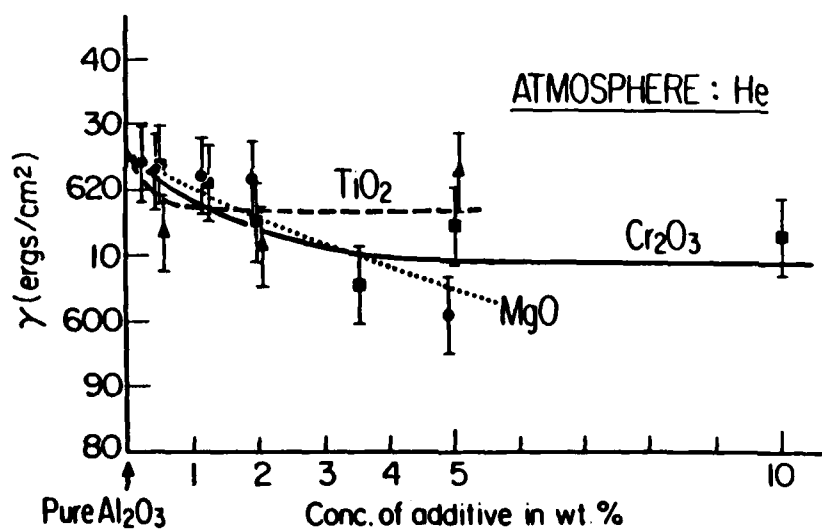


Figure VI.5. Experimental surface tension of the liquids in helium.

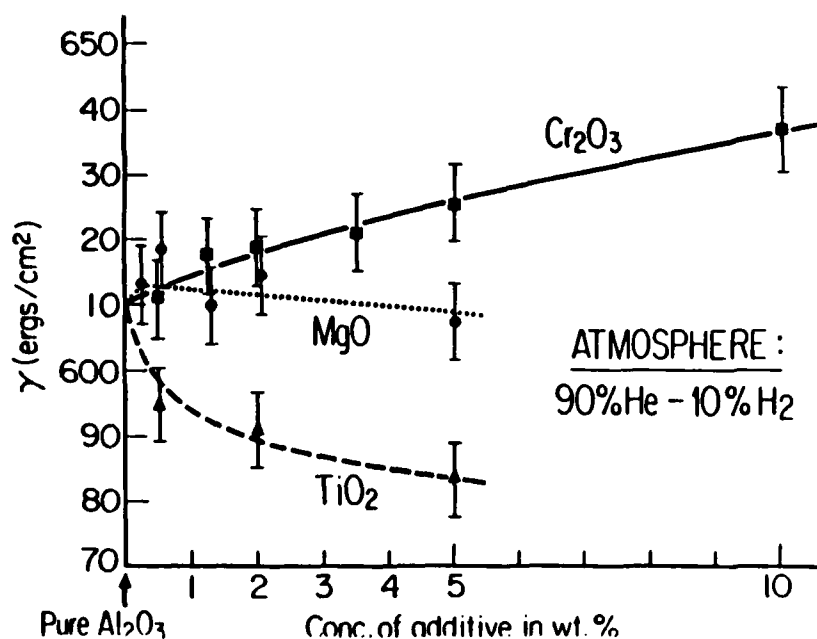


Figure VI.6. Experimental surface tension of the liquids in a 90% helium - 10% hydrogen mixture.

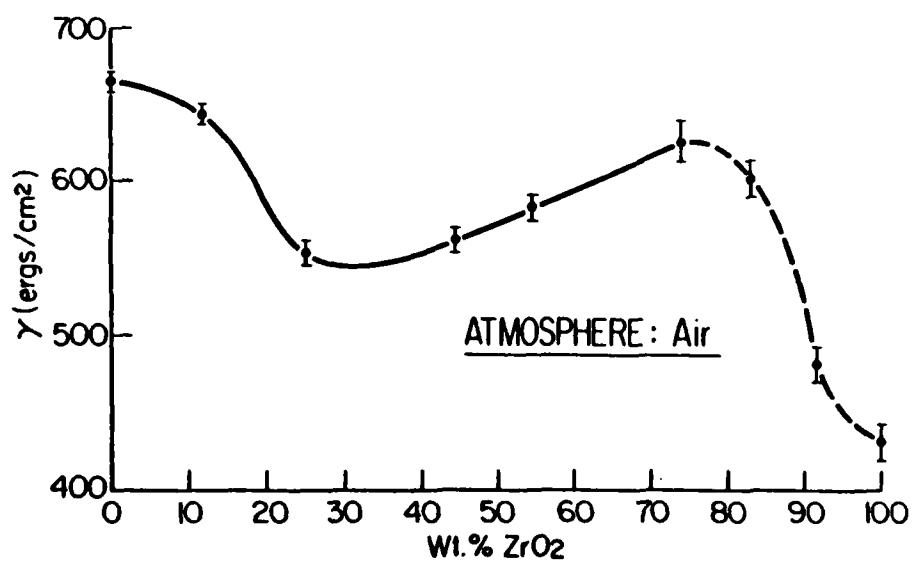


Figure VI.7. Experimental surface tension of various Al<sub>2</sub>O<sub>3</sub>-ZrO<sub>2</sub> liquids in air.

scales. The  $\text{Al}_2\text{O}_3$ - $\text{ZrO}_2$  data were plotted separately from the other data taken in an air-atmosphere because ranges of variables were wider.

In general, surface energies increased with increasing oxygen partial pressure. For pure  $\text{Al}_2\text{O}_3$ ,  $\gamma$  was 665, 625 and 610 ergs/cm<sup>2</sup> for air, He and He- $\text{H}_2$  atmospheres respectively.

The effect on surface energies of additions up to ~ 10 weight percent was generally either a small monotonic increase or decrease.  $\text{TiO}_2$ , the exception, caused a rapid decrease in  $\gamma$  for levels < 0.5 wt.%, followed by essentially constant  $\gamma$  values for higher concentrations. All samples characterized by electron microprobe showed identical surface and bulk compositions.

For an air atmosphere, additives generally caused the  $\gamma$  values to increase or decrease in the same direction that they cause the liquidus curves to change. For small concentrations,  $\text{Cr}_2\text{O}_3$  is the only additive that raises the melting point and is the only additive that raises the  $\gamma$  value. The minimum  $\gamma$  value for the  $\text{Al}_2\text{O}_3$ - $\text{ZrO}_2$  system corresponds to the eutectic composition, approximately 42 wt.%. For  $\text{ZrO}_2$  contents > 70 wt.%,  $\gamma$  decreases with increasing  $\text{ZrO}_2$ , violating this generality. This departure may result from a thermal reduction of the high  $\text{ZrO}_2$ -content melts as evidenced by the darkening of the quenched pendant-drops, following the trend of reduced  $\gamma$ 's with reduced oxygen partial pressures.

The effects of additives on  $\gamma$ 's in He and He- $\text{H}_2$  atmospheres are more complex; their magnitudes do not follow trends expected on the basis of oxygen partial pressure. No data was found for the effect of oxygen partial pressure on melting points, so this correlation could not be examined. It is apparent that  $\gamma$ 's for these systems are sensitive to atmosphere and composition even though the causes are not understood.

## VI.5. SUMMARY AND CONCLUSIONS

An improved technique for analyzing the surface energies of liquids in a pendant-drop configuration has been developed. The procedure, based on comparing observed and calculated contours, is particularly applicable to melts that cannot be extended to high length-to-diameter ratios and to high temperature melts for which precise dimensional characterization is difficult. The results demonstrated the technique with several alumina

containing melts. The precision of the  $\gamma/\rho$  measurements appears to be approximately 1%. The accuracy of the  $\gamma$  values is limited by the lack of  $\rho$  values.

Both composition and atmosphere have strong effects on  $\gamma$  values. In an air atmosphere, the effect of additives on  $\gamma$ 's parallels their effect on melting points. In He and He-H<sub>2</sub> atmospheres the effects are more complex.

#### VI.6. ACKNOWLEDGEMENTS

This research was supported by ONR and ARO under contract N0014-82-K-0350, and the French Government by a salary grant. The specialized laser heated crystal growth equipment was provided by NSF Contract No. 791687-DMR and Anne H. Foster, Boston, MA, and the Materials Processing Center, MIT. David Lum, Douglas Chin and Paul McGrath assisted in sample preparation and computational work; Professor R. A. Brown provided important background information and insights. All these contributions are gratefully acknowledged.

## VI.7. REFERENCES

1. Turkdogan, E. T., Physico-Chemical Properties of Molten Slags and Glasses, The Metals Society, London, August 1983.
2. M. Humenik and W. D. Kingery, "Metal-Ceramic Interactions: Surface Tension and Wettability of Metal-Ceramic Systems," J. Am. Ceram. Soc., 37 [1], 18-23 (1954).
3. W. D. Kingery, "Surface Tension of Some Liquid Oxides and Their Temperature Coefficients," J. Am. Ceram. Soc., 42 [1], 6-8 (1959).
- 4a. V. P. Elyutin, E. F. Grifts and B. S. Mitin, "Wetting of Refractory Metals by Oxide Melts," Izv. Akad. Nauk. SSSR, Neorg. Mater., 10, 5 (1974), (Engl. Transl.) Inorganic Materials, 10, 723-25 (1974);  
b. *ibid.*, 10, 1796-97 (1974).
5. Yu. S. Anisimov, E. F. Grifts and B. S. Mitin, "Surface Tension and Density of Melts of the Systems  $Al_2O_3-SiO_2$  and  $Al_2O_3-Cr_2O_3$ ," Izv. Akad. Nauk. SSSR, Neorg. Mater., 13, 1444-46 (1977); (Engl. transl.) Inorganic Materials, 13, 1168-70 (1977).
6. T. Young, "An Essay on the Cohesion of Fluids," Proc. Roy. Soc., London, 1, 171 (1804); Phil. Trans. Roy. Soc. London, 1805, p.61.
7. P. S. Laplace, Mecanique Celeste, Suppl.<sup>t</sup>. Livre X, Paris, 1805.
8. F. Bashforth and J.C. Adams, An Attempt to Test the Theories of Capillary Action by Comparing the Theoretical and Measured forms of Drops of Fluids, Cambridge Univ. Press, London, 1883.
9. S. Sugden, "The Determination of Surface Tension from the Rise in Capillary Tube," J. Chem. Soc., 1483 (1921).
10. N. K. Adam, The Physics and Chemistry of Surfaces, 3rd Ed., Oxford Univ. Press (1941), p. 365.
11. J. M. Andreas, E. A. Hauser and W. B. Tucker, "Boundary Tension by Pendant Drops", J. Phys. Chem., 42, 1001 (1938).
12. S. Fordham, "On the Calculation of Surface Tension from Measurements of Pendant Drops," Proc. Roy. Soc. London, A194, 1 (1948).
13. A. W. Adamson, Physical Chemistry of Surfaces, 2nd Ed., John Wiley & Sons, (1967), p. 14.
14. C. E. Stauffer, "The Measurement of Surface Tension by the Pendant Drop Technique," J. Phys. Chem., 69, 1933 (1965).
15. C. Huh and R. L. Reed, "A Method for Estimating Interfacial Tensions and Contact Angles from Sessile and Pendant Drop Shapes", J. Colloid Interface Sci., 91 [2], 472 (1983).

16. J. S. Haggerty and W. P. Menashi, Production of Oxide Fibers by a Floating Zone Fiber Drawing Technique, NASA CR-72811, ADL 71997.
17. J.F. Padday, "The Measurement of Surface Tension," in E. Matijevic, Surface and Colloid Science, vol.1, Wiley Interscience (1969), p.110-112.
18. J. F. Padday, "The Profile of Axially Symmetric Menisci, "Phil. Trans. Roy. Soc., London, A269, 265 (1971).
19. J. F. Padday and A. Pitt, "Axisymmetric Meniscus Profiles, "J. Colloid Interface Sci., 38, [2], 1972.
20. A. D. Kirshenbaum and J. A. Cahill, "The Density of Liquid Aluminum Oxide," J. Inorg. Nucl. Chem., 14, [3-4], 283-87 (1960).
21. B. S. Mitin and Yu. A. Nagibin, "Density of Molten Aluminum Oxide," (Engl. Transl.) Russian J. Phys. Chem., 44, [5], 741-42 (1970).
22. N. Bloembergen, "Fundamental of Laser-Solid Interactions," Laser-Solid Interactions and Laser Processing, 1978, Materials Research Society, p. 1-8.
23. M. Lax, "Temperature Rise Induced by a Laser Beam," J. Appl. Phys., 48, 3919 (1977); Appl. Phys. Letters, 33, 786 (1978).
- 24a. H. von Wartenberg, E. Wehner and E. Saran, "die Oberflächenspannung von geschmolzener  $Al_2O_3$  und  $La_2O_3$ ," Nachrichten Gesell. Wissensch. Göttingen, Math. Phys. Kl., Fachgruppe II, 65-71, (1936-37).  
 b. ibid, "Die Dichte geschmolzener Tonerde", 73-75, (1936-37).
25. R. W. Bartlett and J. K. Hall, "Wetting of Several Solids by  $Al_2O_3$  and BeO Liquids," Am. Ceram. Soc. Bull., 44, [5], 444-48 (1965).
26. O. K. Sokolov, "On the surface Tension of Molten Salts and Oxides," Izv. Akad. Nauk. SSSR, Metal Delo, 4, 59-64 (1963); (Engl. transl.) Russian Met. and Mining, 4, 37-44 (1963).
27. J. J. Rasmussen and R. P. Nelson, "Surface Tension and Density of Molten  $Al_2O_3$ ," J. Am. Ceram. Soc., 54, [8], 398-401 (1971).

**DATE**  
**ILME**